

EXPERIMENTAL STUDY OF A QUASI-OPTIC
SYNTHETIC PHASED-ARRAY TERAHERTZ
IMAGING SYSTEM

By

JOHN F. O'HARA

Bachelor of Science in Engineering

University of Michigan

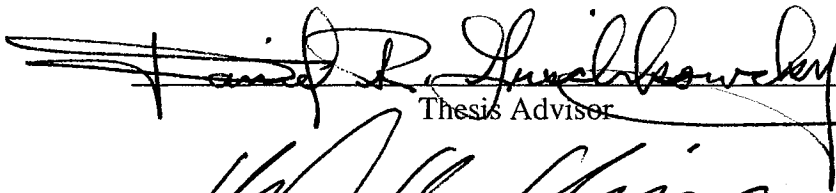
Ann Arbor, MI USA

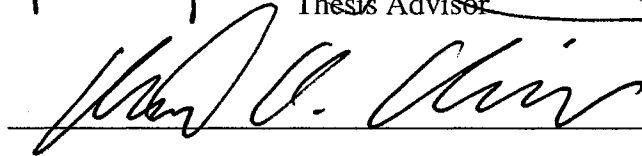
1998


Submitted to the Faculty
of the Graduate College of
Oklahoma State University
in partial fulfillment of
the requirements for
the Degree of
DOCTOR OF PHILOSOPHY
December, 2003


EXPERIMENTAL STUDY OF A QUASI-OPTIC
SYNTHETIC PHASED-ARRAY TERAHERTZ
IMAGING SYSTEM

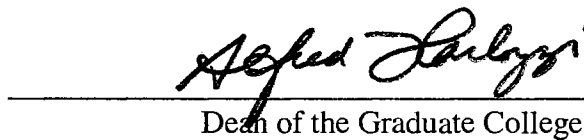
Thesis approved:


Thesis Advisor








Dean of the Graduate College

Acknowledgements

Before all, I would like to thank my major advisor, Dr. Daniel Grischkowsky, for warmly welcoming me into the terahertz group at Oklahoma State University, for guiding me in the spirit of scientific truth and excellence, and for granting me a comfortable measure of freedom without complaint. Over the past few years I have come to realize how great a privilege it was to be part of his research group and to work with him. I am forever grateful for that opportunity.

I would also like to thank Dr. Alan Cheville for somehow making every subject in science seem like the neatest thing in the world and for always being willing to pause for a discussion, regardless of the subject. I would like to thank Dr. James West for his stimulating lectures and discussions about electromagnetics, and for making me feel comfortable with his (often insulting) sarcastic witticisms. Many thanks are also due to Dr. Albert Rosenberger, an excellent teacher who was able to change my whole outlook on modern physics, making very difficult concepts both interesting and understandable.

Of course, I must also thank Dr. Rajind Mendis, a sublime friend who continues to keep me honest and look out for me. This work could never have been completed so fast without his helpful insight and discussions. Thanks pal. I am also lucky to have many other friends and family members to whom I now give thanks for the support they gave me in all aspects of my life and education.

To my parents, Emmett and Sharon, and my sister Susie, I cannot give enough

thanks. Throughout my entire life, they have never ceased to convey utter confidence in my abilities and unwavering faith that something good would come out of my life. Though I will continue to try to live up to their grand expectations, I hope this work serves as some small token of repayment for their generous investment in my life.

To my beautiful wife, Cindy, I give extra special thanks. Her constant love and attention during my time in Oklahoma made it possible for me to live happily and healthfully. Being a graduate student is easy with a woman like her. I am one lucky man, to be sure.

Finally, I would like to thank God for granting me a life that is so blessed: one in which I was given such an excellent education opportunity. I will certainly give it my all to find a way to give back some of the abundance I have received.

Table of Contents

Chapter	Page
1 INTRODUCTION.....	1
1.1 THz Properties and Imaging Applications.....	2
1.2 Purpose of This Study.....	4
1.3 Scope of the Dissertation.....	11
2 IMAGING SYSTEMS AND RESOLUTION.....	14
2.1 General Imaging Systems.....	14
2.2 Image Representation.....	17
2.3 Resolution Criteria.....	18
2.4 Spatial Frequencies.....	20
3 EXPERIMENTAL SETUP.....	24
3.1 General Layout.....	24
3.2 THz Image Production.....	27
3.3 Link to Ultrasonic Imaging.....	34
4 POINT SOURCE IMAGING.....	36
4.1 Single Point Source.....	36
4.1.1 <i>Diffraction Test by Mirror Size Reduction</i>	41
4.1.2 <i>Point Source Verification</i>	47
4.2 Two Point Sources.....	52
5 SYNTHETIC PHASED-ARRAY IMAGING.....	57
5.1 History of Aperture Synthesis.....	57
5.2 Aperture Synthesis in THz Imaging.....	59
5.3 Aperture Synthesis Realization.....	60
5.4 Phased-Array Imaging.....	64
5.5 Synthetic Array Details.....	65
5.5.1 <i>Vertical Arraying</i>	66

5.5.2	<i>Horizontal Arraying</i>	71
5.5.3	<i>Image Coherence</i>	74
5.5.4	<i>Phase Reference</i>	74
5.5.5	<i>Object Placement Accuracy</i>	76
5.5.6	<i>Image Reconstruction</i>	78
5.6	Single Point Source.....	79
5.6.1	<i>Three-Dimensional Data Display</i>	80
5.6.2	<i>Phased-Array Images</i>	82
5.6.3	<i>Artificial Aperture Doubling</i>	87
5.7	Two Point Sources.....	91
5.7.1	<i>Image Analysis and Enhancement</i>	92
5.7.2	<i>Ambiguous Phase Reference</i>	97
5.7.3	<i>Image Reconstruction</i>	99
5.7.4	<i>Array Steering</i>	105
5.8	Two-Dimensional Phased-Array Imaging.....	109
5.8.1	<i>Object Stealth</i>	114
6	THEORETICAL ANALYSIS	117
6.1	Formulation of Models.....	117
6.1.1	<i>Input Pulse</i>	118
6.1.2	<i>Initial Approximations</i>	119
6.1.3	<i>Phasor Notation</i>	120
6.1.4	<i>Comparison to Optical & Radio Systems</i>	122
6.1.5	<i>Diffraction Theory Foundation</i>	125
6.2	Debye Model.....	125
6.2.1	<i>Monochromatic Image</i>	128
6.2.2	<i>Broadband Image</i>	131
6.2.3	<i>Comparison</i>	138
6.2.4	<i>Debye Approximations</i>	141
6.3	Goodman Model.....	142
6.3.1	<i>Monochromatic Image</i>	145
6.3.2	<i>Broadband Image</i>	147
6.3.3	<i>Comparison</i>	152
6.3.4	<i>Approximations</i>	152
6.4	Hybrid Rayleigh-Sommerfeld Model.....	153
6.4.1	<i>Calculation Duration & Precision</i>	154
6.4.2	<i>Hybrid Model Setup</i>	156
6.4.3	<i>Monochromatic Image</i>	158
6.4.4	<i>Broadband Image</i>	162

6.4.5 Comparison.....	165
6.4.6 Illumination Angle	169
6.4.7 Diffraction Test by Mirror Size Reduction	173
6.4.8 Two Point Sources	175
6.5 Arrayed Images.....	180
6.5.1 Single 1 mm Ball.....	181
6.5.2 Two 400 μm Balls	185
7 CONCLUSIONS.....	188
REFERENCES	191

List of Figures

Figure		Page
1-1	Point illumination, transmission-mode, THz imaging system.....	6
1-2	Synthetic aperture THz impulse imaging system	7
1-3	Electro-optic THz imaging system	9
1-4	Quasi-optic THz imaging system.....	10
2-1	Basic imaging system	15
2-2	Off-axis imaging system.....	16
2-3	Rayleigh and Sparrow resolution criteria	19
2-4	Spatial frequency determination	22
2-5	Imaging systems of different spatial frequency bandwidths.....	23
3-1	THz imaging system, general layout	24
3-2	THz imaging system, plan view.....	26
3-3	THz transmitter details.....	28
3-4	THz receiver details	30
3-5	Scale diagram of imaging through receiver silicon lens	31
3-6	Object mounting apparatus	33
4-1	Point source justification for 1 mm ball.....	37
4-2	Single spatial sample of 1 mm ball image	38
4-3	One-dimensional THz image of 1 mm ball.....	39

4-4	THz image of 1 mm ball, side and plan views.....	40
4-5	Scale diagram of geometric cone of THz impingent on receiver	42
4-6	Single spatial sample of 1 mm ball image with halved diameter mirror	43
4-7	One-dimensional THz image of 1 mm ball with halved diameter mirror.....	44
4-8	THz image of 1 mm ball with halved diameter mirror, side and plan views.....	45
4-9	Single spatial sample of 391 μm ball image	48
4-10	One-dimensional THz image of 391 μm ball.....	49
4-11	THz image of 391 μm ball, side and plan views.....	50
4-12	Two point source object comprised of two 1 mm balls	52
4-13	Single spatial sample of two ball image	53
4-14	One-dimensional THz image of two ball object.....	54
4-15	THz image of two ball object, side and plan views	55
5-1	Phased-array THz imaging system	61
5-2	Scale view of THz beam in phased-array system	62
5-3	Side view of phased-array THz imaging system	63
5-4	Relationship of mirrors, scan plane, and image plane in real array	67
5-5	Relationships of image plane and phase fronts from real mirrors	68
5-6	Relationship of mirrors, scan plane, and image plane in synthetic array	69
5-7	Comparison of image planes and phase fronts for synthetic and real case.....	70
5-8	Horizontal arraying details.....	73
5-9	Phase locked reference waveforms for two arrayed THz images.....	76
5-10	Transverse array images of point source (energy and amplitude).....	84
5-11	Slice through composite array image of point source.....	85

5-12	Side view of phased-array system showing geometric image planes	85
5-13	Artificial aperture doubling model.....	87
5-14	Side view of aperture doubled system showing composite image plane.....	90
5-15	Two point source object comprised of two 391 μm balls.....	91
5-16	Slice through composite array image of two 391 μm balls	94
5-17	Reflection features from two 391 μm balls.....	94
5-18	Transverse, arrayed energy image of two 391 μm balls	95
5-19	Transverse, arrayed isoamplitude plot of two 391 μm balls.....	96
5-20	Phase reference waveforms for three images of two 391 μm balls	98
5-21	Phase reference waveforms for seven different scan plane orientations	101
5-22	Overlap between 0° reference and model waveform with components	103
5-23	Overlap between 0° and $\pm 10^\circ$ reference waveforms and model waveforms	104
5-24	Slice through composite array image, steered to upper reference ball	107
5-25	Slice through composite array image, steered to arbitrary reference.....	108
5-26	Scale diagram of T-ball object.....	110
5-27	Normalized partial energy images of T-ball object	112
5-28	Overlap of normalized partial-energy images of T and ball objects.....	113
5-29	Energy image of T-ball without separate normalization.....	114
5-30	Object stealth behavior for horizontal and vertical cylinders	115
6-1	Ideal input pulse for theoretical calculations	119
6-2	Debye theoretical model setup.....	127
6-3	One-to-one imaging system producing converging spherical waves	128
6-4	Normalized 0.7 THz field magnitude image of point source, Debye	130

6-5	Normalized 0.7 THz field amplitude slice through image of point source.....	130
6-6	Broadband field amplitude image of point source, Debye	134
6-7	Broadband image of point source, side and plan views, Debye	135
6-8	Shifted broadband amplitude image of point source, Debye	136
6-9	Shifted broadband image of point source, side and plan views	137
6-10	Comparison between Debye image and actual data image.....	139
6-11	Goodman theoretical model setup	142
6-12	Normalized 0.7 THz field magnitude image of point source, Goodman.....	146
6-13	Broadband field amplitude image of point source, Goodman	150
6-14	Broadband image of point source, side and plan views, Goodman	151
6-15	Hybrid theoretical model setup.....	156
6-16	Setup for diffraction portion of hybrid model.....	158
6-17	Normalized 0.7 THz field magnitude image of point source, Hybrid	159
6-18	Normalized 0.7 THz transverse magnitude image, Hybrid	161
6-19	Normalized 0.7 THz transverse image at circle of least confusion	162
6-20	Normalized broadband field amplitude image of point source, Hybrid	163
6-21	Broadband image of point source, plan view, Hybrid	164
6-22	Monochromatic image comparison from all models	165
6-23	Broadband image comparison from all models	167
6-24	Broadband image of point source, angled illumination, Hybrid.....	171
6-25	Broadband point source comparison image from section 4.1 data	171
6-26	Broadband image of point, angled illumination, plan view, Hybrid	172
6-27	Broadband point source comparison image from section 4.1 data, plan view ...	172

6-28	Comparison $\frac{1}{2}$ diameter aperture images, experimental and Hybrid.....	173
6-29	Two point source image by superposition, Hybrid.....	177
6-30	Two point source image by convolution with PSF, Hybrid.....	178
6-31	Comparison between two point source theory and data	179
6-32	Slice through composite array image of two point sources, Hybrid.....	182
6-33	Slice through array image of two point sources, experimental comparison	182
6-34	Transverse array images of point source (energy and amplitude), Hybrid.....	183
6-35	Transverse array images of point source, experimental comparison	184
6-36	Arrayed image of two point sources, Hybrid.....	186
6-37	Arrayed image of two point sources, experimental comparison.....	186
6-38	Comparison, data/theory, transverse arrayed energy image, Hybrid.....	187
6-39	Comparison, data/theory, transverse arrayed isoamplitude image, Hybrid	187

List of Symbols

a	aperture (mirror) radius, (m)
A	field amplitude coefficient
AS	aperture synthesis
b	binomial expansion variable
c	speed of light in free-space, 3×10^8 m/s
CCD	charge-coupled device
COLC	circle of least confusion
CT	computerized tomography
dS_w	differential wavefront surface area, (m^2)
$d\xi$	differential length in x -direction in diffraction plane, (m)
$d\eta$	differential length in y -direction in diffraction plane, (m)
$d\Omega$	differential solid angle, (steradians)
e	Euler's number, 2.718281828459045
E	field amplitude THz image, (V/m)
EM	electromagnetic
f	frequency, (Hz)
f_d	radius of curvature of spherical wave converging through aperture, (m)
f_L	focal length of spherical mirror, (m)

FWHM	full width at half maximum
G	energy density THz image, (J/m^2)
GaAs	gallium arsenide
h	amplitude point spread function, or impulse response, (V/m)
I	intensity image, (W/m^2)
IR	infrared
j	unit imaginary number, $\sqrt{-1}$
k	amplitude of wavevector (wavenumber), ($1/m$)
k_x	x -component of wavevector or angular spatial frequency in x , ($1/m$)
k_y	y -component of wavevector or angular spatial frequency in y , ($1/m$)
k_z	z -component of wavevector or angular spatial frequency in z , ($1/m$)
MRI	magnetic resonance imaging
N	Fresnel number
O	origin for theoretical image calculations
P	observation point for theoretical image calculations
P_y	intersection point between y -axis and wavefront
PET	positron emission tomography
PSF	point spread function
\mathbf{q}	unit vector from origin to point on wavefront
Q	point on converging wavefront
r_{01}	distance from differential radiator to observation point, (m)
\mathbf{R}	vector from origin to observation point
s	distance from point on converging wavefront to observation point, (m)

S	input THz pulse, (V/m)
SAR	synthetic aperture radar
SNR	signal to noise ratio
SOS	silicon-on-sapphire
t	time (s)
THz	terahertz
(u,v)	transverse (x,y) coordinates in image plane
U_i	scalar field (image) in image plane, (V/m or A/m)
U_o	object plane or field within that plane
U_l	input lens plane or field within that plane
U_l'	output lens plane or field within that plane
W	wavefront converging through aperture
(x,y,z)	coordinates in object space
z_1	distance from object plane to input lens plane
z_2	distance from output lens plane (or diffraction aperture) to image plane
α	system off-axis angle, (degrees)
Γ	system image plane
Γ_C	composite geometric image plane
Γ_O	spherical mirror geometric image plane
Γ_S	synthetic mirror geometric image plane
δ	point source
$\delta t_A, \delta t_C$	time delays for wavefronts in phased-array imaging, (s)
Δ	spatially dependent thickness function of lens, (m)

Δ_0	normal thickness of lens, (m)
$\Delta\varphi$	angular spread defining spatial frequency bandwidth, (degrees)
η_0	impedance of free space, (ohms)
θ	scan plane angle, (degrees)
λ	wavelength, (m)
λ_x	spatial frequency wavelength in x -direction, (m)
λ_y	spatial frequency wavelength in y -direction, (m)
λ_z	spatial frequency wavelength in z -direction, (m)
(ξ, η)	transverse (x, y) coordinates inside diffraction plane
ρ	maximum transverse extent of ray bundle, (m)
Σ	diffraction aperture
τ	pulse width, (s)
φ	angle between ray and optical axis, (degrees)
Φ	spatially dependent temporal delay function, (s)
ω	angular frequency, (radians/s)
Ω	solid angle extent of aperture, (steradians)

Chapter 1

Introduction

Imaging technology has a rich history that began thousands of years ago. The reflection from a pool of still water or a shiny metal surface was arguably the first imaging method routinely used by mankind. With the advent of lenses, many other novel forms of optical imaging emerged, including telescopes and microscopes. Using a lens, a pinhole camera, and a sensitized pewter plate, Niépce was the first person to permanently record an image. Optical photography and other forms of optical imaging have since become commonplace.

Of course, imaging has not been constrained to optical frequencies. In 1895 Roentgen discovered X-rays and successfully used them to form an image of his wife's hand. As with X-rays, whenever a portion of the electromagnetic (EM) spectrum became practically usable, it wasn't long before it was adapted to an imaging configuration. Therefore, it is not surprising that many types of imaging systems exist today and utilize the radio, microwave, infrared (IR), visible, ultraviolet, X-ray, and gamma ray portions of the EM spectrum. Pressure waves have also been adapted to imaging and are manifest in the various forms of ultrasonic and sonographic imaging systems.

The terahertz (THz) frequencies, lying right between the microwave and IR bands, are one of the more interesting portions of the EM spectrum, often behaving with

both microwave and optical characteristics simultaneously. Over the last couple decades, new means of producing and detecting terahertz (THz) radiation have come into frequent use. These methods produce sub-picosecond, broadband pulses of terahertz (THz) radiation by the use of ultrashort laser pulses and either fast photoconductive switches [1,2] or optical rectification and electro-optic effects [3,4]. The consequent liberation of the THz spectral band has since sparked many new forms of research including various forms of THz imaging [5-10].

1.1 THz Properties and Imaging Applications

As with any portion of the EM spectrum, THz has unique properties that make it highly suitable for certain imaging applications. First, THz generated in the aforementioned fashion is broadband with usable frequencies typically ranging from 0.05 THz to 3 THz. Since it is in the form of a pulse, it can be used as a powerful tool to simultaneously probe chemical or material properties over a broad spectral range. It has been found that THz penetrates most dry, non-polar, non-metallic objects such as paper, cardboard, glass, plastics, and non-polar organic substances [11]. For dielectrics, such as semiconductors, THz transparency depends on several factors including impurity concentrations [12]. Polar liquids and gases, such as water and water vapor, have very strong absorption lines in the THz region [13-15].

Additionally, the sub-picosecond pulses of THz radiation are detected coherently, allowing direct measurement of both amplitude and phase. This provides all the information needed to determine the complex dielectric function of a material. The THz

pulses are also transform-limited [16], and can be used as ranging pulses by which the structure of an object can be characterized in the time-domain via radar or echo-location principles. Also, the THz radiation is fairly linearly polarized; therefore polarization sensitive measurements are possible.

Finally, due to its relatively short wavelength, THz radiation is naturally suited to high resolution imaging. By properly designing an imaging system at THz frequencies it should be possible to achieve imaging with resolution on the order of a few hundred microns. This represents a significant resolution advantage over similar microwave systems. Like microwave systems, however, a THz system would retain the same powerful property of coherence.

Combining all these features with an imaging system makes possible many interesting applications. One such application is the spatially-dependent composition analysis of materials. With this analysis, spectroscopy could be used to determine whether an object was isotropic, homogeneous, or in possession of some other similar property. In a similar fashion, spectroscopy can be used to examine the content of certain chemicals with great sensitivity. For example, applications such as burn diagnostics [11], or biological tissue characterization [17], can utilize the high THz sensitivity to water. In these cases, minute differences in hydration levels could be used to distinguish various different types of tissue. Heavily burned tissue, for example, would have less moisture content than lightly burned tissue. It might also be possible to use hydration level, polarization rotation, or other measurable THz effects to distinguish cancerous and healthy tissue in a non-invasive fashion. Such measurements have already been used to identify dental caries [17] and could form the basis for early detection methods of skin

cancer and other skin diseases. With stronger THz sources, this idea could be extended to identify disease in deeper tissues.

Water content can also provide a quality control metric for moisture sensitive products, such as food items. One particular benefit of THz in this respect is the ability to penetrate most packaging materials, thereby allowing evaluation of a sealed product without exposing its contents to contamination. This property is particularly important for sterile or perishable items such as medical or food products. Other quality control processes can use the coherent, pulsed nature of the THz to tomographically identify manufacturing flaws, such as cracks or voids, inside of plastics, ceramics [18] and other products, which are semi-transparent to THz.

More potential imaging applications utilizing the coherence and spectral range of THz include pollution control and security. Being coherent, a THz system is highly insensitive to thermal noise sources and is able to measure the spectral response of very hot gases. As such, a THz imaging system could be used to monitor pollutant levels in exhaust gases or combustion processes [19]. Using spectral analysis, a THz imaging system could also address security issues by identifying weapons, such as letter bombs or explosives, biohazards or drugs [20], without opening up packaging material.

1.2 Purpose of This Study

This dissertation presents an effort to demonstrate, characterize, and theoretically explain the operation of a new type of THz imaging called *quasi-optic THz imaging*. In order to better understand the quasi-optic THz imaging system it is beneficial to review some

other existing systems, which work in different configurations and form images by various methods.

Some systems generate an image by raster scanning an object through a tightly focused THz beam, where either the transmitted [5] or reflected [6] radiation is measured, point-by-point. Such a system is shown in transmission mode in Figure 1-1. This system is good for getting a high THz brightness on one spot of interest, thereby yielding high signal-to-noise ratio (SNR) images. The system can also achieve good transverse resolution by using very large lenses (or mirrors). One disadvantage of this system is that it is necessary to have a thin, uniform object to stay within the Rayleigh range of the focused THz beam. Furthermore, the effects of diffraction are not often considered in such a system so it is only assumed that material properties do not re-direct the beam. Such assumptions can somewhat invalidate certain measurements such as absorption. While this system does collect some range (depth) information based on the time-delay of the pulses through the sample, it is not a true three-dimensional imaging method.

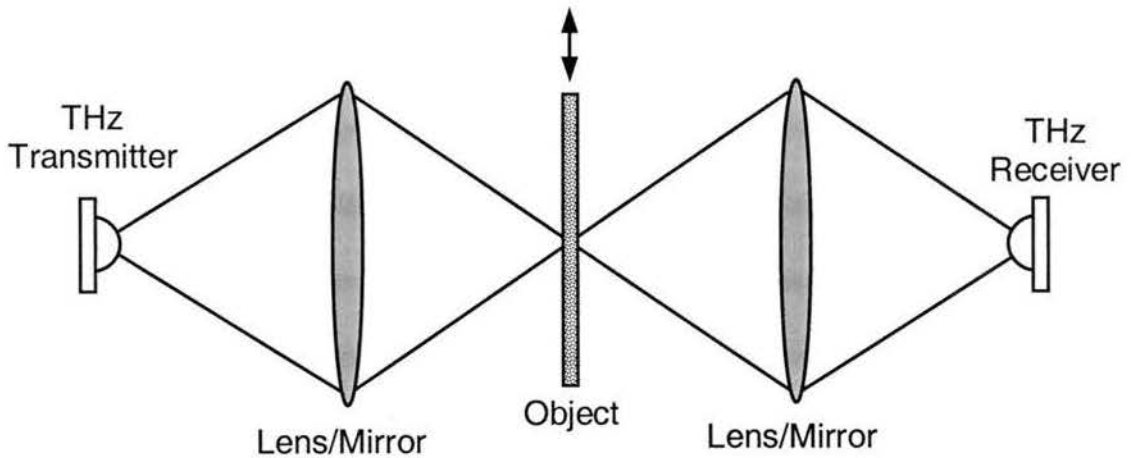


Figure 1-1. Point illumination, transmission-mode, THz imaging system.

Another type of THz imaging system already in use is shown in Figure 1-2. In this synthetic aperture, impulse imaging system [10], the object is illuminated by a THz beam and scatters a portion of the incident radiation to a receiver fixed at some bistatic angle. A large number of discrete measurements of the scattered field are taken, each with either a different rotation angle of the object or a different bistatic angle between the transmitter and receiver. Knowing the time-delays of the received pulses, the orientation of the object, and the orientations of the transmitter and receiver, it is possible (and necessary) to reconstruct the image mathematically.

With this system it is easy to synthesize a very large imaging aperture to achieve excellent cross-range (transverse) resolution in one dimension. This dimension is labeled cross-range(1) in Figure 1-2. Range resolution is also very good due to the large bandwidth of the THz pulses. However, due to necessarily complicated object or receiver orientations, it is more challenging to synthesize a large aperture in the second transverse dimension. This dimension is normal to the plane of the figure and is labeled

cross-range(2) in Figure 1-2. Therefore, high resolution in the cross-range(2) direction can be much more difficult to achieve.

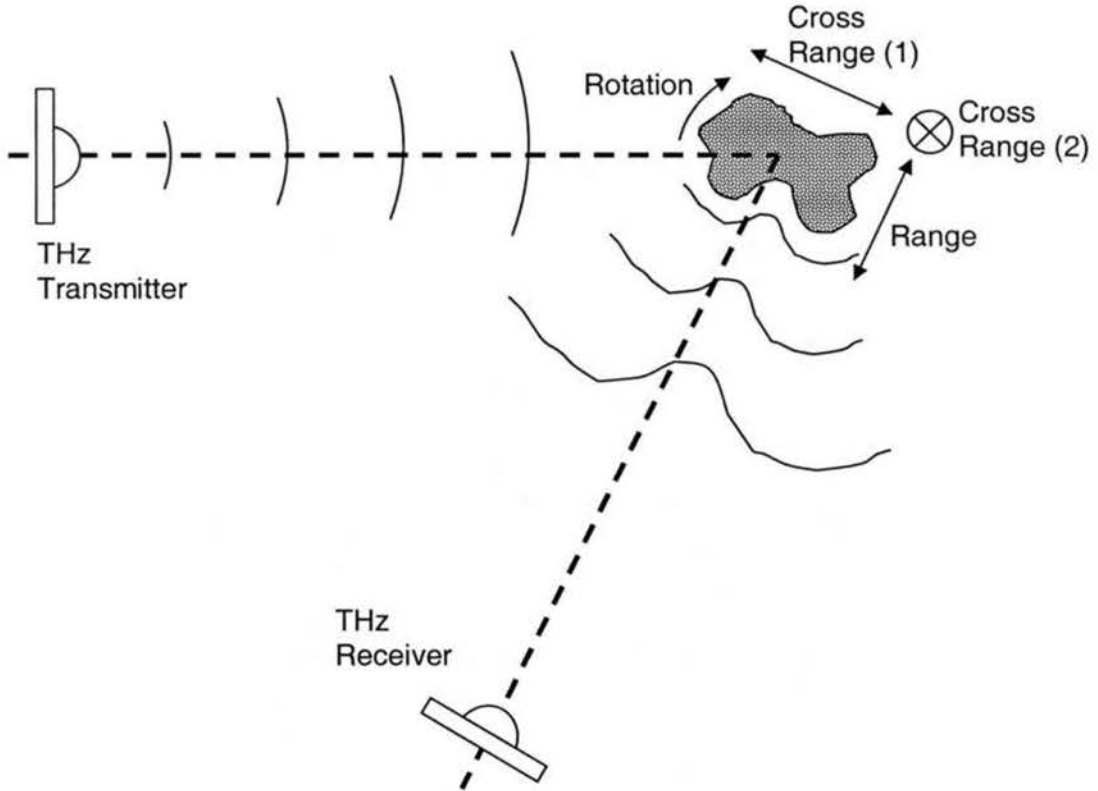


Figure 1-2. Synthetic aperture THz impulse imaging system.

Also, this system is a sparse-aperture system, meaning the synthesized imaging aperture is only sparsely filled with the discrete samples of the wavefront. As in large apertures created with antenna arrays, sparse filling can create side lobes which degrade the end appearance of an image. To avoid this problem, this impulse imaging system can require a large number of measurements to fill in the aperture.

Finally, in the impulse system, the receiver intercepts only a very small portion of the scattered wavefront at any given measurement. Therefore, if a scattered wavefront is

very weak the resulting SNR of the measurement will be very low. In this way, small objects, or any objects that don't reflect a large amount of THz radiation back to the receiver, can be difficult if not impossible to image.

Electro-optic (EO) detection techniques have also been used to generate images without scanning the sample and are excellent for THz beam profiling [7,8]. Figure 1-3 shows a simplified diagram of such a system in transmission mode. In this system, a THz beam is passed through a sample to form a shadow image on an EO crystal. A linearly polarized, pulsed laser co-propagates through the crystal with the pulsed, THz image. As they travel through the crystal, the THz electric-field induces a small rotation in the polarization of the laser via the electro-optic effect. This effectively imprints the THz image onto the laser. The newly polarized laser pulse containing the image information is then run through an analyzing polarizer and detected by a CCD camera. By changing the relative delay between the THz pulse and the laser pulse, the entire time-dependence of the THz image can be recorded. The main advantage of this system is that the entire transverse spatial profile of the image is at once recorded by the CCD camera. There is no need for image sampling except in the time-domain. In this respect, imaging can be done very quickly and without mathematical reconstruction. However, this speed generally comes at the expense of dynamic range so that it is difficult to image weakly transmissive or reflective objects with good SNR.

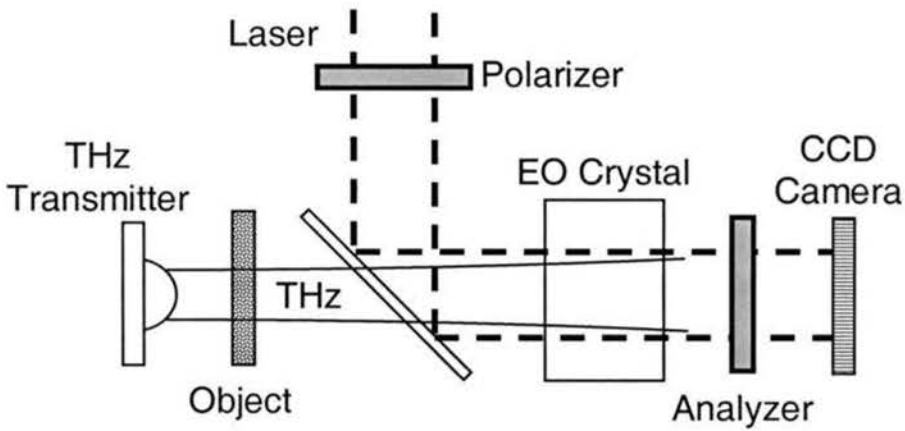


Figure 1-3. Electro-optic THz imaging system. THz beam (solid lines) co-propagates with laser beam (dashed lines).

The quasi-optic THz imaging system, presented in this dissertation, retains many of the beneficial properties of the previously described systems, while simultaneously adding other features. For the sake of pointing out some of its properties, a brief explanation of its operation is now given. A much more detailed discussion will be presented in chapter 3. Figure 1-4 shows the quasi-optic THz imaging system. In this arrangement, THz radiation illuminates the entire object, which then scatters some of the incident radiation to a large spherical imaging mirror. The mirror is positioned to collect a relatively large portion of the scattered radiation and refocus it in the form of a one-to-one image in front of a fixed THz receiver. This image is a complete, real, THz field image and is recorded, one portion at a time, by translating it in front of a fixed THz receiver.

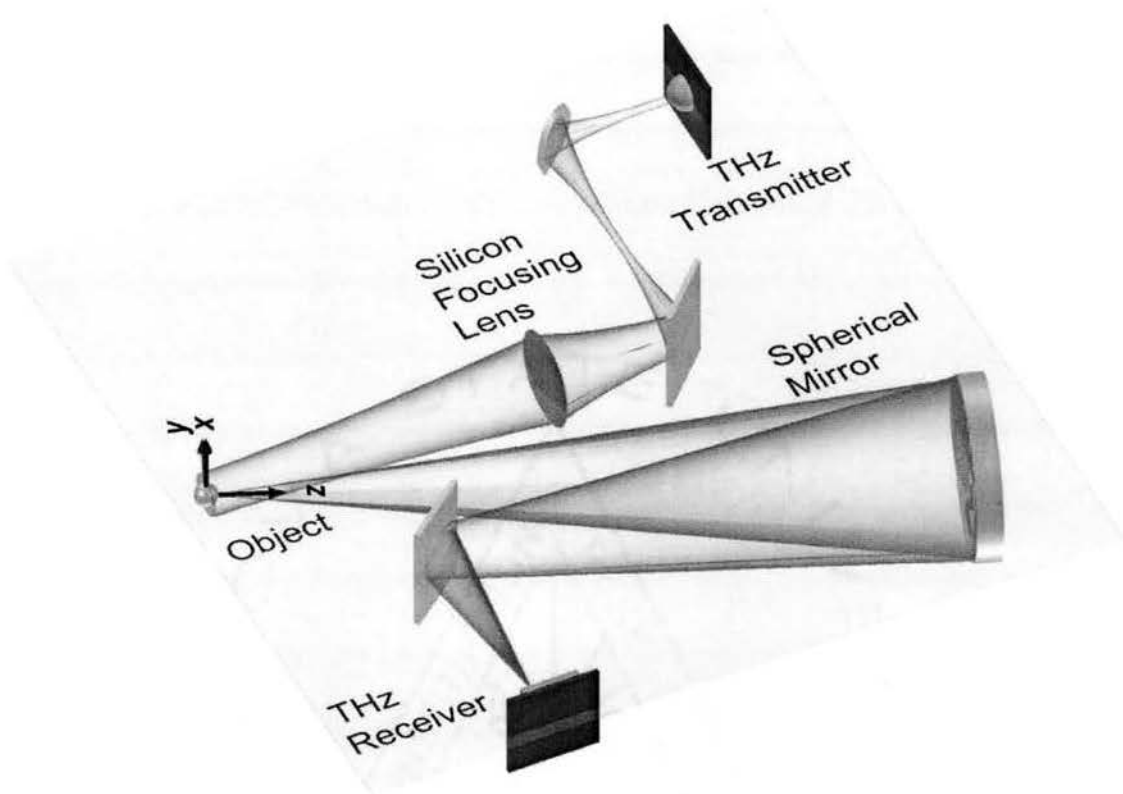


Figure 1-4. Quasi-optic THz imaging system. THz beam path is shown as translucent tubes.

The system is unique because, except for THz generation and reception, it uses optical methods exclusively to achieve imaging. Rather than illuminating an object with a pin-point beam, the entire object is illuminated and, therefore, the entire image is created at once by the spherical imaging mirror. No mathematical reconstruction of data is necessary because the image itself is sampled, not the wavefront scattered from the object. Moreover, since the THz is pulsed, the system also provides a ranging view of the object, similar to those provided by conventional radar systems. Therefore, this system behaves very much like a THz camera with the added benefit that the “film” is coherent. These properties make three-dimensional, diffraction-limited imaging of large, non-uniform, and opaque objects simple yet effective.

The spherical imaging mirror is quite large, is completely filled, and serves as the resolution defining aperture of the system. Therefore it automatically produces high-resolution images with little interference from side lobes. It also serves as a large collection optic for scattered THz radiation, making it possible to record relatively high SNR images from very small or weakly reflecting objects.

Since the system is coherent, it can also take advantage of aperture synthesis (AS), a technique whereby the resolution defining aperture in a system is synthetically increased in transverse extent. Therefore, this dissertation also presents a demonstration and theoretical explanation of an extension to the quasi-optical THz imaging system whereby multiple, coherent THz images are recorded and later combined to form a sharper image. This is called *synthetic phased-array THz imaging* and is a powerful method by which resolution can be increased using phased-array principles. Moreover, by judicious placement of the synthetic, phased-array elements, the resulting stand-alone, diffraction-limited images can be combined by simple superposition rather than complex mathematical reconstruction to form a single higher-resolution image.

1.3 Scope of the Dissertation

The purpose of chapter 2 is to provide an introduction (or review) of some fundamental optics principles and definitions which will be used extensively throughout the dissertation. The first section provides some definitions of the various components of a generalized imaging system and also discusses the paraxial approximation. The second section discusses the multi-dimensionality of THz image data and how it can be

represented and simplified with the paraxial approximation. The next section outlines various definitions of resolution and which ones are applicable to the THz imaging system and why. The last section introduces a few basic spatial-frequency concepts, which are common to the study of Fourier optics and are occasionally useful in discussing the THz imaging system.

Chapter 3 provides a detailed description of the experimental setup of the quasi-optic THz imaging system. The general layout is discussed first and is followed by a detailed discussion of how a THz image is actually produced and recorded, including more detail about the roles of the individual components. Finally a link between THz imaging and ultrasonic imaging is presented.

Chapter 4 presents the experimental results of one-dimensional point source imaging [21]. Several images, generated under various conditions, are presented and used to verify that the system is diffraction limited. One image of a dual point-source object is presented along with some unique resolution features of the system.

Chapter 5 extends the work of chapter 4 into two-dimensional, synthetic phased-array THz imaging [22]. First, a brief history of aperture synthesis is presented, followed by a discussion of how it might be applied to the THz imaging system. The actual realization of AS by using a synthetic phased-array is then discussed. Next, some conditions for proper operation, such as phase references and object placement accuracy, are presented. Several experiments are then presented wherein different objects are imaged using the synthetic phased-array method. Interspersed within these discussions are some of the more subtle details of the operation of the system. These include the establishment of proper relative phase between array elements, the various methods by

which three-dimensional image data can be displayed on two-dimensional paper, and some image analysis and enhancement techniques. Some other important details, including object stealth behavior, multi-path effects, and array steering are also discussed.

The purpose of chapter 6 is to present a theoretical explanation of all the experimental work. The general approach to modeling is presented first, and is followed by some discussion of approximations, notation, and some comparisons to typical optical and radio systems. Three different theoretical models are then discussed in both the monochromatic and broadband contexts. The results of each method are displayed in the same form for comparison. Finally, using the last model, several theoretical images, generated to mimic the experimental data, are presented with actual data, for comparison. Chapter 7 provides a brief summary of the work and presents some conclusions.

Chapter 2

Imaging Systems and Resolution

To facilitate the understanding of the THz imaging system this chapter provides a brief overview of some imaging principles. A basic understanding of geometric optics and elementary diffraction theory is assumed. The definitions and principles introduced in this chapter are standard notation as found in references [23-25] and will be used consistently in describing the THz imaging system.

2.1 General Imaging Systems

Figure 2-1 shows the model of a basic imaging system. The *object* occupies some region of space, called the *object space*, and some set of optics is used to form an imperfect representation of the object, called the *image*, somewhere in a separate space called the *image space*. If a cone of rays diverging from some object point is perfectly transformed into a cone of rays converging through an image point, the system is said to be *stigmatic* for these two points. In other words, the imaging is perfect between these two points, neglecting diffraction. The points themselves are called *conjugate points*. A *well-corrected* imaging system is defined as one that transforms the diverging spherical wavefront emitted by a point object into a converging spherical wavefront centered at the

geometrical image point [26, Chap. 3]. Such a system is obviously stigmatic and suffers no aberrations, so its resolution is limited by diffraction.

Most imaging systems, however, are designed to form quality images between two surfaces comprised of a set of conjugate points. These can be referred to as the *object surface* and the *image surface*. In general these surfaces are curved, but for simplicity, they will now be assumed to be planar and shall henceforth be referred to as the object plane and image plane, or geometric image plane. The image plane can also be defined as that plane in which the projected image is the most accurate representation of the object [23, Sec. 5.3.1]. Assuming fixed optics and a fixed object plane we can equivalently define the geometric image plane as the plane wherein imaging is most stigmatic (most perfect). Not surprisingly, the geometric image plane is also where geometric optics predicts the image to lie.

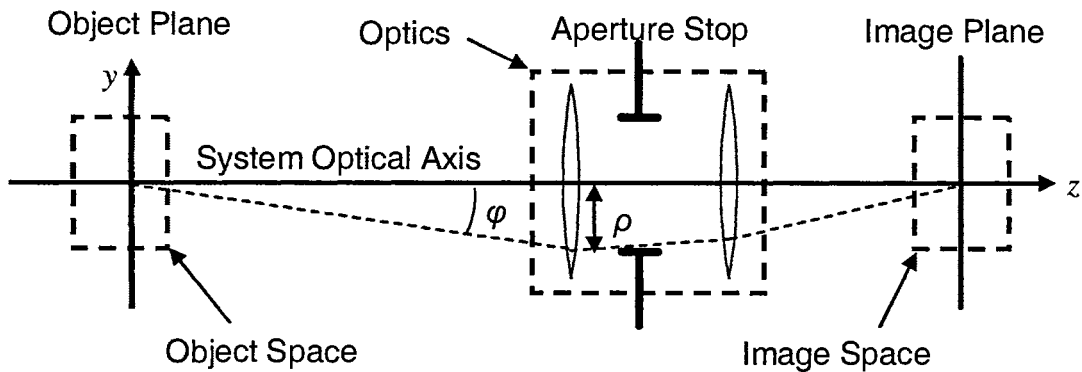


Figure 2-1. Basic imaging system diagram. Light dashed lines indicate the path of one ray through the system and φ is its angular separation from the system optical axis.

The components of the system are situated along the system optical axis, which is in general, normal to the object and image planes. The system optical axis can be

regarded as the central path around which a bundle of rays, issuing from the object, propagates as it passes through the optics and to the image plane.

A distinction is made here between the system optical axis and the symmetry axes of the individual optical components. Consider an off-axis imaging system, as shown in Figure 2-2, wherein a spherical mirror is used for the single optical component. The symmetry axis of the mirror is the one around which the mirror has rotational symmetry. This axis is not coincident with the system optical axis, in this case, but is angularly separated from it by the off-axis angle, α . This distinction is important for off-axis imaging systems because some image aberrations are functions of α .

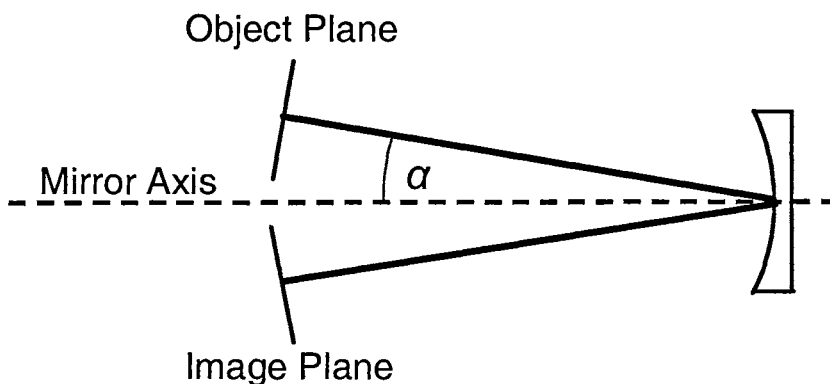


Figure 2-2. Off-axis imaging system with off-axis angle, α . System optical axis (heavy line) lies at an angle, α , with respect to mirror rotational axis (dotted line).

Most imaging systems operate on a bundle of rays whose divergence from the system optical axis subtends only a small angle, φ , such that $\sin(\varphi) \approx \varphi$, and whose maximum transverse extent, ρ , is limited, as shown in Figure 2-1. Such systems satisfy the *paraxial approximation*, which allows the effects of optics on the ray bundle to be more easily predicted and quantified. The *aperture stop* is used to limit the maximum transverse extent of the bundle of rays. Sometimes, as in the case for the THz imaging

system, the aperture stop is defined by the rim of a lens or mirror and is not a separate diaphragm or iris, like the one shown in Figure 2-1.

The *exit pupil* of a system is defined as the image of the aperture stop as seen from an axial point on the image plane through the interposed lenses, if there are any [24, Sec. 5.3.2]. More simply, this pupil defines how angularly large the most limiting aperture in the system appears from the vantage of the axial image point. The exit pupil is important in diffraction calculations and will be discussed more in chapter 6.

2.2 Image Representation

Consider a hypothetical data set comprised of intensity measurements for an imaging system whose optical axis lies parallel to the z -axis, like the one in Figure 2-1. For monochromatic light, these measurements can represent an image located in the image plane. Such an image could be represented by the variable $I(x,y)$. To represent the intensity distribution over all image space, rather than on the image plane alone, the image variable would become $I(x,y,z)$. Now, if the light source was pulsed or broadband, the image would be time-varying and could be represented by $I(x,y,z,t)$. Similarly $E(x,y,z,t)$ could represent the electric field distribution in the image space, which, by nature, is time-varying. Neglecting the vectorial nature of fields, this is the most general representation for an image as it incorporates the variability of all four measurable dimensions.

For paraxial rays, the dependence of E on both z and t can sometimes be considered redundant. Consider the electric field distribution in two closely spaced

planes in image space, one located at z_0 and the other at $z_1 > z_0$. Using pulsed light under the paraxial approximation, the field in z_1 at time t_1 will be almost equivalent to the field in z_0 at some earlier time t_0 , and the approximation $E(x,y,z_1,t_1) = E(x,y,z_0,t_0)$ is valid, where $t_1 - t_0 = (z_1 - z_0)/c$. This says that the pulse merely traveled from one z -plane to the other, but its transverse, spatial distribution was essentially unchanged. Therefore, in a paraxial, pulsed system, the variables z and t are linearly dependent for a field distribution over a sufficiently small image space and the field can be expressed therein as either $E(x,y,z)$ or $E(x,y,t)$. This approximate representation is valid for most cases in the THz imaging system and it allows the direct transformation of time-delays into ranging distances.

2.3 Resolution Criteria

Several criteria are used to define the transverse, spatial resolution in an imaging system. Consider the Rayleigh and Sparrow resolution criteria for monochromatic, circular-aperture imaging systems. The Rayleigh criterion states that two point sources are just resolved when, in their image, the intensity peak of one is coincident with the first intensity null of the other [24, Sec. 10.2.6]. The Sparrow criterion states that two points are just resolved when, in their image, their overall intensity profile acquires a flat top [24, Sec. 10.2.6]. These criteria are shown in their normalized forms in Figure 2-3.

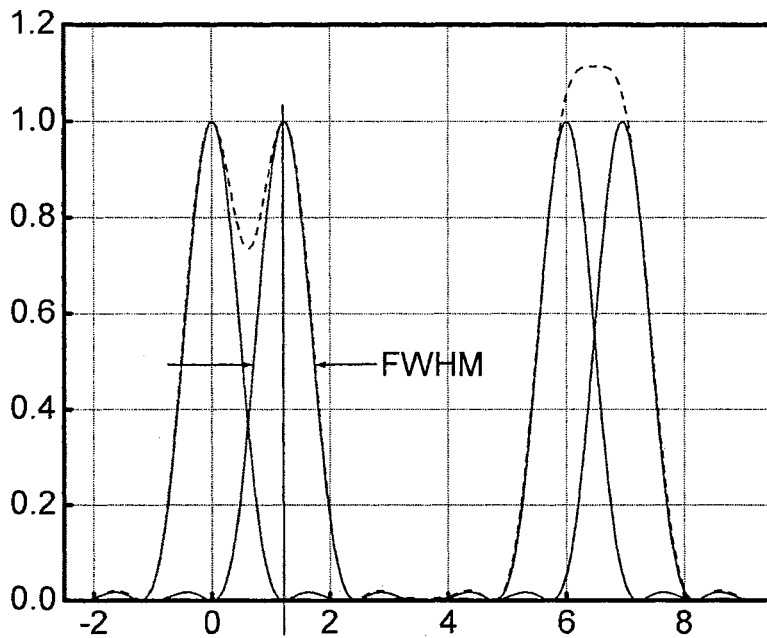


Figure 2-3. Normalized Rayleigh and Sparrow resolution criteria. Solid and dotted lines indicate individual and overall intensity profiles, respectively

Another criterion used for defining the resolution can be adapted to a single point source and is called the Buxton criterion. It specifies that two point sources are resolved when the distance between the central maxima of the composite *amplitude* distribution is equal to the full width at half-maximum (FWHM) of the diffraction pattern of either point source [27]. Since resolution is defined by the FWHM of either pattern, it can similarly be applied to a single source. In this case resolution is a measure of the FWHM of the main lobe of the amplitude profile and higher resolution accompanies lower FWHM measurements. This FWHM criterion is used in the discussion of the THz imaging system.

Like radar, the THz system is a pulsed system, and also has the ability to discriminate objects based on their range. Its range resolution is determined by the temporal length (and hence the bandwidth) of the THz pulse. Two object features are

considered resolved in time if their reflections do not greatly overlap. Using the radar ranging formula, range resolution is on the order of $c\tau/2$, where τ is the pulse duration. One criterion useful for quantifying this resolution is the Schuster criterion. Like the Rayleigh and Sparrow criteria it is generally applied to spatial intensity patterns. It states that two sources are resolved when no portion of the main lobe of the diffraction pattern overlaps with the main lobe of the other [27]. A variation of this criterion can be used to quantify the minimum temporal separation between two resolvable THz pulses. It specifies that two pulses, separated by τ , are just resolved when τ is the temporal distance between zero-crossings of a THz pulse. This criterion works well and was used for the THz imaging system.

2.4 Spatial Frequencies

Analogous to time-domain signals, images are spatial-domain signals and can be decomposed into their spectral components, called spatial frequencies. Whereas high frequencies are necessary to obtain sharp temporal features in a time-domain signal, high spatial frequencies are necessary to obtain sharp spatial features (high resolution) in an image. Sampling rules follow similar relationships. To acquire an accurate discrete representation of a continuous image, sampling points must be sufficiently dense such that aliasing doesn't occur for the higher spatial frequencies. All the images recorded by the THz imaging system satisfied these sampling requirements.

The spatial frequency bandwidth of an image is determined by the wavelength of the radiation employed and the angular extent of the exit pupil in the system. The

resolution of an imaging system is also determined by the same two factors, so it is not surprising that resolution is highly related to spatial frequency bandwidth.

Following the notation of [24,30], spatial frequencies can be determined by simple geometry. Consider the optical system shown in Figure 2-4. The spherical wave issuing from the aperture and converging to point O can be decomposed into a set of plane waves, or rays. One such ray, coming from the edge of the aperture, intersects the optical axis with an angle φ . The figure shows several wavefronts of this ray as dashed lines, one of which passes through O . The immediate neighboring wavefront crosses the y axis at some point P_y . The distance between the wavefronts is just the wavelength of the radiation, λ , and the distance between O and P_y can be thought of as the spatial wavelength, λ_y . It is related to the angular spatial frequency, k_y , by

$$k_y = 2\pi / \lambda_y \quad (2-1)$$

and its value is determined by

$$\lambda_y = \lambda / \sin(\varphi). \quad (2-2)$$

The highest spatial frequencies are therefore generated from rays having minimum λ and originating from the edge of the aperture, where φ is maximized.

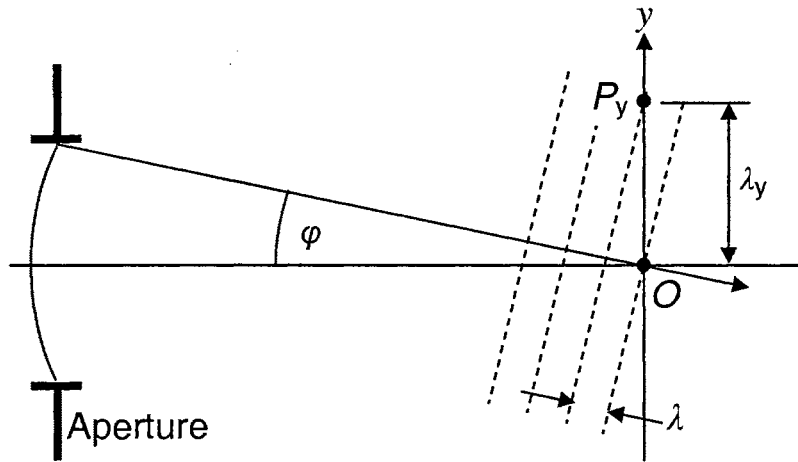


Figure 2-4. Spatial frequency determination. Wavefronts are denoted by dashed lines.

It is noted that the angular spatial frequency, k_y , is merely the y -component of the \mathbf{k} -vector of the plane wave and the overall wavenumber, k , of the plane wave is equal to $\sqrt{k_x^2 + k_y^2 + k_z^2} = 2\pi/\lambda$.

These concepts can be easily linked to imaging system resolution. For a monochromatic imaging system, operating at some frequency $f = c/\lambda$, no object features smaller than the shortest spatial wavelength, λ_y , should be spatially resolvable in the y -direction. However, even if high spatial frequencies are available from highly off-axis portions of aperture, imaging quality suffers unless the remaining aperture is filled. Consider the imaging system shown in Figure 2-5a. This system has an annular aperture which passes high spatial frequencies but filters out low spatial frequencies. It has a low spatial frequency bandwidth (small $\Delta\phi$) because the aperture is not filled. Such a system could only produce an image of the sharp features of an object, but could not produce an image of the slowly-varying, or smooth, features of the object. Similarly, the system shown in Figure 2-5b has only low spatial frequencies. Such a system could only accurately produce an image of the smooth features of the object. However, if both

systems were added together, the image could have both sharp and smooth features and more exactly represent the object. This is completely analogous to time-domain signal processing wherein a certain continuum of frequency components is necessary to exactly create any arbitrary waveform.

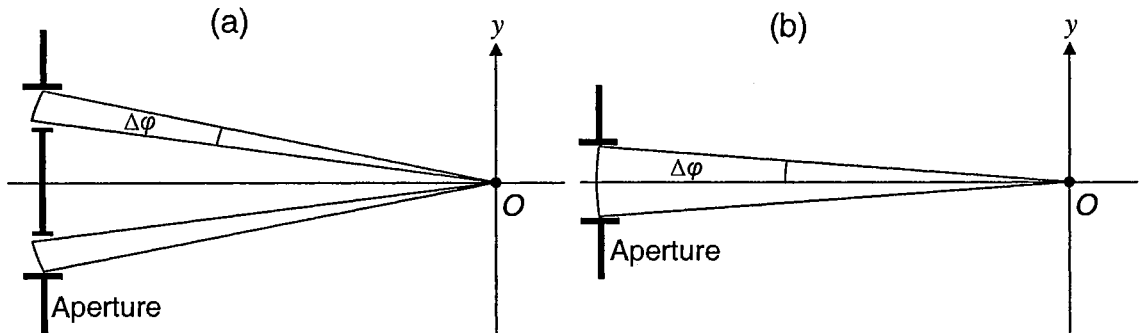


Figure 2-5. Low spatial frequency bandwidth imaging systems. (a) system filters out low spatial frequencies, (b) system filters out high spatial frequencies.

Therefore, in order to form the most accurate image of an object it is necessary to fill in the aperture, or provide large spatial frequency bandwidth. Such concepts form the basis for many image processing techniques such as edge detection and image smoothing.

Chapter 3

Experimental Setup

3.1 General Layout

The overall experimental setup is shown in Figure 3-1 and consists of an optoelectronic THz transmitter and receiver, illumination optics, an object and collection optics. To make things clearer, the detailed discussion of the transmitter and receiver is deferred until the next section.

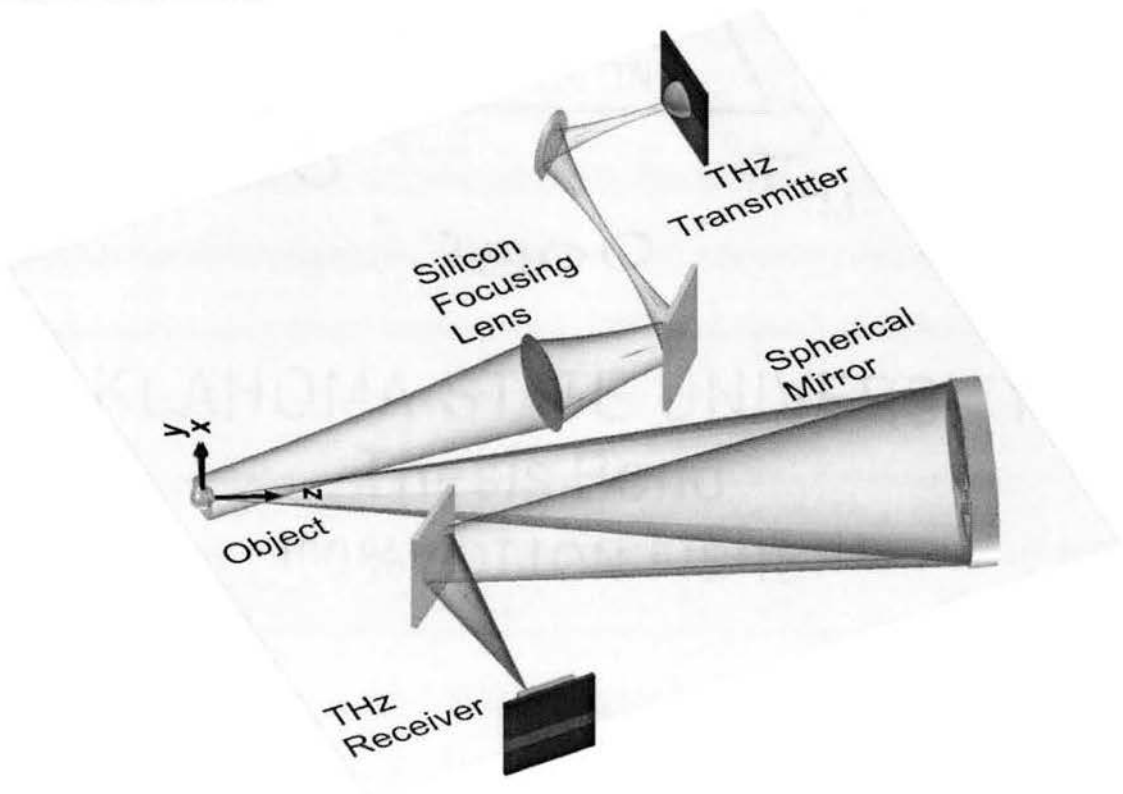


Figure 3-1. THz imaging system. The THz path is indicated by the translucent “tubes”. In this figure the object is a small sphere.

The illumination optics consist of a paraboloidal mirror placed just in front of the transmitter, a flat mirror and a silicon focusing lens, all of which serve to efficiently direct and brighten the illumination on the object. The paraboloidal mirror has a focal length of 119 mm and is placed 119 mm in front of the transmitter. The 50 mm diameter silicon focusing lens is made of high-resistivity silicon (Resistivity $\approx 10^4$ ohm-cm), has a focal length of 280 mm and is placed 280 mm upstream from the object.

The collection optics consist of a spherical mirror and a second flat mirror, which focus and direct scattered THz radiation to the receiver. The spherical mirror is a 152.4 mm diameter optical-grade mirror with a radius of curvature of 610 mm and a focal length of 305 mm. It is an aluminum-coated telescope mirror with a silicon-monoxide (SiO) protective coating.

The overall layout of the system is designed to minimize imaging aberrations, such as astigmatism and coma, while maintaining practical functionality. All the components of the system lie centered in $y = 0$ plane. In order to further discuss the layout, shown in a plan view in Figure 3-2, it is convenient to define some axes within the system. The central axis extending from the object to the spherical mirror, back to the second flat mirror and finally to the THz receiver is the system optical axis, as defined in chapter 2. The axis extending from the first flat mirror through the silicon focusing lens and to the object is called the illumination axis. The illumination axis and the first leg of the system optical axis subtend a 17° angle at the object. This angle prevents the silicon focusing lens from shadowing the spherical mirror from any radiation scattered by the object. Further concern for the orientation of the system optical axis is due to third-order

imaging aberrations. Two of these aberrations, astigmatism and coma, generally occur whenever an object does not lie on the symmetry axis of the imaging element, in this case the spherical mirror. Therefore the system optical axis should be made to coincide, as much as possible, with the symmetry axis of the spherical mirror. For this reason, the system is folded as much as practically possible such that the system optical axis subtends only 10° from its angle of incidence to its angle of reflection at the spherical mirror. The symmetry axis of the spherical mirror bisects the system optical axis.

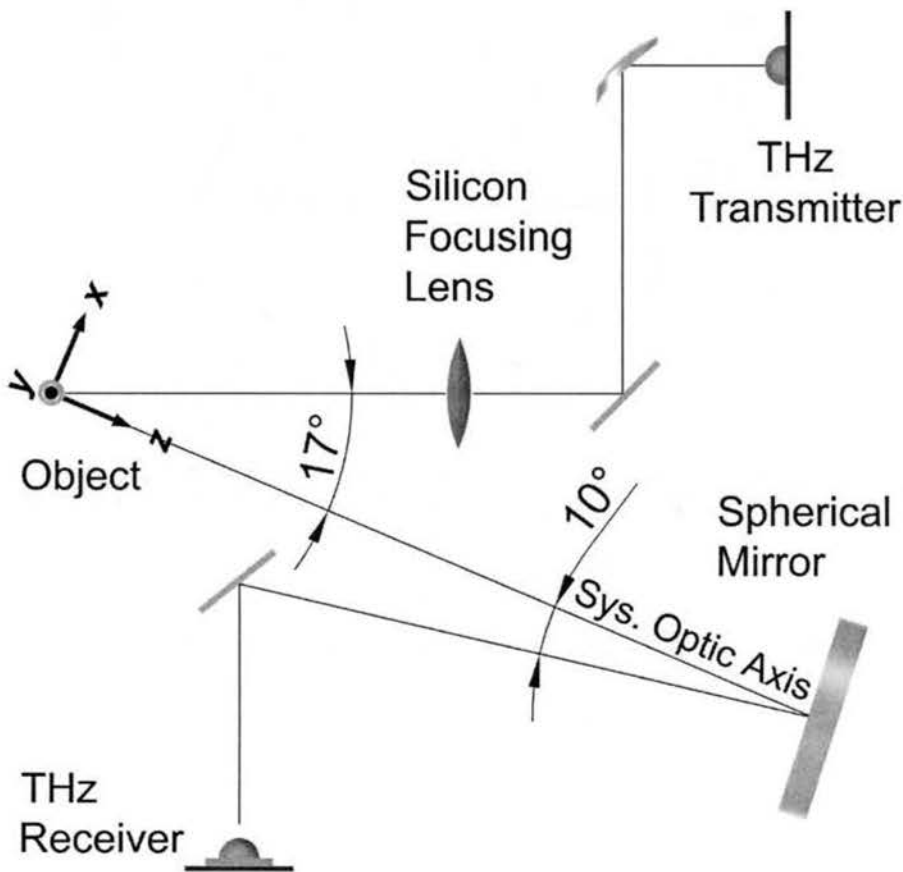


Figure 3-2. Plan view of THz imaging system.

The origin of the system is defined as the point 610 mm from the surface of the mirror on the system optical axis. The object is normally located at the system origin and is shown as such in Figures 3-1 and 3-2. The first leg of the system optical axis, from the origin to the spherical mirror, defines the direction of the positive z -axis. The plane defined by the x and y axes is then perpendicular to the system optical axis.

3.2 THz Image Production

As in references [16] and [12], subps THz pulse generation begins at the transmitter, shown in Figure 3-3, with a train of 80 fs optical pulses having a center wavelength of 801 nm and a repetition rate of 91 MHz, generated by a Kerr-lens mode-locked Ti:Sapphire laser. The optical pulses have an average power of about 25 mW and are shaped into an ellipsoidal focus by a 300 mm focal length cylindrical lens. They are then further focused by a 10 mm focal length plano-spherical lens onto the inner edge of the anode line of a coplanar transmission line on a semi-insulating GaAs chip as in reference [28]. The transmission line consists of two parallel 10 μm wide, 20 mm long, metal lines separated by 80 μm , and is shown in Figure 3-3c. The major axis of the ellipsoidal focus is parallel to the lines while the linear polarization of the optical beam is perpendicular to the lines. This arrangement enhances the THz output power [29] and allows the incident optical power to be increased without damage to the chip. The coplanar transmission line is biased between 50 V and 70 V to accelerate the free carriers generated by each optical pulse as it creates a temporary electron-hole plasma in the gap between the biased lines. The accelerated carriers subsequently radiate a near single-cycle electromagnetic pulse of

THz radiation, linearly polarized in the direction of the bias field and having frequencies ranging from about 0.050 to 2.5 THz. Much of this THz radiation is collected by a 10 mm diameter hyper-hemispherical lens, made of high-resistivity silicon and attached to the back of the GaAs chip. The lens focus is coincident with the optical focus on the transmission line, so the lens collimates the THz radiation and emits it as a highly directional, freely-propagating beam. This chip, lens combination, as a whole, constitutes the transmitter of the system.

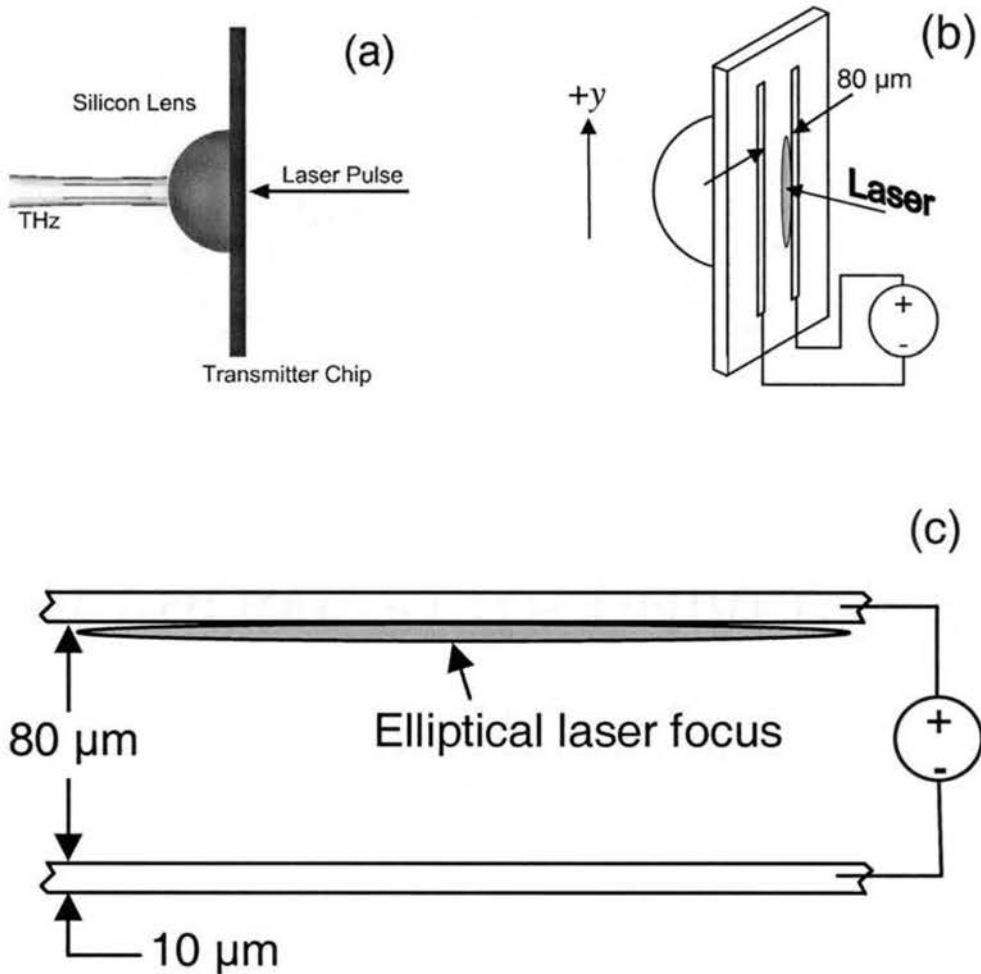


Figure 3-3. THz transmitter details. (a) side view of assembly, (b) view of assembly showing transmission line orientation, (c) scale diagram of coplanar lines on chip and elliptical laser focus (shown in gray).

After leaving the transmitter, the radiation propagates to an off-axis paraboloidal mirror, which re-collimates the beam and directs it toward a flat mirror. The flat mirror then redirects the beam toward the object. On the way to the object, the beam passes through the aforementioned silicon focusing lens. This lens has a focal length of 280 mm and is located 280 mm upstream from the object, thus forming a frequency independent illumination spot on the object. This spot has a $1/e$ amplitude beam diameter of approximately 14 mm.

As in previous THz ranging systems [31], the object is illuminated by the THz beam and subsequently scatters some of the incident radiation to the collection optics and the THz receiver. However, in the quasi-optic THz imaging system, the scattered radiation is collected by the spherical mirror located 610 mm from the object. The focal length of the spherical mirror is 305 mm so it projects a real, inverted, one-to-one THz image of the object toward the second flat mirror. The flat mirror redirects this image so that it falls in front of the fixed THz receiver. The receiver is located 627 mm from the spherical mirror measured along the system optical axis. Therefore the one-to-one image is located approximately 17 mm in front of the receiver.

Like the transmitter, the THz receiver, shown in Figure 3-4, is comprised of a 10 mm diameter hyper-hemispherical silicon lens, made from high-resistivity silicon, mounted with an optoelectronic semiconductor chip similar to those used in previous THz work [16]. The chip is made from ion-implanted silicon-on-sapphire (SOS) and a 50 μm , polarization-sensitive dipole antenna is mounted on its surface. A detailed view of the receiver chip is shown in Figure 3-4c. Between the silicon lens and the SOS chip are mounted two 500 μm thick, optically polished shims of high-resistivity silicon. The

shims serve to place the focal point of the silicon lens 1 mm in front of the dipole antenna. In this way, the image, formed by the spherical mirror and located 17 mm in front of the silicon lens, is once again imaged with size reduction and inversion onto the image plane of the silicon lens wherein lies the receiver's dipole antenna. Figure 3-5 shows a diagram of this imaging.

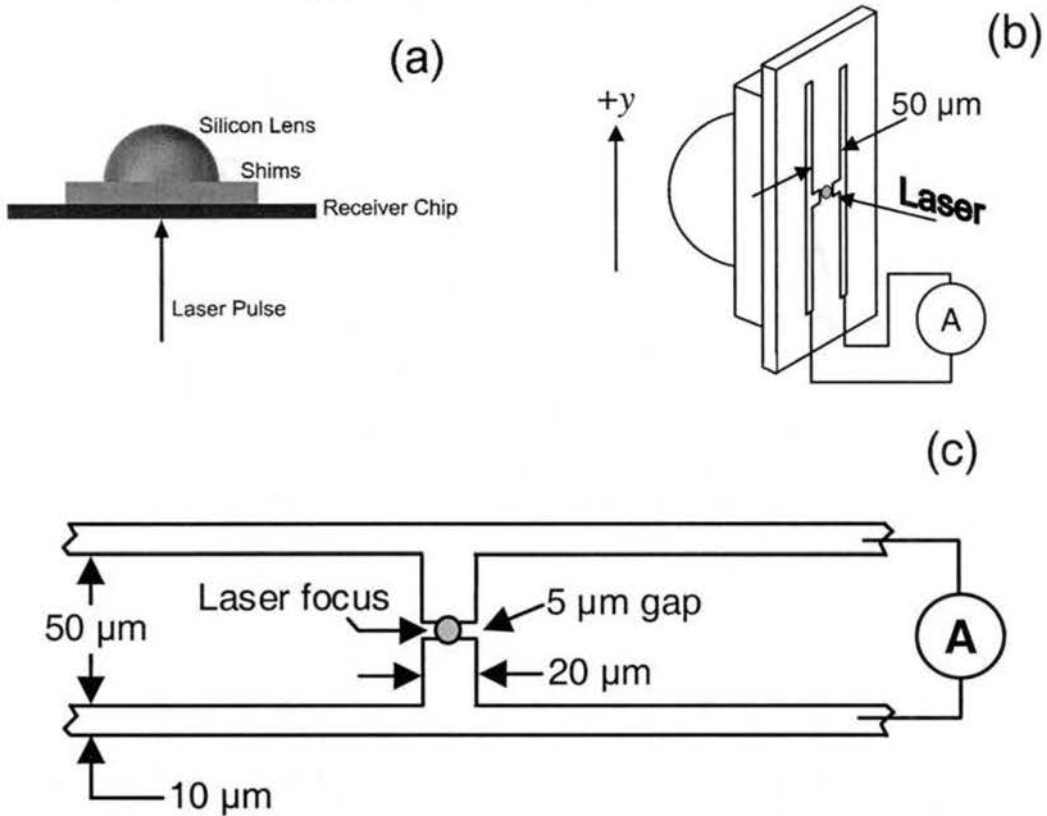


Figure 3-4. THz receiver details. (a) side view of assembly, (b) view of assembly showing antenna orientation, (c) scale diagram of receiver chip with dipole antenna and laser focus (shown in gray).

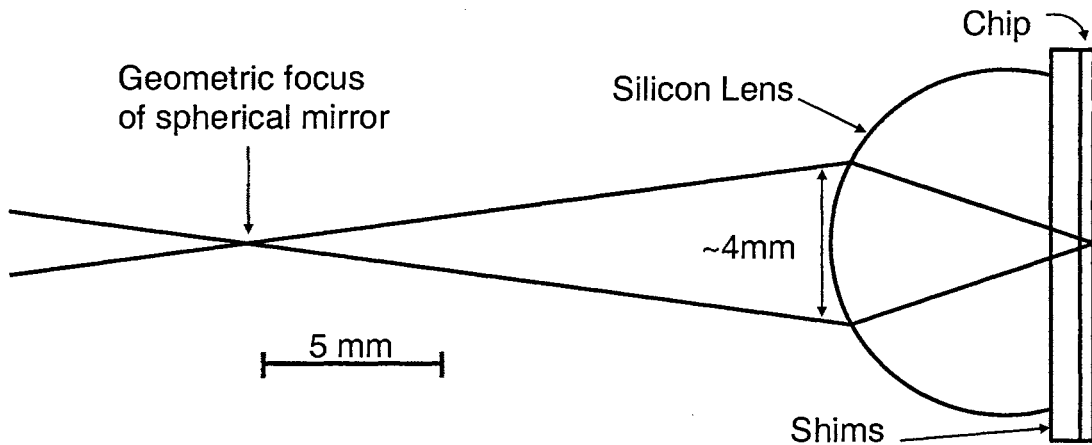


Figure 3-5. Scale diagram of imaging through hyper-hemispherical silicon lens.

With the THz image projected on it, the dipole antenna is photoconductively switched by a second 80 fs optical pulse, split from the first and appropriately delayed in time. The optical pulse train arrives at the receiver with an average power of about 11 mW and is focused onto the gap between the poles of the antenna by a 10 mm focal length, plano-convex lens. Each pulse produces free carriers that generate a DC current proportional to the instantaneous electric field amplitude of the incident THz pulse. By measuring this current while changing the relative delay between the detected THz pulse and the optical gating pulse, the entire time-dependence of the THz pulse can be recorded.

To increase the signal-to-noise ratio (SNR), the THz radiation is passed through an optical chopper just after it exits the transmitter. A lock-in amplifier is used to measure the small average receiver current modulated at the chopper frequency. A computer is used to poll the lock-in and record the data. The resulting THz record has a typical SNR of about 100 and preserves both phase and amplitude information, but represents the measurement of only a single spatial point in the image; a single spatial

sample, $E(t)$, for some constant x , y and z .

In order to record an entire image, the image must be translated in front of the receiver and sampled point-by-point. To preserve laser alignment and absolute pulse timing information, everything in the system, except the object, is fixed in its position. Due to the optical imaging configuration, translating the object creates the necessary one-to-one translation of the image in front of the receiver. Similarly, the reduced image projected onto the receiver's antenna translates proportionally. A single measurement (spatial sample) is recorded while the object is fixed at some position (x_0, y_0, z_0) . The result is a time-dependent measurement $E(x_0, y_0, z_0, t)$, a current (in picoamperes) versus time-delay (in picoseconds) measurement, where, as stated before, the measured current is proportional to the electric field amplitude. This process is repeated for different positions of the object in (x, y, z) and each measurement is a sample of the overall image. The final resulting data set consists of a set of time-dependent field measurements, one for every spatial sample point. Since the data is recorded in digital form, each time-dependent measurement is a waveform consisting of a collection of discrete temporal measurements. These are *temporal* samples of the time-dependent waveform and must be distinguished from the previously mentioned *spatial* samples of the image. Typically, spatial samples are separated by 100-150 μm in both the x and y directions and each spatial sample waveform consists of 256 discrete temporal measurements spaced by either 33.3 fs or 66.7 fs.

Figure 3-6 shows a detailed view of the object mounting apparatus. In order to translate the object (and image), it is mounted on two perpendicular, motorized, linear-translation stages. This allows the object to be translated anywhere within a single xy -

plane, normally oriented perpendicular to the system optical axis (z -axis). The translation stages themselves are mounted on a custom fabricated goniometric and rotary combination stage. This allows the plane of translation (or scan plane) to be tilted with respect to the system optical axis, while keeping the object nearly fixed in space. The goniometric stage allows the scan plane to be rotated or tilted about the x -axis and the rotary stage allows it to be tilted about the y -axis. During any single image recording, the orientation of this plane is kept constant. The motivation for tilting the scan plane is to make possible synthetic phased-array imaging, which will be explained in detail in chapter 5.

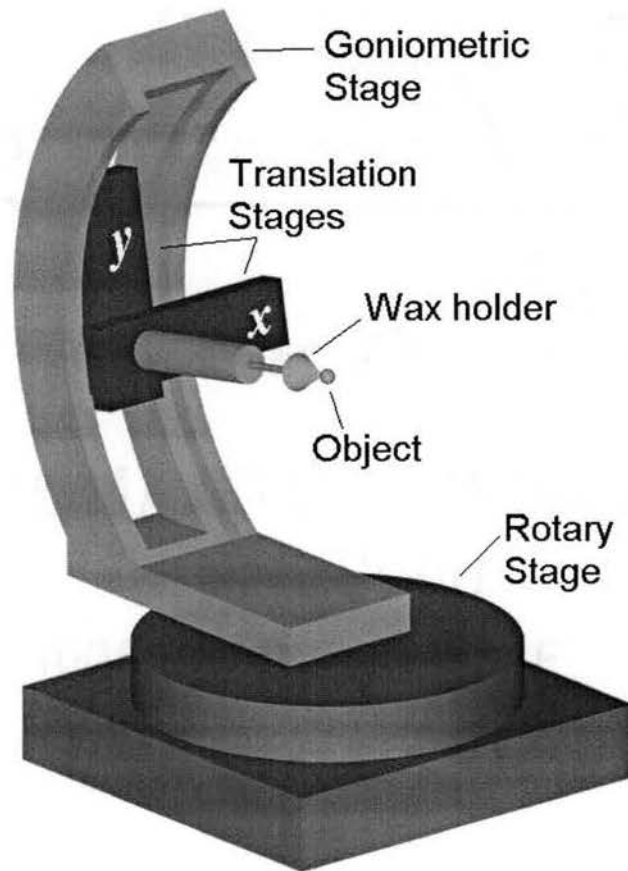


Figure 3-6. Object mounting apparatus. The motorized translation stages are marked with an x and y . Scan plane shown tilted -10° about the x -axis.

The object is mounted on the front of a paraffin wax holder, which itself is mounted to the motorized translation stages via a cantilever attached to its back. The holder is not meant to be imaged along with the object but only to serve as a mount. Therefore, it is shaped in a stealth fashion such that any radiation incident upon it will be scattered in a direction away from the spherical collection mirror. Furthermore, the paraffin holder has a low refractive index (about 1.6) for the broadband THz region [32]. Together, these two properties make the holder essentially invisible.

Since there are significant water vapor absorption lines [15] in the far-infrared region of the spectrum, the entire setup is enclosed in an air-tight box that is purged with dry air during data collection.

3.3 Link to Ultrasonic Imaging

Ultrasonic imaging is a mature technology that has much in common with THz imaging. Notably, both technologies use pulsed temporal signals to illuminate objects, and both technologies use coherent signal reception, thereby preserving both phase and amplitude information. Therefore it is not surprising that the resulting data sets have very similar forms. Following the descriptions given in [33], the similarities are easily seen.

In the THz imaging system, a single temporal measurement (single spatial sample), has the form $E(t)$. This is completely analogous to the A-scan in ultrasonic imaging, which represents the reflected ultrasonic signal as a function of time.

Further, the ultrasonic imaging B-scan is a collection of A-scans used to form a one-dimensional image. Successive A-scans are taken at different spatial locations and

together they form a two-dimensional data set of the form $A(x,t)$, a sectional amplitude image of the object. Exactly the same procedure is used to create a one-dimensional THz image. Multiple spatial samples are collected along one spatial direction and the resulting data set has the form $E(x,t)$.

Finally, a two-dimensional THz image can be formed by collecting multiple spatial samples along two directions. The result is a data set of the form $E(x,y,t)$. In ultrasonic imaging this is called a C-scan and is simply a set of A-scans collected at various spatial locations in x and y .

Chapter 4

Point Source Imaging

The first images recorded by the THz imaging system were those of objects which behaved as point sources. Such objects make it possible to determine the resolving power of the system. Particularly, the image of a point source determines the system's amplitude point spread function (PSF), or equivalently, its spatial impulse response. Since the THz system is broadband, this PSF is also broadband and applies to many frequencies at once. The system is well-corrected, so the resulting images are limited only by diffraction and measure the resolution of the system.

4.1 Single Point Source

A 1 mm diameter, chrome-plated, steel ball was used as the first object to image. To a very good approximation, this ball can be treated as a point source. This is due to the fact that short pulses are used for illuminating the object, and that the effective cross-sectional scattering area is much smaller than the ball itself. The short pulses allow the specular reflection to be temporally separated from surface waves or other higher order scattering products. Then, to isolate the specular reflection, it is only necessary to gate out the unwanted scattering data which appears later in time. Next, Figure 4-1 shows how only a

small solid angle portion of this object actually scatters specular radiation in the direction of the spherical mirror. The spherical mirror subtends only 0.049 steradians at the object, and thereby restricts all detectable rays to a maximum reflected angle of 7.1° with respect to the system optical axis. For a 1 mm ball, this restriction makes the effective visible spot only $62\ \mu\text{m}$ in diameter, sufficiently small to be considered a point source. This also makes it possible for the 1 mm ball to produce images smaller than itself, given sufficient system resolution.

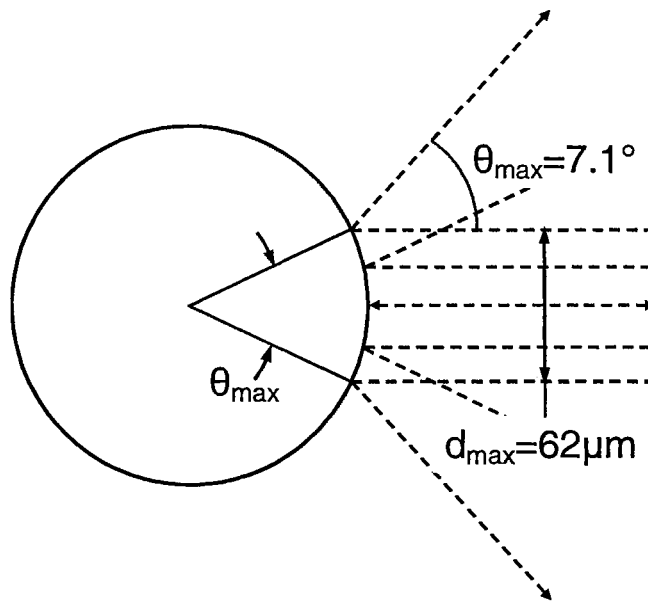


Figure 4-1. Point source justification for 1 mm ball. Dashed lines indicate incident and reflected THz rays.

The ball was scanned and sampled in the x direction only, so the resulting image was one-dimensional. The image consisted of 41 spatial samples spaced by $150\ \mu\text{m}$ thereby covering a range from $x = -3\ \text{mm}$ to $3\ \text{mm}$. To ensure the object was centered near $x = 0\ \text{mm}$ it was coarsely placed into position then adjusted slightly until the measured signal was nearly maximized. This position was then assigned the value $x = 0$.

Each spatial sample was an 8.5 ps time-dependent waveform consisting of 256 data points, each separated by 33.3 fs. The strongest of the waveforms, and its spectrum, is shown in Figure 4-2 and exhibited the peak signal-to-noise ratio for the image of 95.

Figures 4-3 and 4-4 show the image in various forms. The image can be described as a fin shape lying at some angle with respect to the x -axis. This angled orientation is shown most clearly in Figures 4-3 and 4-4b and is due to off-axis illumination of the object. As the object moves in the positive or negative x direction, the path length from the transmitter to the object changes causing earlier or later arrival times for the illuminating THz pulses to the receiver, respectively. The figures appear reversed from this situation because of the method by which they were plotted.

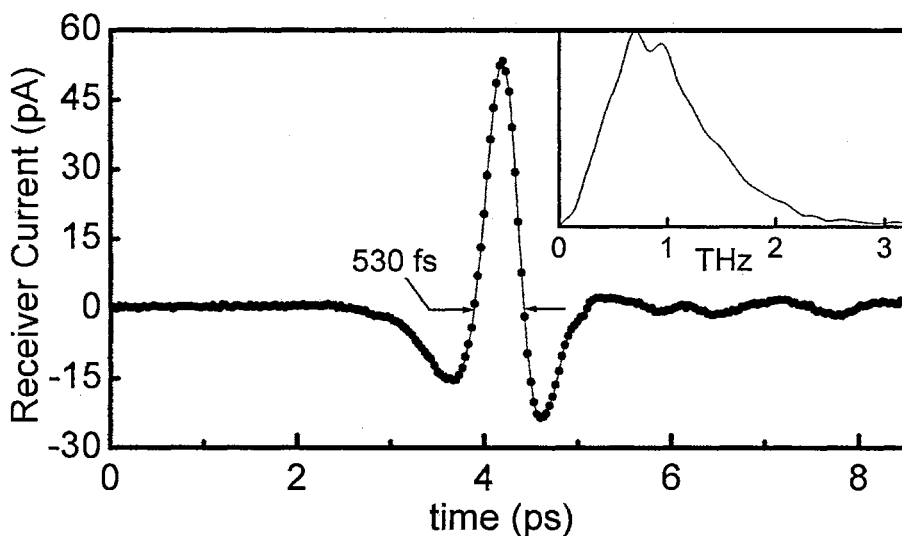


Figure 4-2. Single spatial sample ($x = 150 \mu\text{m}$) of 1 mm ball image. Data points are shown as filled circles with connecting lines for clarity. Normalized amplitude spectrum is shown inset

Due to the sampling nature of the system, as the object moves in the $+x$ direction, the receiver samples the $-x$ side of the image. Plotting the images in the fashion of Figures 4-3 and 4-4 reverses this sampling phenomenon and makes the $-x$ side of the image correspond to the $-x$ side of the object.

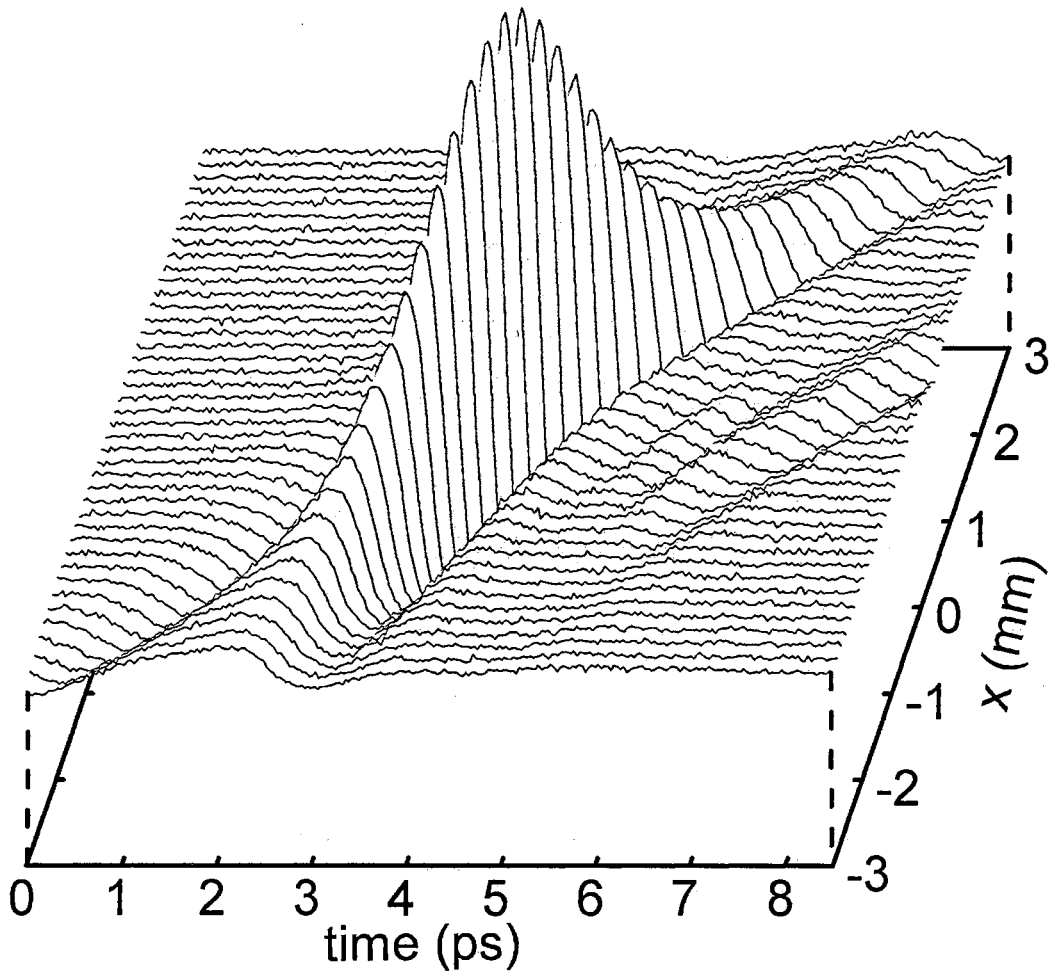


Figure 4-3. THz image of 1 mm ball. Plot is composition of curves constant in x .

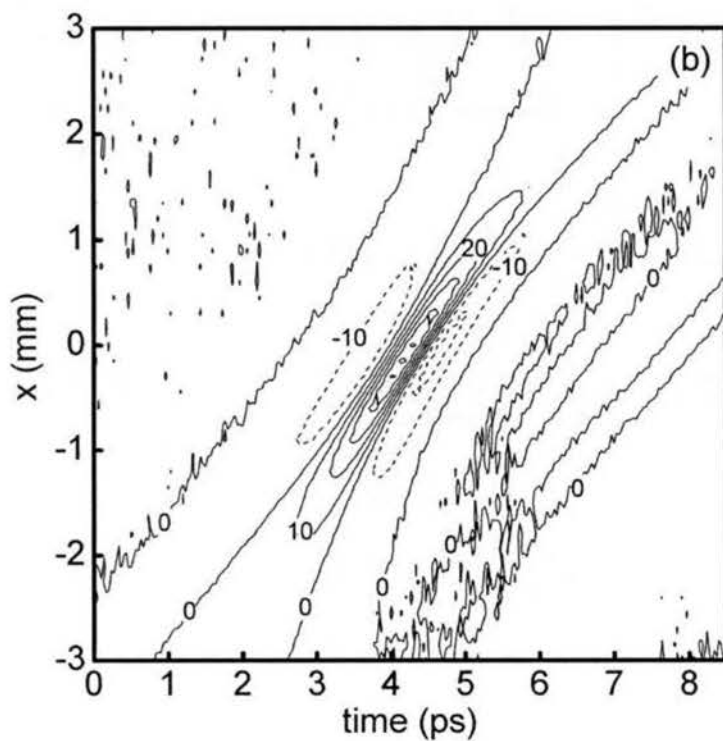
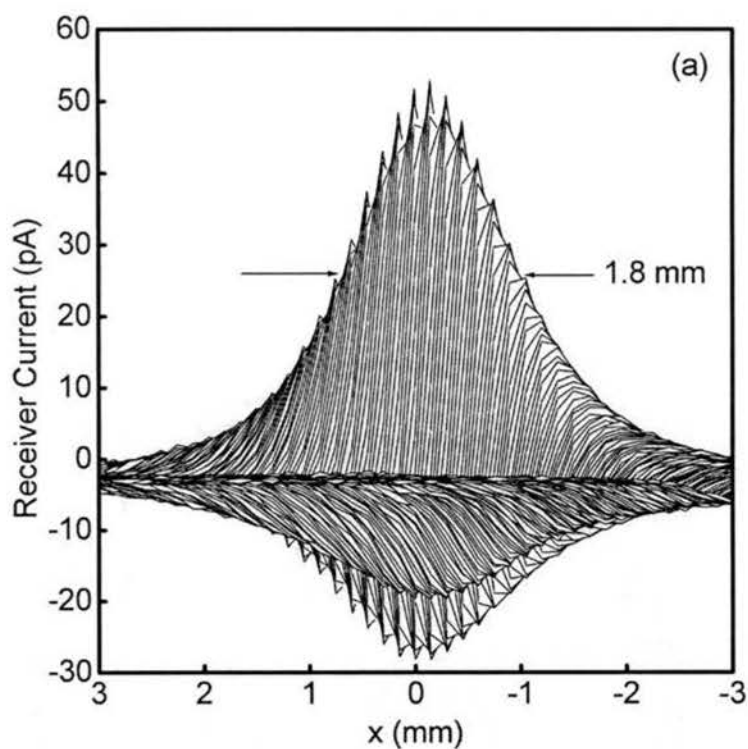


Figure 4-4. THz image of 1 mm ball. Side view (a) is a composition of curves that are constant in time. Contour plan view (b) with contour separation of 10 pA. Negative contours are indicated by dashed curves.

The images also show that the range resolution is much sharper than the spatial resolution. Using the 530 fs pulse measurement shown in Figure 4-2, the range resolution is 80 μm . The spatial resolution of the system is quantified using the FWHM measurement of the image, which is about 1.8 mm. Assuming the system is well-corrected, these values define the normal diffraction-limited resolution. Since the object is a point source, the images of Figures 4-3 and 4-4 define the broadband PSF of the system.

4.1.1 Diffraction Test by Mirror Size Reduction

To determine if the system is operating in the diffraction limit, it is necessary to know the most limiting aperture in the system. Using geometric optics, the most limiting aperture of the system can be found to be the spherical mirror. Figure 4-5 is a scaled diagram showing that rays coming from the outer edge of the spherical mirror are not further apertured by the silicon lens mounted to the receiver.

One way to test if the system was limited by diffraction was to reduce the diameter of the most limiting aperture, the spherical mirror. If the system had large geometric aberrations, reducing the mirror size would not have reduced the image size significantly. If the system was well-corrected, reducing the diameter of the spherical mirror should have produced a proportional increase in the FWHM measurement of the spatial extent of the image, noticeably worsening resolution.

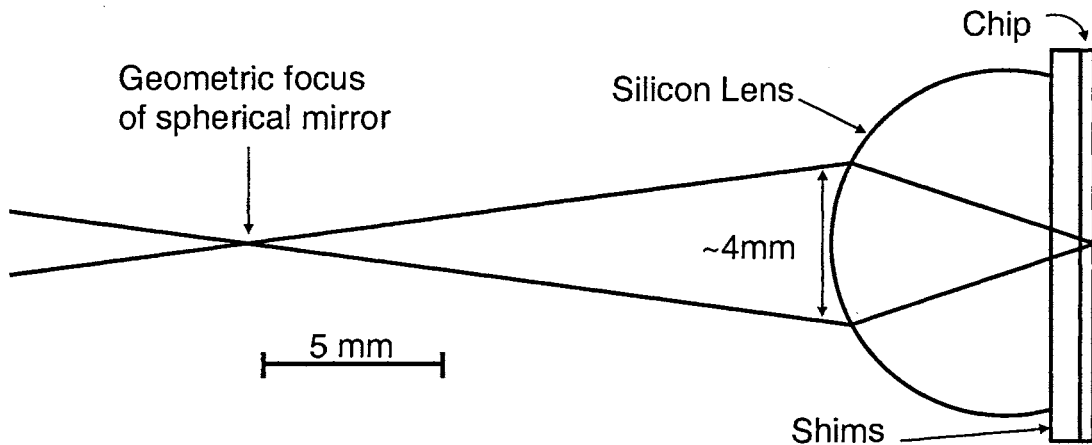


Figure 4-5. Scale diagram of geometric cone of THz rays impinging on receiver.

Therefore, the 1 mm ball experiment was performed again, this time with the spherical mirror diameter halved. To reduce the diameter of the mirror, an annular absorber was placed over the face of the spherical mirror. The absorber was a woven graphite cloth with a 76.2 mm diameter hole cut from the center. This cloth absorbs THz quite well and absorbed the THz that struck the outside annulus of the mirror.

Figures 4-6, 4-7, and 4-8 show the resulting image data. The peak signal-to-noise ratio for this image was 26. As before the image is angled with respect to the x -axis. The spatial resolution was worsened, as indicated by the increase of the FWHM extent of the image to 3.1 mm. The temporal resolution was unchanged since the profile of the THz pulse did not change.

The signal amplitude was decreased by approximately a factor of three. The expected decrease in signal amplitude was a factor of about two, since the area of the spherical mirror was reduced by a factor of four, and the field amplitude of the radiation reflected from the mirror is proportional to square root of the area. The change in spatial

resolution was 1.72 times, not exactly proportional to the decrease in aperture size. The deviations of these values from the expectations are explained presently.

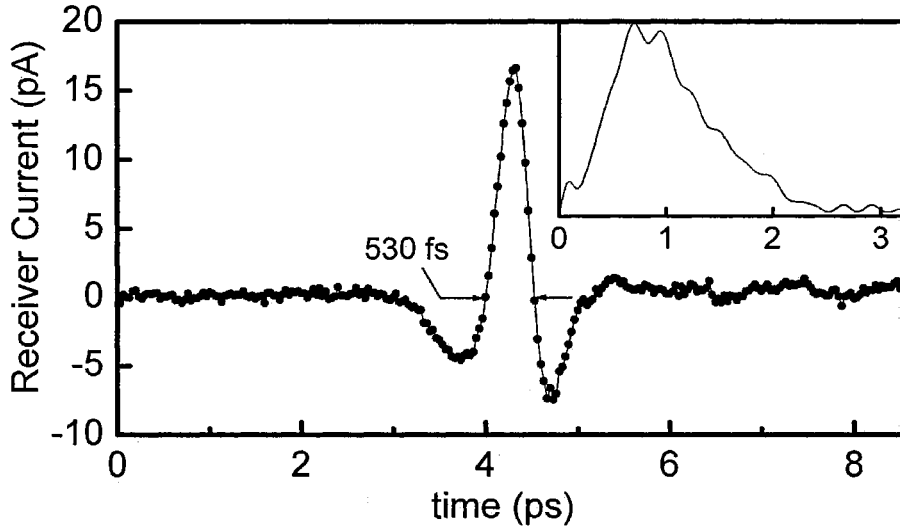


Figure 4-6. Single spatial sample ($x=0$ mm) of 1 mm ball imaged with 76.2 mm diameter spherical mirror. Data points are shown as filled circles with connecting lines for clarity. Normalized amplitude spectrum is shown inset.

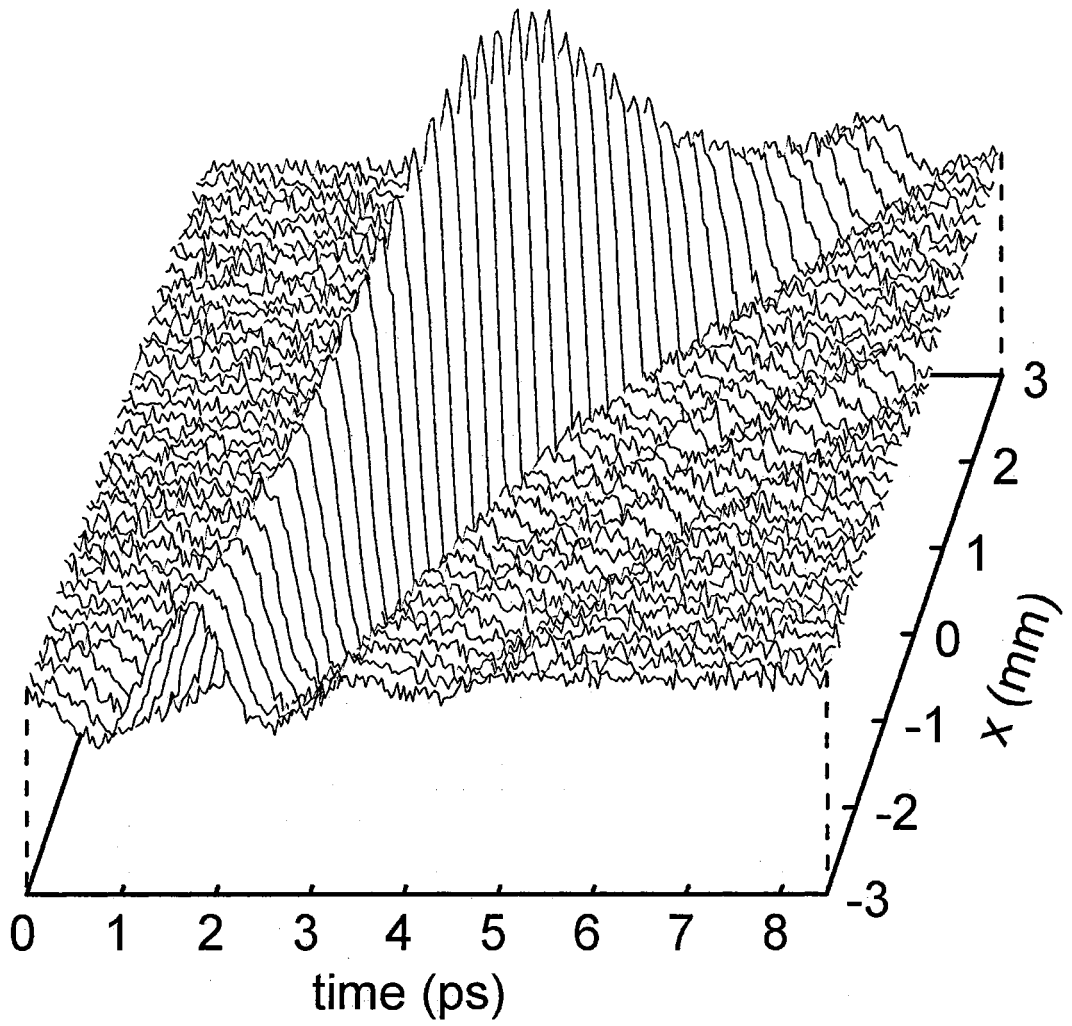


Figure 4-7. THz image of 1 mm ball imaged with 76.2 mm diameter spherical mirror. Plot is composition of curves constant in x .

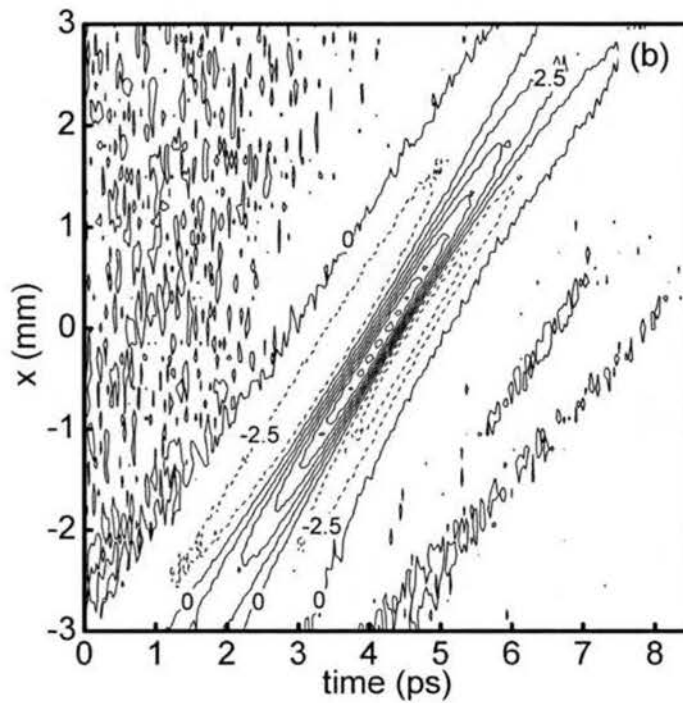
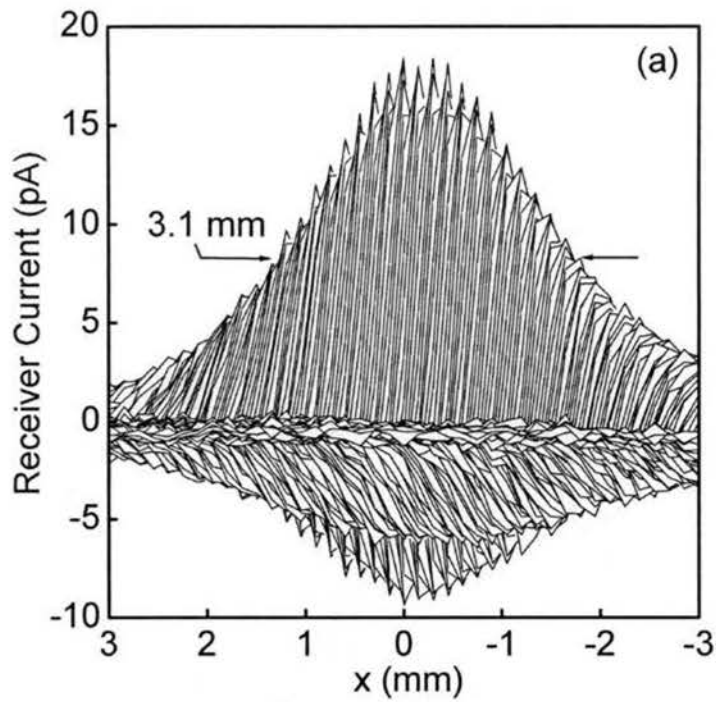


Figure 4-8. THz image of point source imaged with 76.2 mm diameter spherical mirror. Side view (a) is a composition of curves that are constant in time. Contour plan view (b) with contour separation of 2.5 pA. Negative contours are indicated by dashed curves.

First, the mismatches between the actual and expected amplitude decrease and resolution loss are not wholly unreasonable given the signal-to-noise ratios for the images. Nevertheless, the discrepancies could be explained by a minor receiver or spherical mirror misalignment, either of which would result in an excess loss of signal. The more likely explanation, however, is the combination of two effects. First, the illuminating beam is not infinite in extent but has a $1/e$ beam diameter of about 14 mm. For the smaller spherical mirror, the FWHM extent of the image is larger and therefore the object is more visible when it is further out from the peak of this illumination. The resulting illumination intensity drop causes an artificial decrease in the spatial extent of the resulting image. Second, the silicon lens in the receiver might not perfectly project the image formed by the spherical mirror onto the dipole antenna. This could not only cause the peak signal amplitude discrepancy but could also change the spatial extent of the image.

Actually, the previous discussion of discrepancies assumed the simple view that the FWHM extent of the image should double and the peak signal amplitude should halve by halving the diameter of the spherical mirror. This is not precisely the case for a broadband system due to the interference between different frequency components. As will be shown in chapter 6, halving the diameter of the spherical mirror produces an increase in the FWHM extent of the image by a factor of 1.85. If the profile of the illumination beam is taken into account, this factor reduces to 1.78, thus agreeing very well with the collected data. This not only shows that the system is operating very near to the diffraction limit but also that the effect of the receiver can essentially be disregarded. In fact, as will be shown, it was found that the receiver, as a whole,

essentially behaved as an ideal sampler of the image formed by the spherical mirror. Consideration of the peak signal amplitude is only important because it provides a practical lower limit to the extent of the spherical mirror. In other words, if the mirror is made too small, signals would become buried in noise.

4.1.2 Point Source Verification

In order to verify that the object was sufficiently small to justify the point source approximation one final test was performed. In this test the object was changed to a chrome-plated, steel ball with a diameter of $391 \pm 3 \mu\text{m}$. The graphite cloth was not present during this experiment so the aperture of the spherical mirror was the normal 152.4 mm diameter. As before, any rays impinging on the spherical mirror must fall within an angle of 7.1° from the system optical axis. For a $391 \mu\text{m}$ ball, this restriction makes the effective visible spot only $25 \mu\text{m}$ in diameter.

Figures 4-9, 4-10, and 4-11 show that the spatial resolution is almost exactly the same as that of the 1 mm ball. The $391 \mu\text{m}$ ball has a spatial FWHM measurement of 1.9 mm. This indicates that both the 1 mm ball and the $391 \mu\text{m}$ ball could be considered point sources. Similarly, with a pulse width of 560 fs, the range resolution is $84 \mu\text{m}$, almost identical to the $391 \mu\text{m}$ ball.

Two main differences in the images of the 1 mm ball and the $391 \mu\text{m}$ ball are apparent. First, the signal amplitude from the smaller ball has dropped by a factor of 2.8. This can be explained by considering the total reflecting area of the object. The diameter of the two balls differs by a factor of 2.6. Therefore the visible area on the smaller ball

was reduced by a factor of $(2.6)^2 = 6.54$, compared to the 1 mm ball. Hence the field amplitude should fall off by a factor of 2.6. This matches quite well with the actual reduction in signal amplitude.

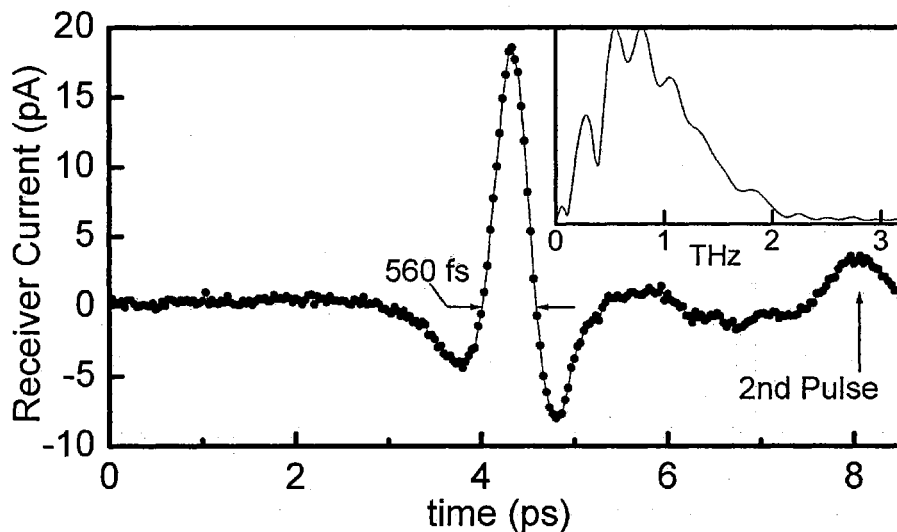


Figure 4-9. Single spatial sample ($x = 0$ mm) for the 391 μm diameter ball image. Data points are shown as filled circles with connecting lines for clarity. Normalized amplitude spectrum is shown inset.

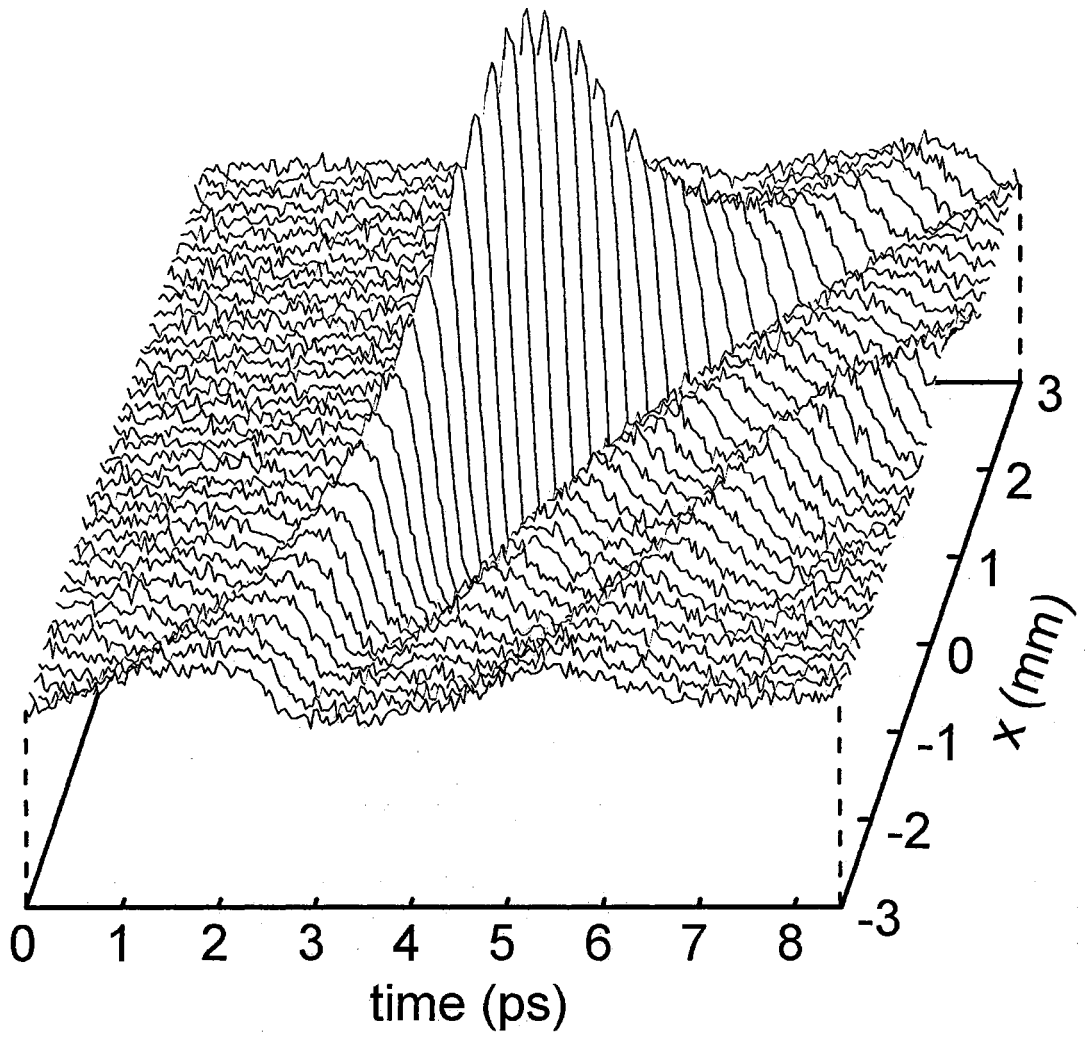


Figure 4-10. THz image of 391 μm ball. Plot is composition of curves constant in x .

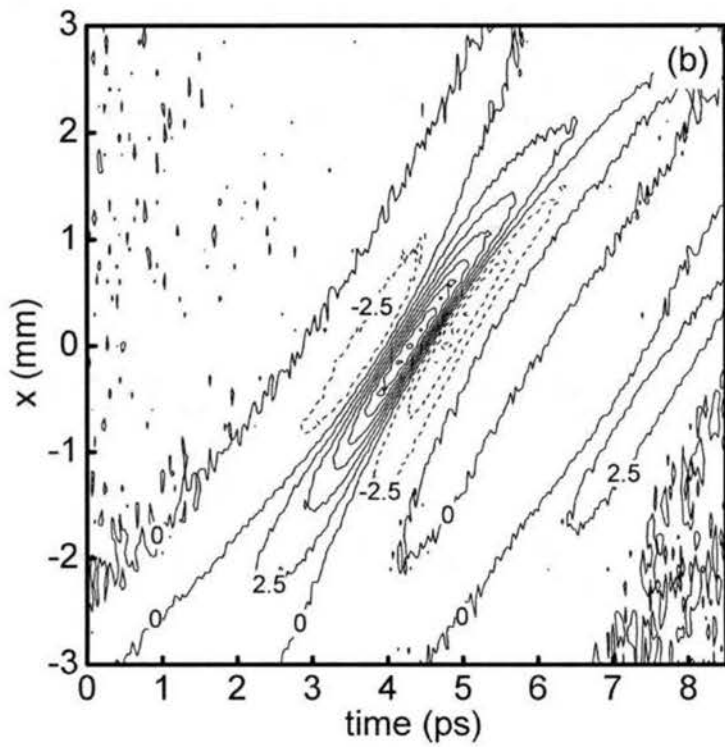
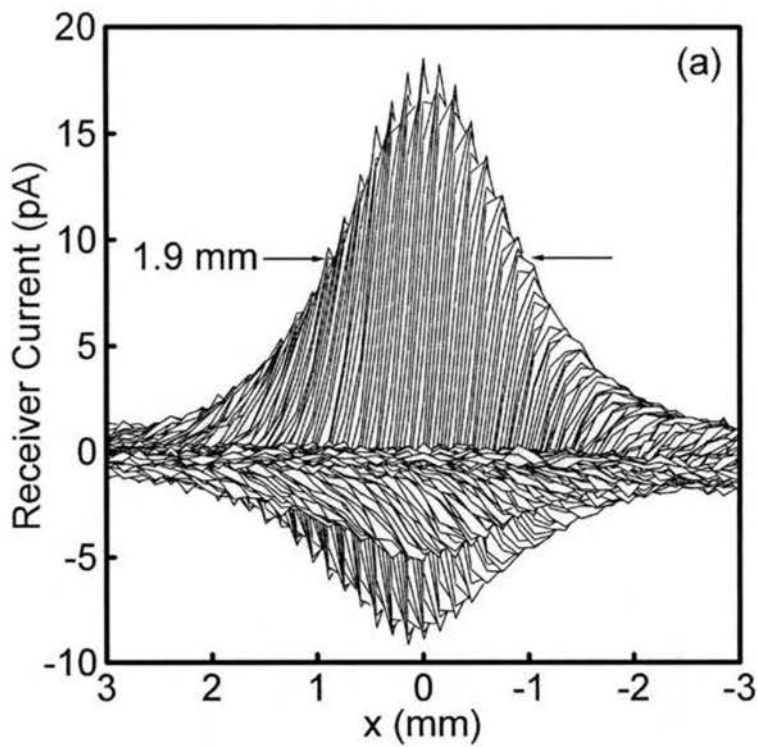


Figure 4-11. THz image of 391 μm ball. Side view (a) is a composition of curves that are constant in time. Contour plan view (b) with contour separation of 2.5 pA. Negative contours are indicated by dashed curves.

The second main difference between the images is the presence of a second pulse in the image of the 391 μm ball, labeled “2nd Pulse” in Figure 4-9. This feature occurs later in time and has a smaller amplitude than the main reflection. Given the small size of the ball, it is possible that the feature is either a weak reflection from the paraffin holder or a creeping wave which traveled around the circumference of the ball and was re-radiated back toward the spherical mirror. Such features would not be visible on the image of the larger ball since they would be too delayed in time to appear within the recorded time window. The periodic dips in the amplitude spectrum shown in Figure 4-9 are the obvious effects of the second pulse.

Using some radar theory similar to [31], one can calculate the return waveform for a plane wave pulse incident on a conducting sphere. The calculation includes both the specular reflection and the creeping wave. Using typical THz pulses, this calculation yields similar waveforms to the one seen in Figure 4-9. It is noted, however, that the calculation does not account for the fact that the ball is only half surrounded by paraffin. Preliminary calculations indicate that this fact changes the delay between the pulses. Whereas the actual data shows the 2nd pulse somewhere around 4 ps later than the initial pulse, the radar calculation predicts the pulse would exist between 3 ps and 6 ps, depending on whether the medium surrounding the ball is either air or paraffin, respectively. Moreover, pulse reshaping makes these delays difficult to measure, so the origin of this 2nd pulse remains inconclusive. Since it was not the goal of this experiment to investigate the detailed radar behavior of the system, the 2nd pulse was not further pursued. Suffice to say, such multipath effects can certainly become an issue in imaging more complicated objects. In fact, another multipath effect manifests itself in a later

experiment discussed in section 5.7. Though it is not a creeping wave, it nevertheless causes undesirable, clutter-like features in the image of two small balls.

4.2 Two Point Sources

To further demonstrate the resolution of the system two 1 mm balls were mounted together to form a double point source object. Successful imaging of this object would verify the resolvability of individual features on a more complex structure. The two balls were mounted onto a paraffin wax holder such that they were separated by about 1.4 mm in x and 1.1 mm in z , as shown in Figure 4-12.

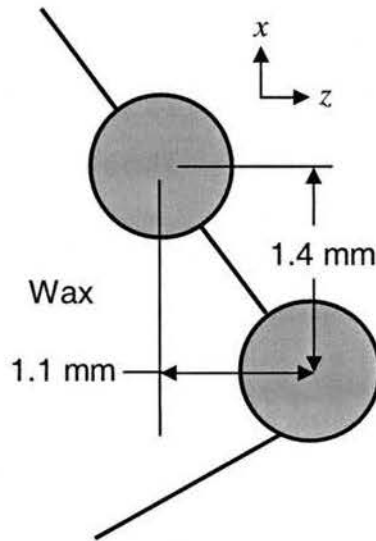


Figure 4-12. Two point source object comprised of two 1 mm balls.

The object was scanned and sampled in the x direction only, so the resulting image was one-dimensional. The image consisted of 61 spatial samples spaced by $100\ \mu\text{m}$ and covered a range from $x = 0\ \text{mm}$ to $6\ \text{mm}$. To ensure the overall object was

centered near $x = 3$ mm it was coarsely placed into position then adjusted slightly until the measured signal from the earlier reflection was maximized. This maximum signal position was then assigned the value $x = 2.4$ mm. Each spatial sample was a 17 ps, time-dependent waveform consisting of 256 data points, each separated by 66.7 fs. This is double the duration of the single point source images in order to fit both balls into the image.

Figure 4-13 shows a single temporal measurement $E(x = 2.4 \text{ mm}, t)$ from the resulting image. The arrows indicate the pulse width, 540 fs, used for calculating the range resolution of 81 μm . Figures 4-14 and 4-15 show the overall one-dimensional image. The peak SNR of the image was approximately 85. The FWHM spatial extent of each ball image is 1.8 mm, unchanged from that of the single ball image and the figures show how the two balls are easily resolvable.

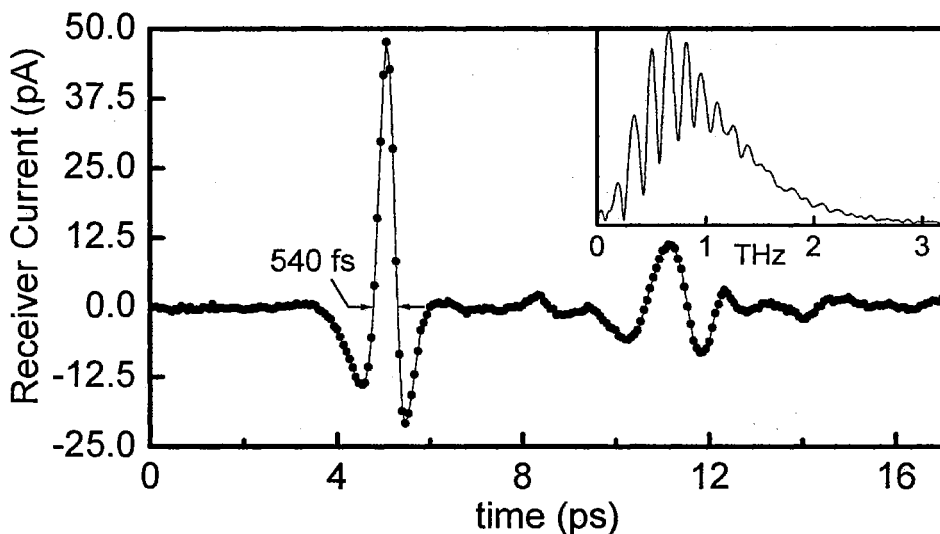


Figure 4-13. Single spatial sample ($x = 2.4$ mm) of image of two 1 mm balls. Data points are shown as filled circles with connecting lines for clarity. Normalized amplitude spectrum is shown inset.

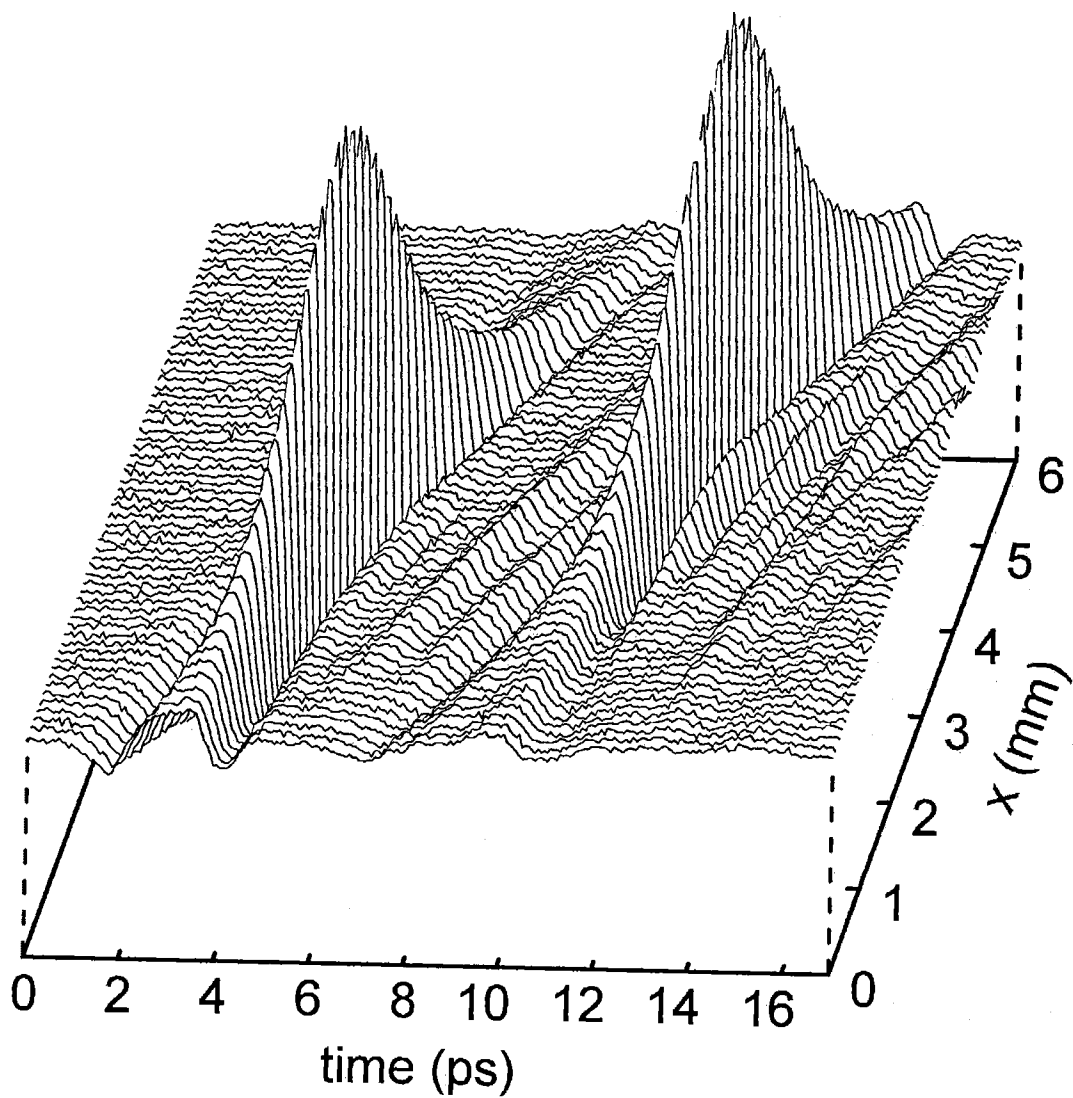


Figure 4-14. THz image of two 1 mm balls. Plot is composition of curves constant in x .

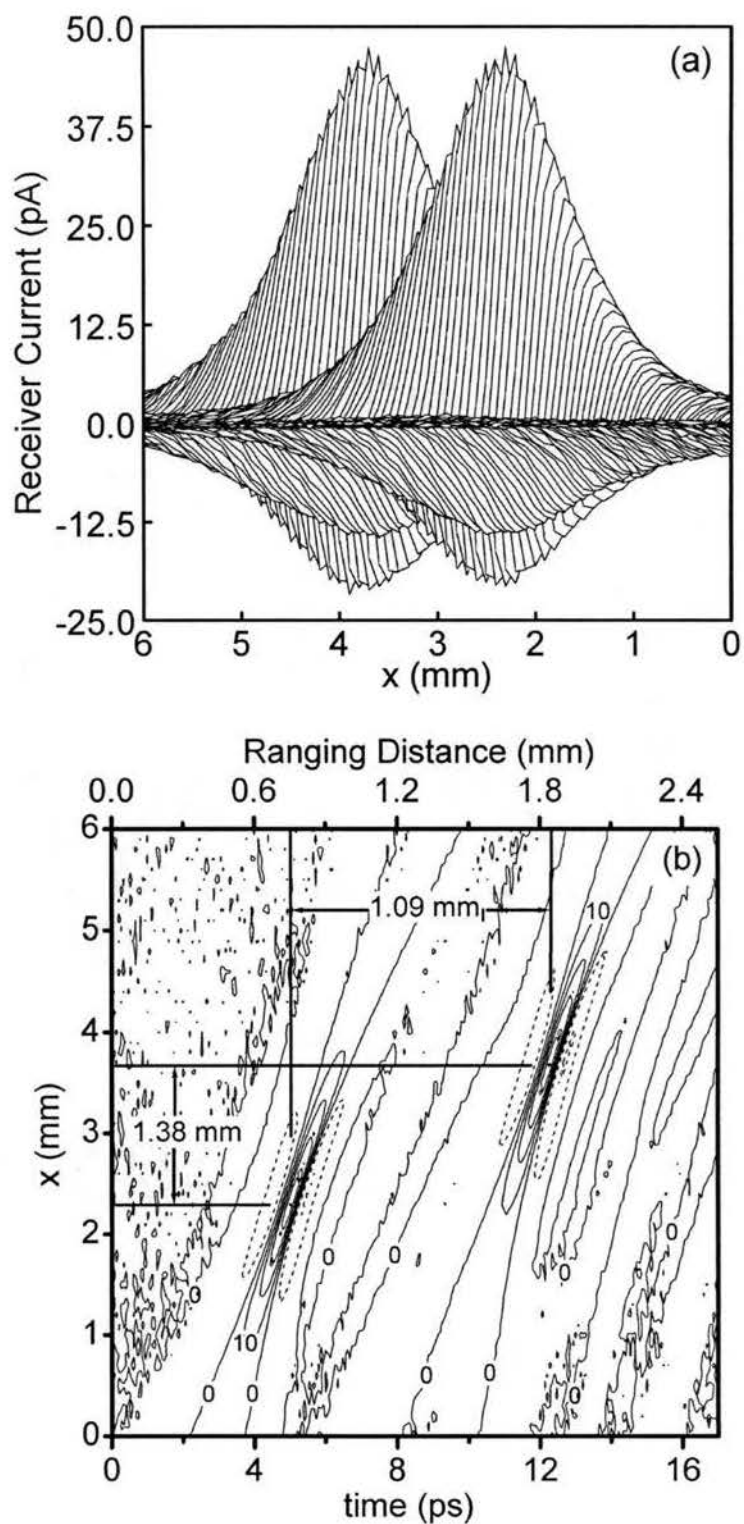


Figure 4-15. THz image of two 1 mm balls. Side view (a) is a composition of curves that are constant in time. Contour plan view (b) with contour separation of 10 pA. Negative contours are indicated by dashed curves. Dots indicate peak locations.

One interesting consequence of the high temporal resolution is that it makes it possible for two objects to be better spatially resolved. To understand this, recall the Rayleigh and Sparrow resolution criteria discussed in section 2.3. For an imaging system that measures intensity, these criteria are based on the extent to which two point source images smear together spatially. As intensity images become closer, they add together into one un-resolvable unit. For the THz imaging system, two point source images resolved in time never smear together spatially because they exist at different times. While temporally resolved, they can never smear together to form an un-resolvable unit. Therefore, the two images can become very close to one another from a transverse point of view, yet maintain their spatial resolution. This concept is easy to see in Figure 4-15a and represents a significant *spatial* resolution advantage for pulsed imaging systems. Note that this is a coherent, two-point, spatial resolution phenomenon and, even though such phenomena are understood [23, Sec. 6.5.2], they seem to be rarely applied to pulsed systems. Nevertheless, the pulsed system brings out some interesting effects wherein the definitions of resolution have to be somewhat reconsidered.

Finally, the distance measurements between the image peaks in both the x direction and the z direction are 1.38 mm and 1.09 mm respectively, thus matching the original physical measurements very closely. Also, the peak amplitude of both peaks matches to within 2% as one would expect. This experiment demonstrated the ability of the THz system to properly image extended targets.

Chapter 5

Synthetic Phased-Array Imaging

5.1 History of Aperture Synthesis

For its great ability to increase resolution in imaging systems, apertures synthesis (AS) was a monumental concept. The foundation of the idea was stellar interferometry: an idea first conceived by H. Fizeau in 1868 [34]. A.A. Michelson was the first to successfully use this technique to measure the diameter of Jupiter's satellites in 1891 [35]. With this technique, Michelson found that he could very accurately measure the diameters of distant objects by converting a normal telescope into an interferometer. He did this by placing a cap containing two parallel slits over a normal telescope aperture. The two slits formed interference fringes which could be used to infer the size of the astronomical source.

With the ability to measure phase at radio frequencies these interferometric techniques developed into the idea of aperture synthesis. In this form, AS was a method whereby the information gathering capability of a large aperture was synthesized by measurements with an interferometer of two elemental apertures, one fixed and the other movable to all positions within the large aperture [36]. Radio astronomers began using this technique to increase the resolution of their telescopes over 40 years ago [37] and continue to do so today [38,39]. Such techniques not only permitted increased resolution

but also eventually allowed scientists to steer the direction in which their telescopes looked, without physically moving antennas.

Similar systems are often termed *phased-arrays* or *adaptive arrays*, since AS is implemented by an array of transmitters and/or receivers to which variable complex weights are applied. Some of the more familiar applications are found in modern radar systems and consist of rapid electronic beam-forming and beam-steering. These applications can be used to quickly reshape side lobes and thereby reduce multipath effects, clutter, and other natural noise sources [40].

About 30 years ago Labeyrie took Michelson's work a step further by introducing the first interferometric optical telescope [41] in which light was collected and mixed from two independent optical telescopes. His work set the foundation for more complicated optical AS. Since then, optical AS for ground-based optical astronomy has greatly improved [42] and can yield images with resolution unobtainable by conventional ground-based, or even space-based, telescopes.

AS techniques have also found their way into many other forms of remote sensing and visualization. Today, AS is routinely used to generate high-resolution images at microwave frequencies. This well-known practice is termed synthetic aperture radar (SAR) and is currently the best method to obtain high-resolution, microwave images of Earth. Other forms of microwave imaging use inverse SAR principles [43,44] or deconvolution methods which have already been used to generate THz images [10,46].

Finally, ultrasonic imaging has also benefited greatly from AS. Ultrasonic AS has successfully been implemented in sonar [47] and medical imaging systems [48]. Indeed AS has become its own field of study sometimes called *Fourier Array Imaging* and has

found further application in computerized tomography (CT), magnetic resonance imaging (MRI), positron emission tomography (PET), surveillance radar and many other places [49].

However, AS it is not fit for every application. For AS to work, various phase relationships between system components must be well established. It is in this respect optical systems often suffer because most optical detectors are incoherent. Moreover, in cases where optical mixing can make AS possible, as in modern optical astronomy, very stringent component positioning is required because of the short wavelength of optical radiation.

5.2 Aperture Synthesis in THz Imaging

Due to its coherent nature and relatively long wavelengths, the THz imaging system is a prime candidate for the application of AS. Since previous experimental results showed that the THz imaging system was well-corrected and operated in the diffraction limited regime, it was decided to attempt AS to increase resolution. As explained in section 2.4 and evidenced in section 4.1.1, the resolution capability of the system is determined by two main properties: operating frequencies (bandwidth) and angular extent of the exit pupil (limiting aperture). Aperture synthesis improves the resolution by increasing the size of the exit pupil.

Since the extent of the spherical mirror defines the exit pupil, one way to increase resolution is to install a larger spherical mirror. However, this is a physically difficult solution requiring a complete redesign of the system layout. The layout would require a

less folded path in order to avoid clipping the THz beam with optical components, but a less folded path would result in greater off-axis aberrations such as astigmatism and coma. Finally, if the spherical mirror was too big, it would cease to be the most limiting aperture in the system. In this case, the silicon lens on the receiver would become the more limiting aperture. Figure 4-5 showed how this is not a problem with the original spherical mirror. All these consequences make installation of a larger spherical mirror an unattractive and, in many ways, unusable method to improve resolution. AS provides a method by which these problems can be circumvented.

5.3 Aperture Synthesis Realization

To implement AS it is necessary to add into the system another spherical mirror adjacent to the first. Such an arrangement would take the form of Figure 5-1. It shows the system with the additional spherical mirror (henceforth called the “synthetic mirror”) placed below the original and sharing the same center of curvature as the first. The reason the mirror is labeled “synthetic spherical mirror” will become clear. In this arrangement the mirrors are really only two portions of one larger spherical mirror. Together they form a sparse aperture of approximately double the original size in the y direction, but unchanged in the x direction. Each mirror is an element of a phased-array, so the total system can be regarded as a phased-array THz imaging system.

As in any imaging system, the phased-array increases the overall extent of the imaging aperture and thus improves the system’s resolution. The phased-array idea is easy to understand but considerably more difficult to physically implement. To do so

would require accurate placement of the synthetic mirror to within fractions of a THz wavelength, or approximately $15\ \mu\text{m}$, in all directions. Furthermore, such a mirror would introduce some of the same unavoidable difficulties caused by a larger single mirror. Chief among these is the fact that the larger extent of the phased-array would cause the silicon lens mounted on the receiver to become an aperture limiting component. Figure 5-2 is a scaled illustration of this situation.

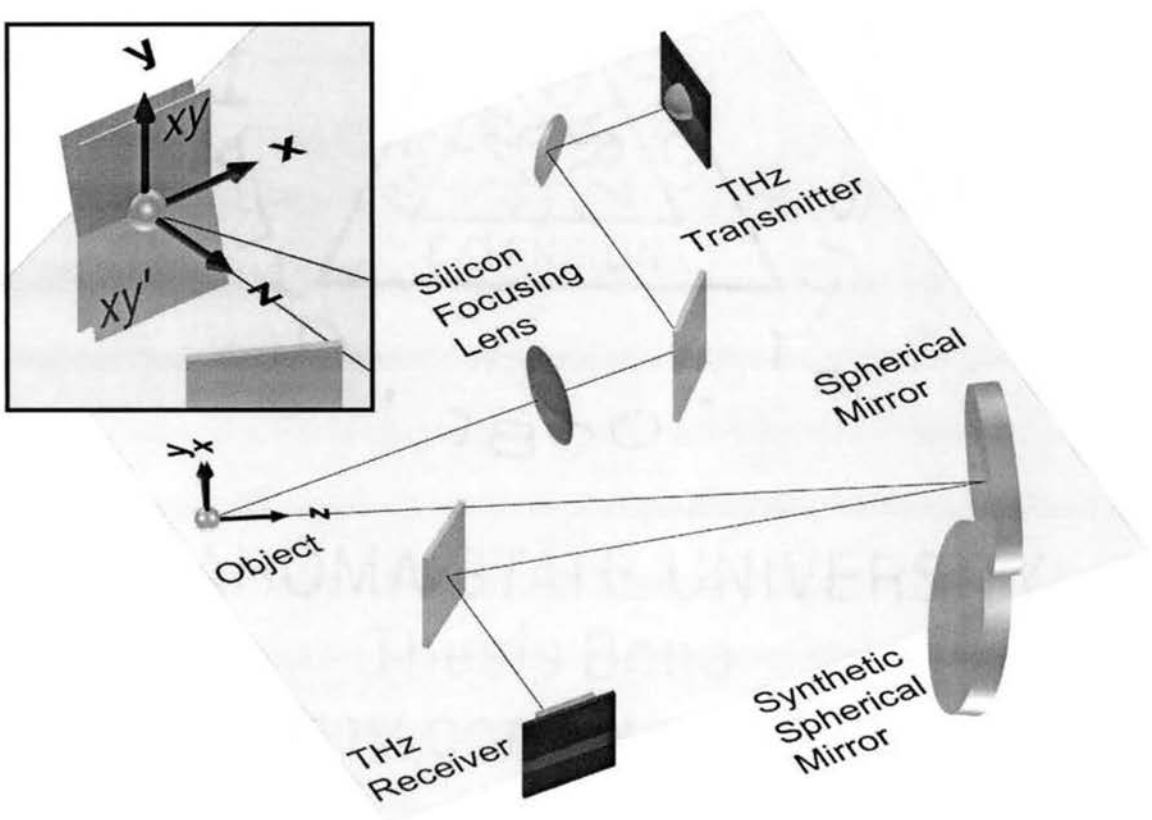


Figure 5-1. Phased-array THz imaging system with second spherical mirror located beneath the original. Both mirrors share a common center of curvature at the origin. The inset shows a detailed view of the object and two scan planes (xy and xy').

In the figure, the dotted line indicates the lower boundary of rays coming from the original mirror, or equivalently, the upper boundary of rays coming from the synthetic mirror. The solid lines indicate the boundaries for rays from the entire phased-array aperture. As the figure shows, rays coming from the lower edge of the synthetic mirror never even intersect the lens. Thus, the small diameter of the lens acts as an aperture stop limiting the extent of the entrance pupil. Such unavoidable effects make physical implementation of the phased array unusable.

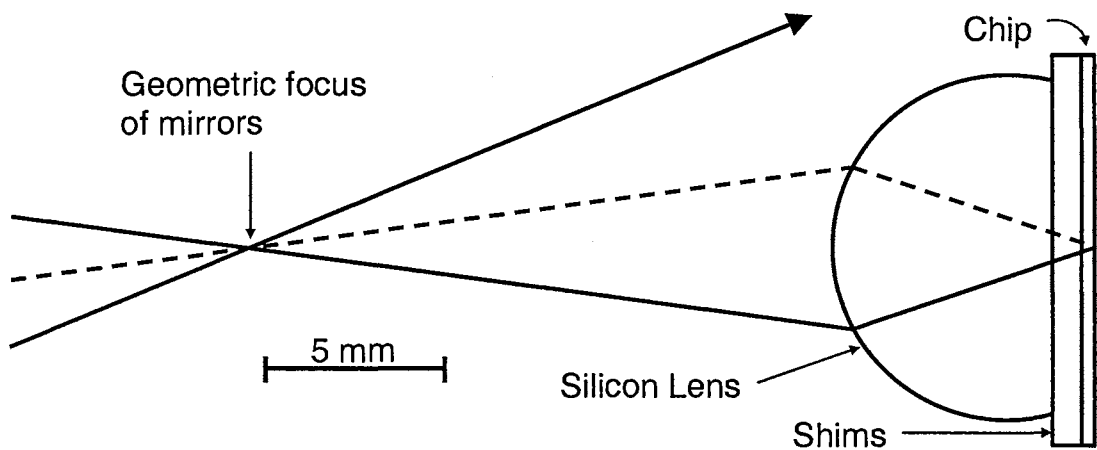


Figure 5-2. Scale diagram of THz beam for phased-array. Solid lines indicate boundary of rays propagating from both mirrors. Dashed line indicates shared boundary.

There is an alternative method by which the phased-array can be implemented and takes advantage of the fact that the object is scanned in the xy -plane such that the image can be sampled. Consider the process of image formation once again. In the normal imaging configuration, spatial samples are acquired by scanning the object in the xy -plane, which is normal to the system optical axis. Imagine if the synthetic mirror was physically implemented during this process. Figure 5-3 shows a side view of the system

operating in this manner. As the object scans in the xy -plane its relative motion appears different from the vantage of the original and synthetic spherical mirrors. From the vantage of the original mirror the scan plane appears as it normally does. From the vantage of the synthetic mirror, this same scan plane appears tilted about the x -axis by the angle defined by the angular separation of the two mirrors, in this case 14.25° . For both cases, the scan plane is the same, but the object motion appears different.

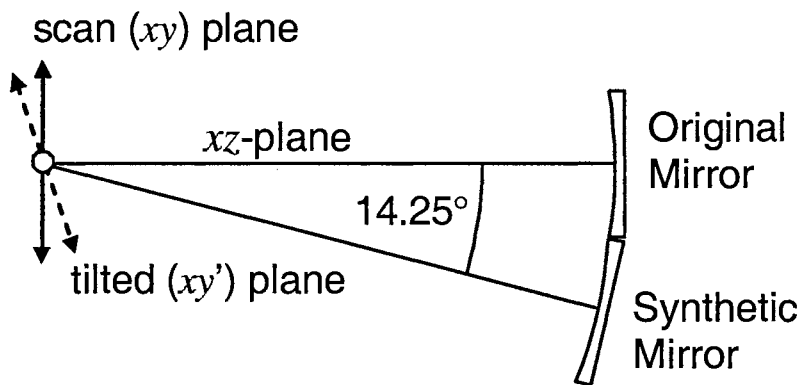


Figure 5-3. Side view of phased-array THz imaging system. Normal and tilted scan planes shown as solid and dotted lines respectively.

Consider now the case where the object is self-luminous and data are collected by the system in the configuration shown in Figure 5-3, with the exception that the original spherical mirror is removed. That is, the synthetic mirror alone is used to collect data while scanning the object in the normal (xy) scan plane. Such data would be effectively equivalent to data generated by using the original spherical mirror alone while the object scanned in the plane tilted 14.25° (denoted by the dotted line in Figure 5-3). In other words, by scanning the object in the tilted (xy') plane, the real spherical mirror is forced to see the object from the viewpoint of the synthetic mirror. In this way it is possible to

generate the data that would be collected by the synthetic mirror without ever implementing it physically. For this reason the lower spherical mirror is called the synthetic mirror. Furthermore, the continuous variability of the tilt of the scan plane makes it possible to place this synthetic mirror in any location around the actual spherical mirror, even locations in which the mirrors' extents overlap. Since this method implements a phased-array by virtue of a synthetic mirror, this method of aperture synthesis is called synthetic phased-array THz imaging.

5.4 Phased-Array Imaging

As described in section 3.2, the object is mounted on a goniometric/rotary combination stage that allows the scan plane to be tilted or rotated about the x and y axes. Figures 5-1 and 5-3 showed a scan plane tilted about the x -axis only. Tilting about the x -axis effectively places a synthetic mirror above or below the original mirror whereas tilting about the y -axis places a synthetic mirror to the left or right of the original mirror. The actual location of the synthetic mirror is determined by the angle of tilt in either or both directions.

A phased-array image is formed by multiple iterations of normal image generation. Separate images are recorded, each being generated from one individual mirror of the phased-array. Equivalently, each image is generated using a single, unique and fixed scan plane orientation. As will be discussed, all the individual images are coherent, amplitude images, with established phase relationships. Since the individual images are coherent they can be numerically superposed, creating the synthetic phased-

array image: a higher resolution THz picture of the object.

Images generated in this fashion will exhibit higher resolution only in the direction in which the overall aperture extent was widened. For example, when the scan plane is tilted about the x -axis, a synthetic mirror is created either above or below the original mirror and the effective aperture of the phased-array is then widened only in the vertical y direction. Therefore resolution will be increased in the y direction only. Similarly, if the scan plane is tilted about the y -axis, resolution will be increased in the x direction.

Synthetic phased-array imaging does not suffer from many of the problems outlined for real phased-array imaging. Whether the actual spherical mirror acts as either a normal imaging mirror or as a synthetic mirror, the system behaves just as it would in the normal imaging configuration. The only thing used to create the phased-array is the simple alteration of the scan plane of the object. The remainder of the system is unchanged.

5.5 Synthetic Array Details

The equivalence between using the synthetic mirror created with a tilted scan plane and using the normal scan plane with an additional real mirror actually installed in the system requires more discussion. For the benefit of this discussion, each case is given a different name. The case in which two real mirrors are implemented in the system and the object is scanned in the normal xy -plane is termed the real case, because this is the configuration of the system if a real phased-array was actually built. The case in which the original

spherical mirror is used with the tilted scan plane to implement a synthetic mirror is termed the synthetic case. Even though the end effect of synthetic phased-arraying is effectively equivalent to actual phased-array imaging, the mechanisms in each case are somewhat different. These mechanisms will now be discussed for both the vertical and horizontal arraying case.

5.5.1 Vertical Arraying

In the real case, the image plane (or reception plane) is coincident with the (xy) scan plane, as shown in Figure 5-4. This is simply due to the orientation of the receiver, whose axis is always considered normal to the image plane. It is clear that the rays (and the phase fronts) coming from the real lower mirror intersect the image plane at some angle. Using spatial frequency concepts, we see that this angle introduces high spatial frequency components into the image. These components interfere with those in the image from the original mirror to yield a higher resolution composite image.

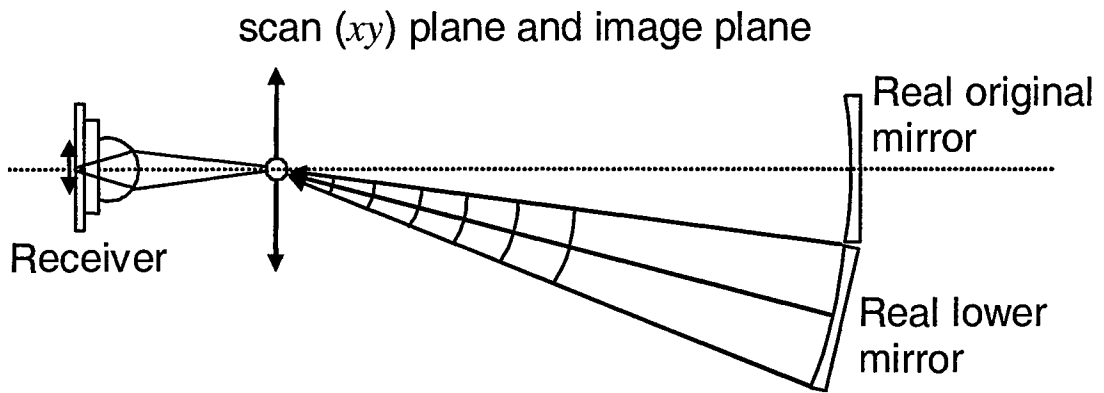


Figure 5-4. Relationship between spherical mirrors, scan plane, and image plane in a real array.

In the time domain, the angle between the image plane and the phase fronts is manifest as a slight shifting in time of the pulse. Consider Figure 5-5a, which shows the phase fronts of a wave issuing from some section of the lower mirror. If the receiver is sampling at point A, there will be a delay of δt_A in the phase front compared to when the receiver samples point B. Similarly, if the receiver samples at point C, there will be an advance of δt_C in the phase front, compared to point B. Figure 5-5b shows how these delays are not the same when the wave is issuing from the original spherical mirror. When the two phase fronts from each mirror are added together it is this decoherence in phase at the outer portions of the image that causes the interference which consequently sharpens the image. Therefore, the enhancement of resolution that accompanies the addition of the real, lower spherical mirror is directly due to the fact that the image plane is angled with respect to incoming phase fronts from the lower mirror.

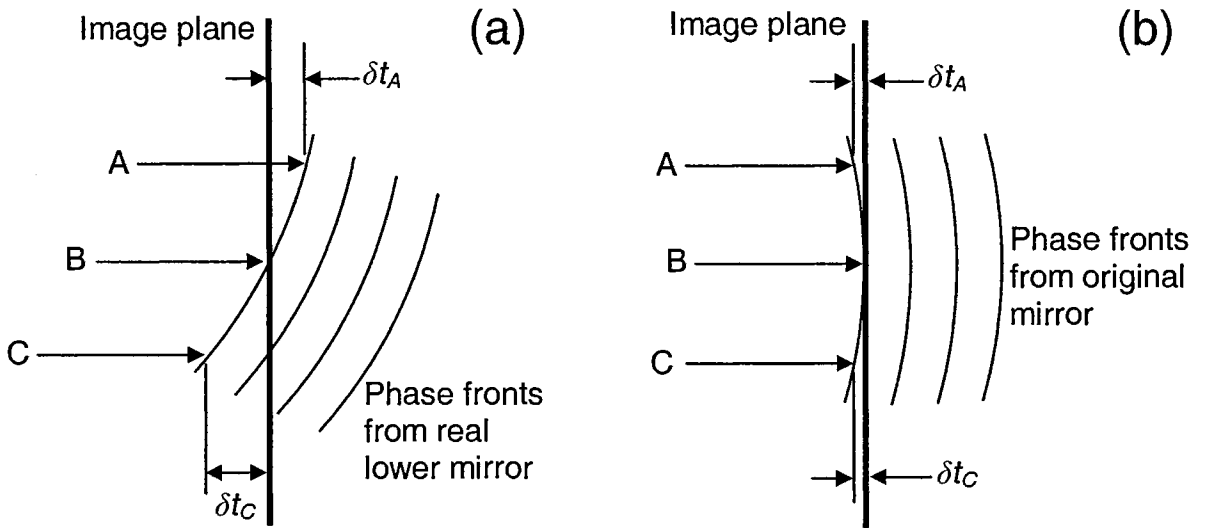


Figure 5-5. Relationships between image plane and phase fronts from (a) real lower mirror, (b) original mirror.

The resolution increase accompanying the synthetic case is due to a different, yet similar, mechanism. In order to strictly mimic the exact behavior of a real lower mirror by means of the original mirror, it would be necessary to rotate the object, scan plane, and image plane, such that the original spherical mirror sees everything as the lower mirror would if it were implemented. Such a setup is illustrated in Figure 5-6a, where, along with the other components, the receiver and image plane have been rotated. However, when synthetic phased-array imaging is performed in the THz system, the receiver (and image plane) is not actually re-oriented. Such a re-orientation of the receiver is not possible for several reasons including the fact that it would drastically affect laser alignment and destroy the absolute timing reference in the system. Instead, only the scan plane is rotated, or tilted, as shown in Figure 5-6b.

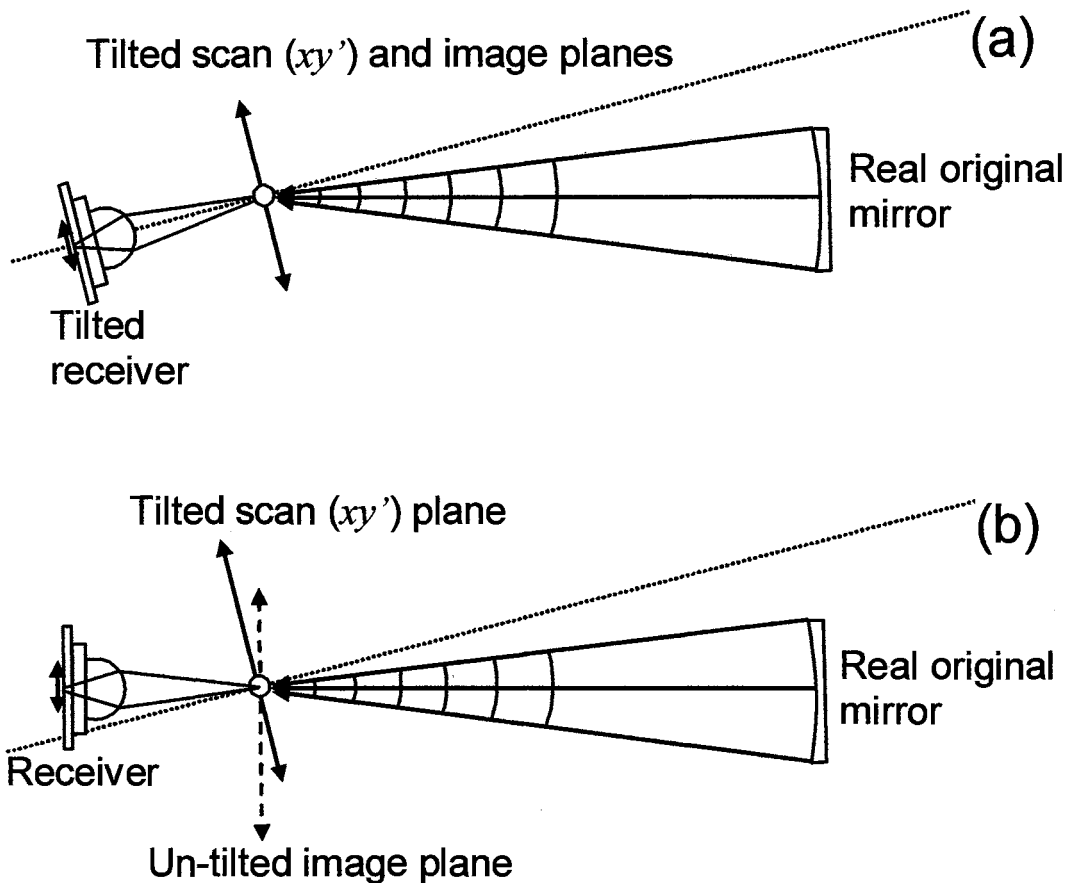


Figure 5-6. Relationship of scan plane, image plane and real mirror for synthetic arraying. (a) strict equivalence between synthetic mirror and lower mirror achieved by rotating image plane and receiver, (b) actual arrangement in synthetic phased-array THz imaging system, image plane not rotated.

It is obvious then, that the synthetic case is not strictly equivalent to the real case. The original mirror (acting as a synthetic mirror) and the phase fronts issuing from it are no longer angled with respect to the image plane, as they were in the real case. Therefore, the mechanism by which resolution is enhanced must be different. The phase shifts necessary to enhance the resolution in this synthetic case come from the fact that the scan plane acquires an angled relationship with the image plane. Figure 5-7a helps to illustrate this in terms of phase fronts. As the object moves in the tilted scan plane the phase fronts from the original mirror also acquire a tilt. The tilted phase fronts manifest themselves as

timing delays or advances. Therefore, the final relationship between the phase fronts and the receiver plane in the synthetic case, shown in Figure 5-7a is equivalent to that of the real case, shown in Figure 5-7a.

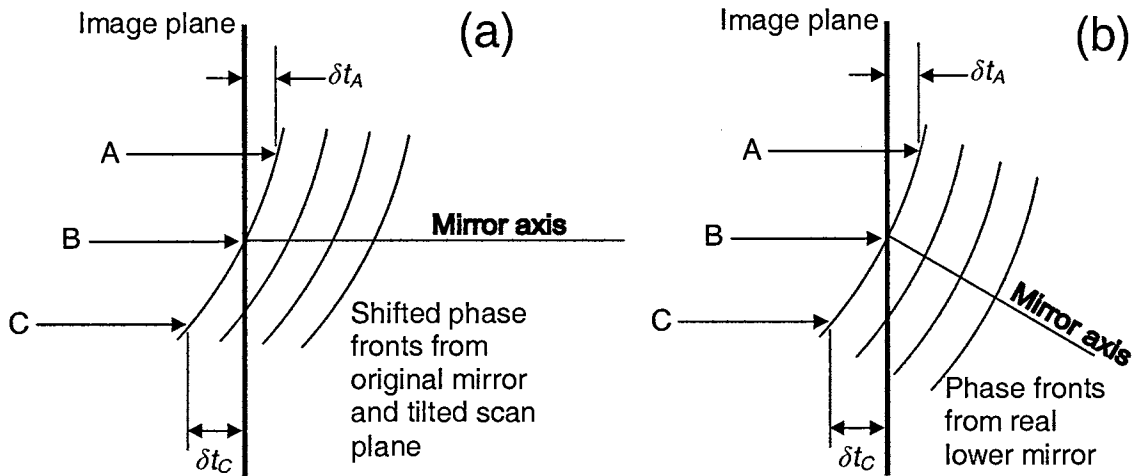


Figure 5-7. Comparison of relationship between phase fronts and image plane for (a) synthetic array case, (b) real array case.

To summarize these concepts, the final result of synthetic arraying is the same as that of real arraying, even though the two are not strictly equivalent in terms of their mechanisms. In the real case, the mechanism by which two images interfere to form a higher-resolution image is the angled orientation between the image plane and the phase fronts issuing from the mirrors. The scan plane and image plane are coincident; therefore their relationship introduces no further phase effects. In the synthetic case, the scan plane and image plane are no longer coincident; therefore their angled relationship introduces the phase effects by which another mirror is synthetically modeled. However, the image plane is no longer angled with respect to the mirror axis or the phase fronts issuing from it; so no phase effects arise from this relationship. This tradeoff in mechanisms permits

successful synthetic phased-array imaging in the THz system, while removing the need for repositioning the receiver. In the end, both the real and synthetic cases can be considered equivalent for THz imaging purposes.

5.5.2 Horizontal Arraying

Horizontal arraying is equivalent to vertical arraying in that synthetic arraying is only *effectively* equivalent to real arraying, due to the fact that the image plane is not re-oriented. All the accompanying discussions regarding the mechanisms by which resolution is increased in vertical arraying are equally applicable to horizontal arraying. However, there is one additional effect present in horizontal arraying due to the off-axis nature of the system. Figure 5-8a shows a top view of the system with a phased-array mirror located to the right (+x direction) of the original mirror. Both mirrors share a common center of curvature and therefore, together, they behave as a single sparse aperture mirror. However, making the original mirror see the object from the vantage of the phased-array mirror cannot be strictly done by rotating the scan plane about the y-axis. Instead, the object and scan plane must be rotated about a vertical axis which goes through the center of curvature of the mirrors, marked by a star in the figure. As discussed in the previous section, the image plane (or receiver) is not concurrently moved in the process. Therefore, tilts about the center of curvature cause very large shifts in the arrival time of the image to the receiver. Consequently, the two images, one formed by the original mirror the normal configuration and one formed from the original mirror synthetically acting as the phased-array mirror, do not overlap in time and cannot

interfere properly to enhance the resolution of the composite image.

The remedy to this problem is simply rotating the scan plane about the y -axis. This causes an effective translation of the scan plane such that the images are once again aligned in space and time. Rotation about the y -axis is effectively equivalent to rotation about the center of curvature of the mirror plus a translation of the object and scan plane. This translation allows both images, produced by the real mirror in the normal and synthetic configurations, to overlap in time and interfere properly to increase the resolution of the composite image. The only additional effect of this translation is a slight change in magnification between the object and image. Since the off-axis angle of the system is so small (10° full angle) this magnification is not significant. Therefore, it is apparent that synthetic phased-array imaging need not be altogether equivalent to a real arraying. Nevertheless, the method is still quite effective as will be shown.

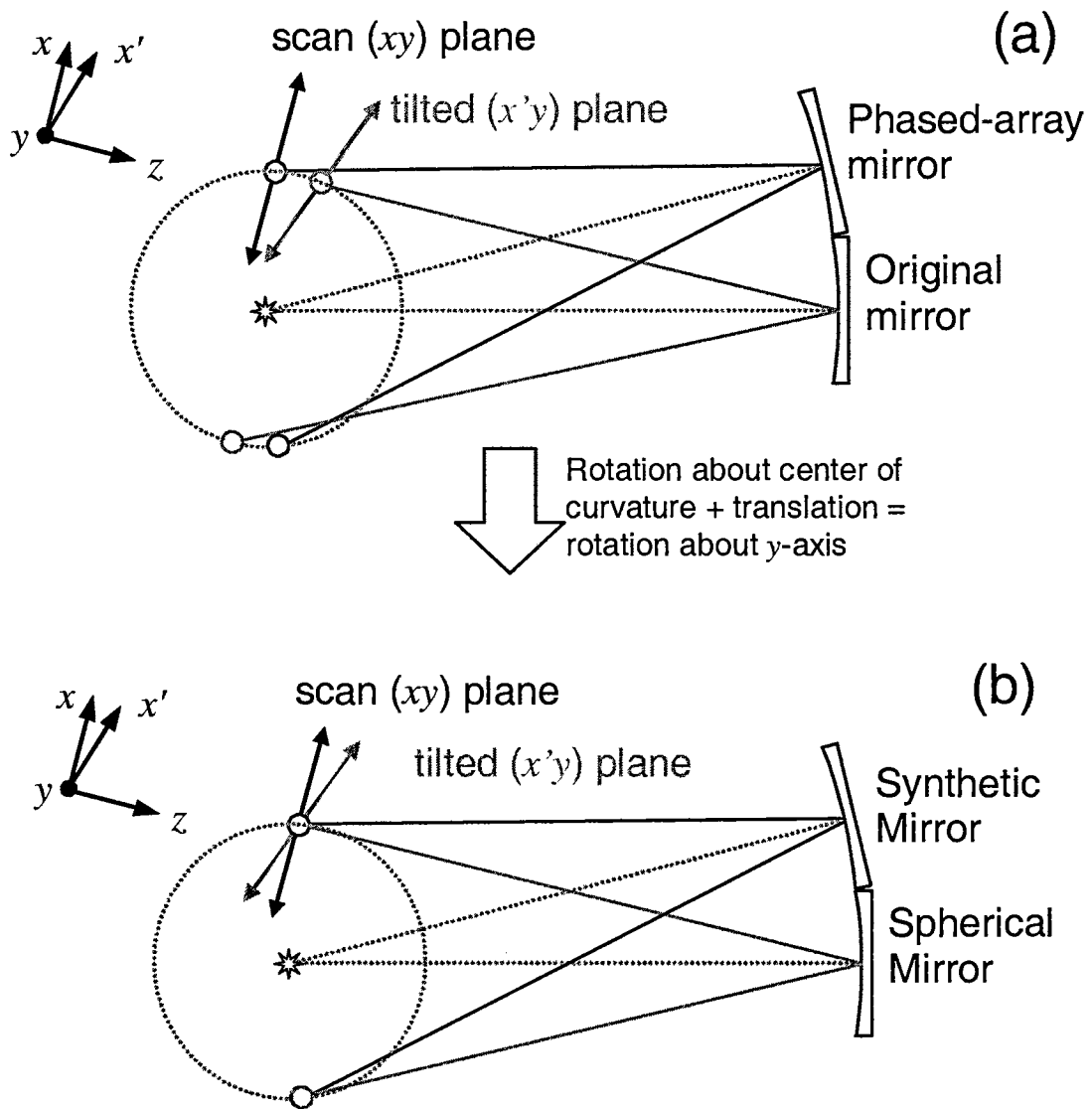


Figure 5-8. Horizontal arraying details. (a) scan plane must be rotated about center of curvature to allow original mirror to mimic phased-array mirror, (b) rotating about y-axis creates an effective translation of the object and image.

5.5.3 Image Coherence

The necessary coherence of the images is due to two properties of the THz imaging system. First, all the individual images are generated by the same single object. All the phased-array mirrors see the same object emitting the same wave-field, regardless of their orientation. This provides the spatial coherence between multiple mirrors, and consequently, between multiple images. Second, the object is illuminated by a pulsed THz beam that is measured coherently [16]. This provides the temporal coherence between images ensuring that they all remain locked in a constant phase relationship. The fact that the THz is pulsed makes it easy to measure this phase relationship, which is simply manifest as the temporal location of the pulse. The following section discusses more details of this phase relationship.

Coherence among the spatial samples in any single image is established by the precision of the motorized delay line, which is about 500 nm. This translates into 3.33 fs of temporal precision, far better than required to maintain phase coherence among samples.

5.5.4 Phase Reference

For phased-array imaging to be successful, each individual, coherent image must have an established phase relationship with the others. Since the THz imaging system uses short pulses for illumination, this phase relationship is easy to establish, for a point source. As will be shown in section 5.7.2, it can be more difficult to establish for more complicated objects. Phase reference establishment relies on the fact that each individual

image has its own associated scan plane containing unique points through which the object scans; yet all the scan planes share one common point, the origin. When the object is at this point, all the individual images should exhibit zero relative phase with respect to each other. Given the pulsed nature of the THz, the relative phase between images is manifest as simple timing shifts of the pulse. Therefore, zero relative phase can be established easily by ensuring that the waveforms (spatial samples) collected from each image at the origin overlap exactly. A close overlap indicates that the object was in the same spatial location (the origin) for each image. Figure 5-9 shows two such waveforms from a phased-array image. Both are spatial samples (at the origin) of the image of a point source. The solid line indicates the origin sample from the first image generated with the scan plane in the normal orientation. The dashed line indicates the origin sample from the second image generated with the scan plane oriented -16° about the x -axis. Their close overlap ensures the object was in the same spatial location during each origin sample.

Phased-array imaging, therefore, is accomplished by the following procedure. A single image is recorded with the scan plane in some desired orientation. The resulting data contains the spatial sample collected when the object was at the origin. Following image recording, the scan plane is re-oriented to begin recording the image from a synthetic mirror. Before recording another image, the object is carefully positioned such that the spatial sample at the origin overlaps closely with the previous one already recorded. The careful positioning ensures that the origin is in the same place it was in the previous image, thereby establishing the phase relationship.

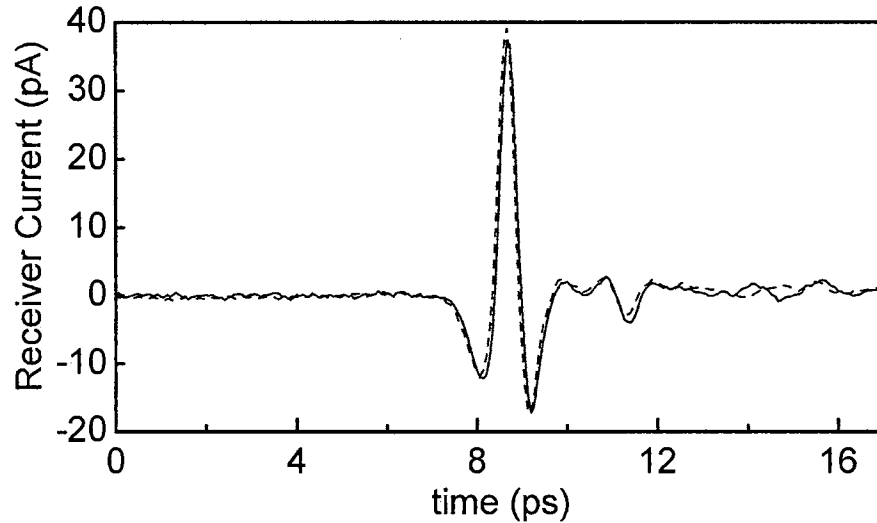


Figure 5-9. Phase locked reference waveforms for two arrayed THz images.

Imaging then continues as normal. This process is repeated for every subsequent image. The overall result is that all the images are phase-locked to each other with a common absolute reference.

5.5.5 Object Placement Accuracy

To experimentally realize the phase locking procedure, it is necessary to have very accurate placement of the object before and during imaging. Transverse placement is done by aligning the object to the crosshairs of a long-distance microscope mounted on a fixed kinematic base. The microscope looks at the object along the system optical axis (in the $-z$ direction) so the crosshairs register the object's x and y position. This results in a transverse placement accuracy of approximately $15\ \mu\text{m}$; more than sufficient as shown by the following spatial frequency calculation. If φ is the full-angular extent of the mirror subtended at the axial image point, then the highest angular spatial frequency possible in

the image is $k_y = 2\pi \sin(\varphi)/\lambda = 12.89 \text{ mm}^{-1}$, where $\varphi = 14.25^\circ$ and λ is $120 \text{ }\mu\text{m}$ corresponding to 2.5 THz . Using this value, the shortest spatial wavelength generated by the system in the normal configuration is $\lambda_y = 2\pi/k_y = 488 \text{ }\mu\text{m}$; over 30 times larger than the transverse placement accuracy.

Object placement is more critical in the z -dimension where even slight variations can create significant phase shifts. Coarse z -placement is accurate to about $100 \text{ }\mu\text{m}$ and is done by adjusting the object position until it is well focused when viewed through the microscope. Fine adjustment in z is done by measuring the temporal location of the amplitude peak in a spatial sample. The object position is adjusted until the peak is in the same location as the peak of the reference. Thus, using the ranging capabilities of the system, z -positioning can be accurate to approximately $15 \text{ }\mu\text{m}$, or $1/10^{\text{th}}$ a wavelength for 2.0 THz .

It is noted that there is considerable tolerance in positioning the object despite the fact that the phase must be very accurate. Positioning in x and y by use of the microscope is far better than it need be. Placement within about $\pm 50 \text{ }\mu\text{m}$ would be sufficient since it is still only about $1/10^{\text{th}}$ of the wavelength of the highest spatial frequencies involved. Positioning in z also has some tolerance but in another form. As long as the object is placed within approximately $100 \text{ }\mu\text{m}$, the time-delay between the gating optical pulses of the transmitter and receiver can be manually adjusted to bring the peak of the pulse into overlap with the reference. This seems somewhat invalid since it doesn't actually put the object exactly on the previously defined origin. However, these small adjustments to lock in the phase do not noticeably affect the image. This is due to the shape of the focal region of the spherical mirror. As will be discussed in chapter 6, this shape can be

described as an elongated tube and permits a significant tolerance in positioning the image plane. In other words, small changes in the z -position of either the object or the image plane do not noticeably affect the spatial field distribution in the image plane, as long as the timing is established.

5.5.6 Image Reconstruction

As stated earlier, the phased-array elements effectively share a common center of curvature in the THz system. Since the elements are spherical mirrors this allows them to behave together as a large, single, sparse-aperture spherical mirror. Therefore they naturally act in unison as one object: one large-aperture optic, forming a single image. The data collected by this system need not be deconvolved or further processed in any way to form the image. There is no need for interferometric techniques like those used in radio astronomy. The image is completely processed naturally by the setup of the system. Aside from superposing the individual images, the phased-array system behaves just like the single mirror system.

This is quite different from other AS systems. In many AS systems, such as those used in radio astronomy, it is impractical or impossible to place individual array elements such that they construct a single coherent sparse-aperture optic. Rather, individual movable elements are used to collect data, which is then reconstructed into an image by interferometric techniques [36]. Similarly, airborne SAR methods collect data from a single array element that is scanned through the sky on an airplane. The data, known as the phase history [50], is recorded and images are later reconstructed with numerical or

optical techniques.

Most optical systems, however, form images immediately by lenses. The relative phase shifts applied to the spatial signals are induced by the shape and curvature of the lens itself. The THz system is able to use such optical processing to naturally form an image, just like a lens. At the same time, AS can be easily implemented in the THz system due to its relatively forgiving positioning requirements and its ability to measure amplitude and phase.

In all these respects the THz imaging system is unique and demonstrates the simplest possible form of image reconstruction in an AS setup: superposition. This mixture of optical and microwave properties makes high resolution imaging at THz frequencies very simple yet effective.

5.6 Single Point Source

A 1 mm diameter, chrome-plated, steel ball was used as the object to demonstrate the conceptual validity of synthetic phased-array THz imaging. Again, this ball behaves as a point source so it was possible to obtain an image smaller than the 1 mm ball. Two images were recorded, each having a different orientation of the scan plane. The first image was recorded with the scan plane in the normal orientation, or 0° tilt. This scan plane was called the xy -plane. The second image was recorded with the scan plane tilted -16° about the x -axis to mimic a synthetic mirror located below the spherical mirror. This scan plane was called the xy' -plane. Spatial samples were taken in both the x and y dimensions so the resulting data set had the form $E(x,y,t)$. To differentiate the two data

sets and the two different scan plane orientations the first image was termed $E_1(x,y,t)$ and the second, $E_2(x,y',t)$. In both images a total of 825 spatial samples were recorded; 33 samples in y (or y') by 25 samples in x . Spatial sample spacing was $125\ \mu\text{m}$ in both directions, so the images spanned a total of 3 mm in x and 4 mm in y . Each spatial sample was a 17 ps, time-dependent waveform that consisted of 256 data points, each spaced by 66.7 fs. The peak SNR of the images ranged from about 70 and 110 due to a recurring noise problem. In section 5.5.4, Figure 5-9 showed two spatial samples obtained from this experiment. These were the origin samples of the two individual images and their overlap ensured a proper phase reference. After both individual images were collected they were superposed to generate the higher-resolution composite image.

5.6.1 Three-Dimensional Data Display

Having collected three-dimensional data, the problem of displaying it became evident. Surface plots are sufficient for two-dimensional data wherein the third display dimension can be used to indicate field amplitude. However, such plots are no longer usable for three-dimensional data because a fourth display dimension is necessary to indicate field amplitude. There are several ways to overcome this problem. One such method borrows from C-scan ultrasonic imaging wherein the peak amplitude value is picked from each spatial sample and this value is used as a gray level in the image [33]. Another method is to simply plot the amplitude values in a single plane of interest within the image. Such a plane would represent a slice through the volumetric data and could correspond to some specific temporal or spatial region of interest.

Another method is to integrate out the time dimension by plotting the energy density of the images, $G(x,y)$, rather than their field amplitudes, where

$$G(x, y) = \frac{1}{\eta_0} \int (E_1 + E_2)^2 dt = \frac{1}{\eta_0} \int (E_1^2 + E_2^2 + 2E_1E_2) dt \quad (5-1)$$

and η_0 is the impedance of free space equal to 376.73 ohms. Here E_1 and E_2 represent the two sets of individual electric field image data and (E_1+E_2) represents their superposition. Therefore $G(x,y)$ is the composite energy density image and contains both the individual energy density images $G_1(x,y)$ and $G_2(x,y)$ defined as

$$G_1(x, y) \equiv \frac{1}{\eta_0} \int E_1^2 dt \quad (5-2)$$

$$G_2(x, y) \equiv \frac{1}{\eta_0} \int E_2^2 dt \quad (5-3)$$

and the interference term defined as

$$G_{12}(x, y) \equiv \frac{1}{\eta_0} \int 2E_1E_2 dt . \quad (5-4)$$

The net result is a two-dimensional image that would be obtained if THz photographic film or a THz CCD camera was placed in the image plane and used to record the image. This approach can be generalized to superpositions of greater numbers of individual images by the following formula

$$G(x, y) = \frac{1}{\eta_0} \int (E_1 + E_2 + E_3 + \dots + E_n)^2 dt . \quad (5-5)$$

The individual energy density images are then designated by

$$G_n(x, y) \equiv \frac{1}{\eta_0} \int E_n^2 dt . \quad (5-6)$$

Henceforth, the “density” term shall be suppressed in referring to such images. For simplicity they shall simply be referred to as energy images.

5.6.2 Phased-Array Images

The images obtained by this experiment are shown in Figure 5-10 and will now be discussed. Consider the plane (henceforth called the xY plane) bisecting the two scan planes, xy and xy' . To a good transverse approximation $y = Y$ and $y' = Y$. For plotting purposes only, therefore, we may treat all these variables as same single variable Y . By doing so, the transverse spatial profile of the images can be presented in a comparable fashion. Figure 5-10 uses this Y variable for the vertical axis of all the images. Figures 5-10a through 5-10c show the normalized energy plots for the individual images (at 0° and -16° orientations), and the composite image, respectively. Figures 5-10d through 5-10f show the corresponding amplitude images. Figures 5-10d and 5-10e were generated by picking the peak field amplitude out of each time-dependent spatial sample. This amplitude was used to determine the contour level at that spatial location.

The composite amplitude image, shown in Figure 5-10f, had to be generated in another fashion. It is not meaningful to simply pick the peak amplitude value in the composite image because there are two peaks (one from each individual image) for every spatial point except those near the origin. To clarify this Figure 5-11 shows the $x = 0$ slice through the normalized composite image data. The individual image pulses are

maximally separated in time at the far y -ends of the image. These two pulses smoothly pass through each other as a function of y and overlap precisely at the $(x = 0, y = 0)$ position. Therefore, to display the image, it was necessary to pick the amplitude values in a particular plane of interest. For Figure 5-10f, this plane was defined by the set of temporal points which lie halfway between the individual image peaks. Figure 5-11 shows this plane as the heavy line.

There are two reasons why this plane was a suitable choice. First, this plane defines the set of all points in which the coherent interference between the two images is maximized. This is consistent with the goal of this experiment, which was to utilize the beneficial effect of interference. It is pointless to look at some region in time where no significant interference is happening. Second, this plane corresponds to the composite image plane of the phased-array system. Consider Figure 5-12 where the side view of the phased-array system is shown again. Each mirror can be assigned its own individual image plane in a geometric optics sense. In this sense, the image plane is the plane perpendicular to the axis of the optical path and located at the geometric image point. As shown in Figure 5-12, the image planes are shown as solid lines, Γ_O and Γ_S , for the original and synthetic mirrors, respectively. Neither of these image planes, however, would be suitable to call the image plane of the composite phased-array system. Instead, this composite image plane should be the plane perpendicular to the composite system optical axis, shown as the dash-dot line in Figure 5-12.

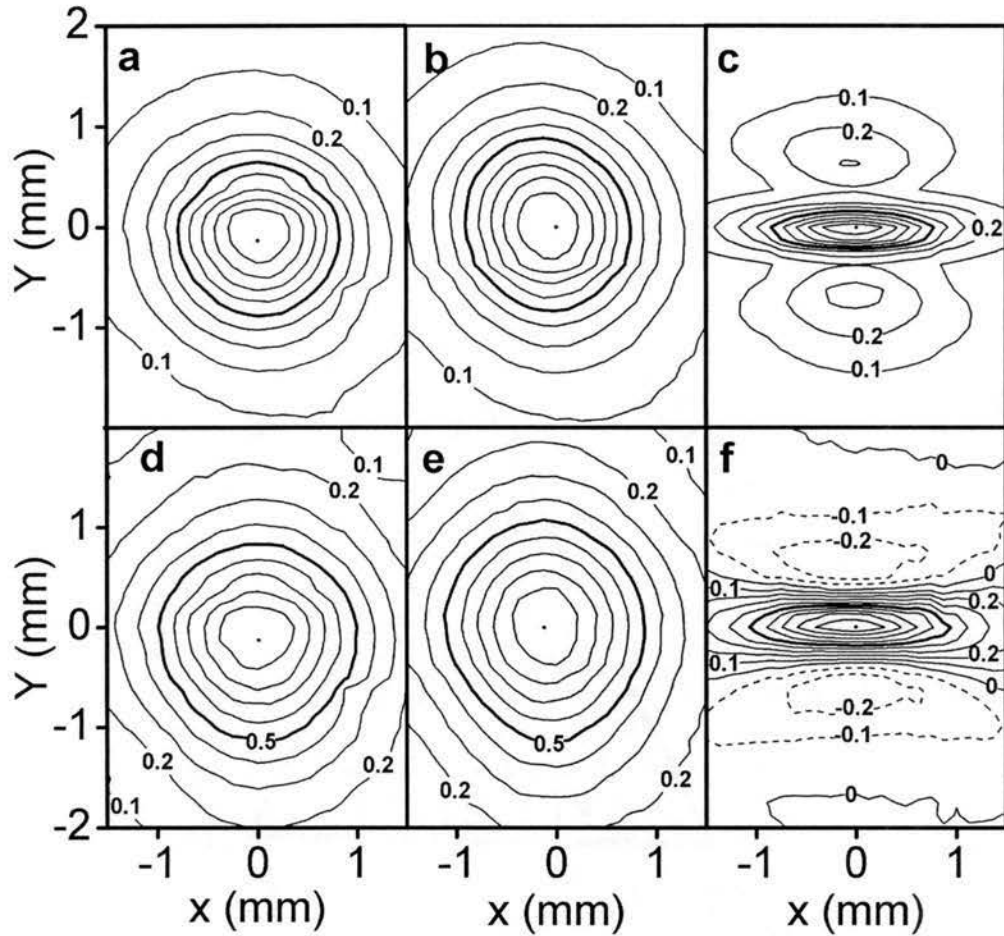


Figure 5-10. Normalized transverse array images of THz point source. (a) 0° energy image (b) -16° energy image, (c) phased-array energy image, (d) 0° amplitude image, (e) -16° amplitude image, (f) phased-array amplitude image. Contours separated by 0.1. Negative contours are denoted by dashed curves. Contour for 0.5 shown as heavy curve.

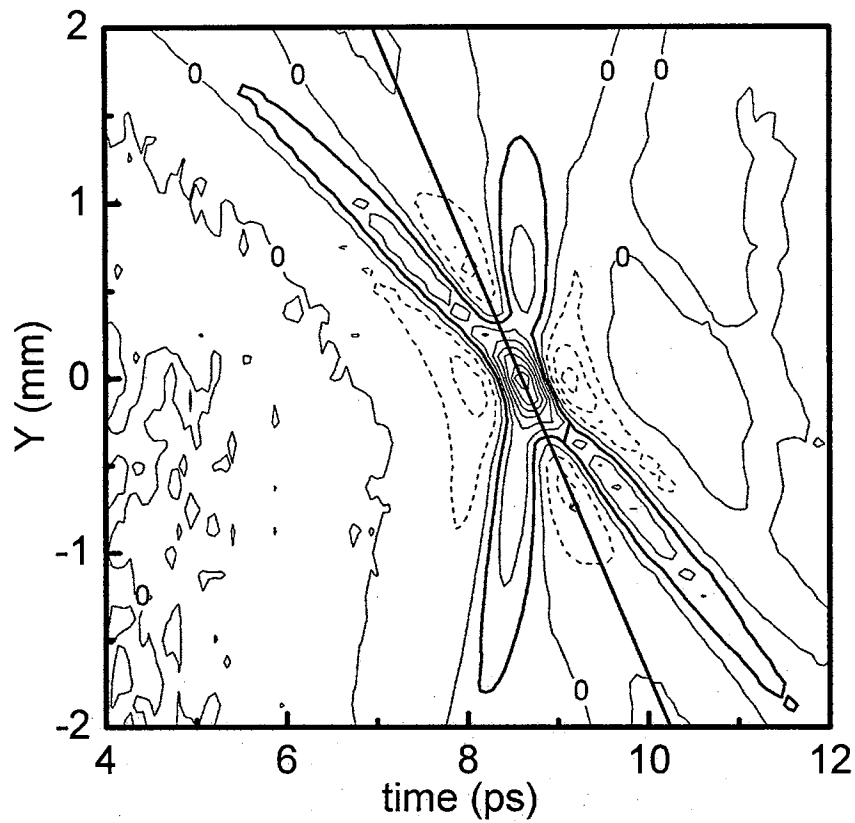


Figure 5-11. Slice $x = 0$ through normalized composite image data. Contours separated by 0.125. Negative contours denoted by dashed curves. Contour at 0.125 shown as heavy curve to outline pulse peaks.

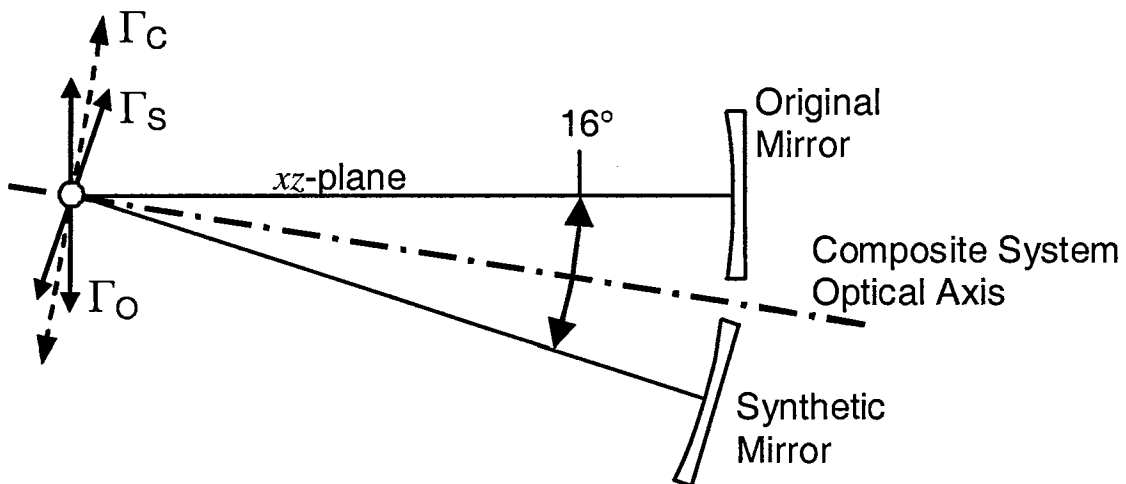


Figure 5-12. Side view of phased-array system showing individual and composite image planes.

This new image plane Γ_C corresponds to the xY plane previously mentioned and is shown as the dashed line in Figure 5-12. Since the receiver was not moved during image collection only the Γ_O plane corresponds to the actual reception plane of the system, as described in section 5.5. The composite image plane, Γ_C , is merely a conceptual tool for extracting the data in a desirable fashion.

To link the physical position of the composite image plane with timing, we note that the temporal separation between the pulses in the composite image is a function of y , and the rate of change of that separation is dependent on the angle between the individual image planes. The composite image plane bisects this angle and, therefore, the time slice corresponding to the image plane of the composite system, Γ_C , is halfway between the pulse peaks of the individual images.

The effects of the phased-array system are obvious in Figures 5-10c and 5-10f. In the vertical y dimension, the width of the image is significantly reduced and two side lobes appear, whereas no significant change is apparent in the horizontal x dimension. This is because the synthetic mirror increased the effective aperture in the vertical direction only. The vertical side lobes appear as a consequence of the sparse composite aperture. The decrease in vertical width of the image (or equivalently the increase in resolution) is approximately four times.

5.6.3 Artificial Aperture Doubling

The four times increase in resolution was unexpected and is a consequence of the fact that the object is not self-luminous but moves through a fixed illumination beam. In the xy -plane, the arrival time of the illumination pulse to the object is approximately independent of the object's y -position. However, in the xy' -plane, the illumination encounters more or less path length as the object scans in the $+y'$ and $-y'$ directions, respectively. Figure 5-13 illustrates this effect. The effect of the altered path length can be approximately modeled by assuming the object is self-luminous and the scan plane was tilted 30° , approximately double the intended 16° . In this case, the effect is constrained to the y -dimension, so we note that it is independent of the time-delays in the image caused by the angled illumination axis. If arraying was also done in the x -dimension, the artificial aperture doubling would still occur but would be superimposed on the time-delays caused by the angled illumination axis.

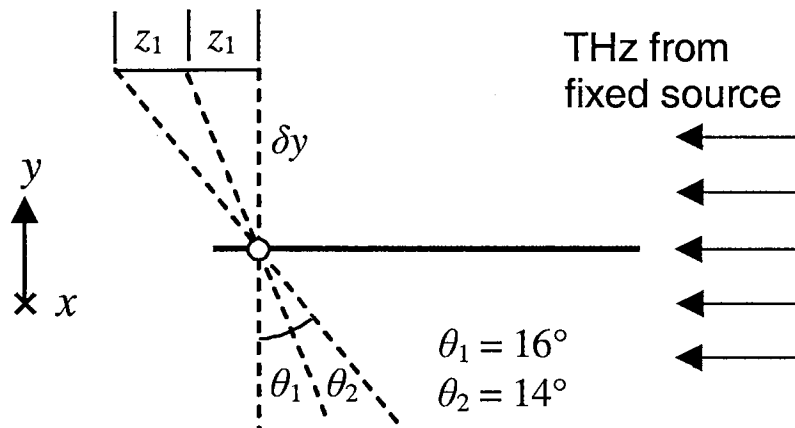


Figure 5-13. Artificial aperture doubling model. Scan planes are shown as dotted lines.

The artificial aperture resizing is more precisely described as follows. We know

$z_1 = \delta y \cdot \tan(\theta_1)$, as shown in Figure 5-13 and since the THz must travel to and from the object, we can say the overall path change is $2z_1 = 2\delta y \cdot \tan(\theta_1)$. However, we can also express this path change in terms of a self-luminous object in another scan plane tilted more than the first. In this case the same path change is expressed as $\delta y \cdot \tan(\theta_1 + \theta_2)$. Equating the two path change expressions and solving for θ_2 yields $\theta_2 = 13.8^\circ$. Hence the fixed illumination source made the synthetic and spherical mirrors appear to have an angular separation of 29.8° , approximately double what was intended. It is notable that this more precise treatment is still not exact because in the tilted configuration the object moves a distance of δy in the tilted direction, not the normal y direction. Suffice to say, the overall consequence is that the effective aperture was not only approximately doubled, as intended, but increased by almost four times in size, thus increasing resolution by about four times, to our advantage. This is a fully justifiable phenomenon as resolution is directly related to observed phase differences [44], something which path length changes cause, by nature. Finally we note that this effect would obviously not occur for a self-luminous object and that the approximate doubling is only evident at small scan plane tilts ($< 20^\circ$). As tilt angles increase, the effect diminishes.

Another verification of the understanding of this doubling effect is evident in the side lobe amplitudes of the composite images. In the THz system, the artificial doubling of the angular mirror separation created an effectively larger but sparser overall aperture, which resulted in greater side lobe levels. A common example of this behavior is the common two-slit optical interference pattern wherein side lobes are as large as the central lobe. This is very similar to the situation illustrated in Figure 2-5, where the resolution is high due to the large angular span of the aperture but side lobes are enhanced due to the

lower relative spatial frequency bandwidth. This phenomenon increased the side lobe amplitudes to the levels seen in Figure 5-10. The theoretical analysis in section 6.5.1 will show a close agreement with these side lobe levels, indicating the understanding of this doubling effect is valid.

Having discussed the aperture doubling effect it becomes necessary to show how it affects the location of the composite image plane. The aperture doubling does not change the manner in which the composite image plane is defined, but it does change its orientation. Figure 5-14 shows how, in the aperture doubled system, the composite image plane still bisects the image planes of the individual elements, but is now tilted at approximately twice the angle shown in Figure 5-12. Even though the *scan planes* were only separated by 16° , the *image planes* were separated by approximately double that, due to artificial aperture doubling. Therefore, to bisect the individual image planes, the tilt of the composite image plane must also double. Nevertheless, the composite image plane still corresponds to the time slice halfway between the pulses from the individual elements. So the method whereby the image in the composite image plane is obtained is unchanged.

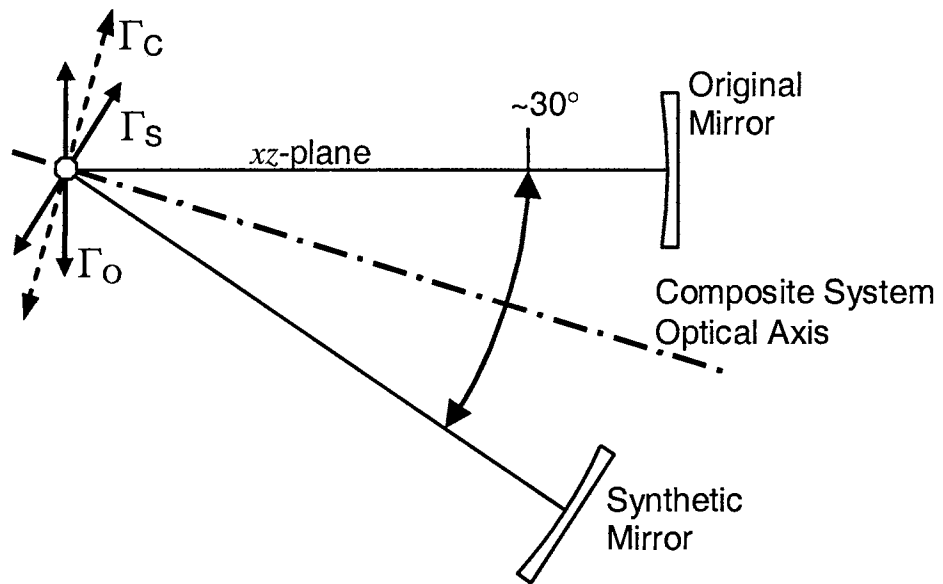


Figure 5-14. Side view of aperture doubled system showing composite image plane.

5.7 Two Point Sources

To further demonstrate the enhanced resolving power of the system, two 391 μm diameter, chrome-plated, steel balls were mounted together to form a double point source object. The successful imaging of this object verified the resolvability of individual features on a more complex structure and determined some higher order effects that interfere with phased-array imaging and resolution in general. The two balls were mounted, as shown in Figure 5-15, on a paraffin wax holder such that they were in contact with each other in y but separated by about 50 μm in z , where the upper ball was more distant from the spherical mirror.

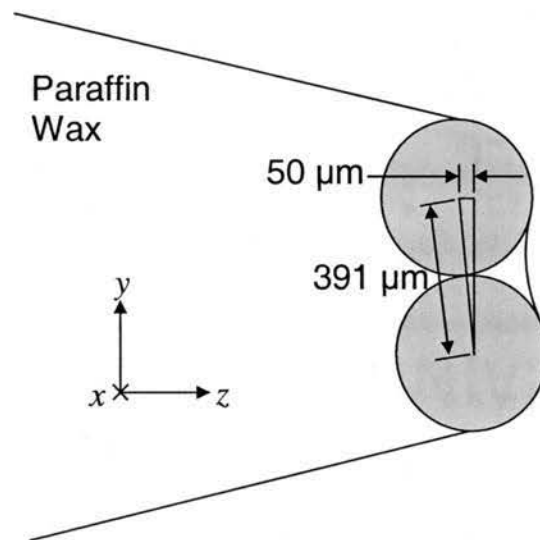


Figure 5-15. Two point source object comprised of two 391 μm diameter steel balls mounted in a paraffin wax holder. Some wax was also present between them at their front face.

Due to the proximity of the balls, it was thought that side lobe levels might interfere with resolution. To reduce these side lobes by filling in the sparse aperture, three images (instead of two) were recorded, each having a different orientation of the

scan plane. The first image was recorded with the scan plane in the normal orientation, or 0° tilt. The second and third images were recorded with the scan plane tilted -10° and $+10^\circ$ about the x -axis to mimic a synthetic mirror located below and above the spherical mirror, respectively. Spatial samples were taken in both the x and y dimensions so the resulting data set had the form $E(x,y,t)$. In all three images a total of 651 spatial samples were recorded; 31 samples in y by 21 samples in x . Spatial sample spacing was $100\ \mu\text{m}$ in both directions so the image spanned a total of 2 mm in x and 3 mm in y . Each spatial sample was a 17 ps, time-dependent waveform that consisted of 256 data points. The SNR of the data ranged from 13 to 120 due to sporadic noise problems and the changing orientations. All three individual images were superposed to generate the high-resolution composite image.

5.7.1 Image Analysis and Enhancement

For the plots of these images, the y -axis was simply labeled “ y ” and represents the y -value on the *composite* image plane, just like the “ Y ” label for the previous images in Figure 5-10. In fact, the synthetic phased-array for this and future experiments contained elements symmetric about the normal configuration. Therefore the composite image plane was coincident with the y and/or x direction. Due to their symmetry, all subsequent composite images will also follow this notation.

Figure 5-16 shows an $x = 0$ volumetric slice through the composite data. The two balls are quite clearly resolved by their specular reflections. Also evident is a double reflection feature occurring later in time. This feature is the multipath effect, mentioned

in section 4.1.2, wherein the THz is first reflected from one ball, to the next, and then to the receiver. Figure 5-17 illustrates this phenomenon. The overall received waveform is therefore approximated as a superposition of four reflection features: two specular reflections and two double reflections. Two specular reflections and one double reflection are illustrated in Figure 5-17 and the other double reflection just follows the reverse path of the first. The changes in path length, caused by scan plane re-orientation, are equivalent for both double reflections, so they always overlap and, together, can be considered one reflection feature.

The double reflection feature becomes important when viewing the transverse images, because it interferes with the resolvability of the balls. Consider the energy image of the two balls shown in Figure 5-18a. This image was created by integrating over the entire temporal span of the image. Though it is weaker, the double reflection is spatially located right between the two specular reflections and acts as clutter in the image. Therefore, in the energy image, the specular features are blended together by the double reflection and the resolution of the balls is destroyed. The resulting general implication is that a system may be well-corrected and have a sufficiently low diffraction limit to resolve the object features, but resolution may still not be possible due to higher-order effects. This would be a significant problem in an incoherent system, where filtering in the time-domain would not be possible. However, the THz system is coherent and the double reflection feature, which occurs later in time than the specular features, can be windowed out of the data.

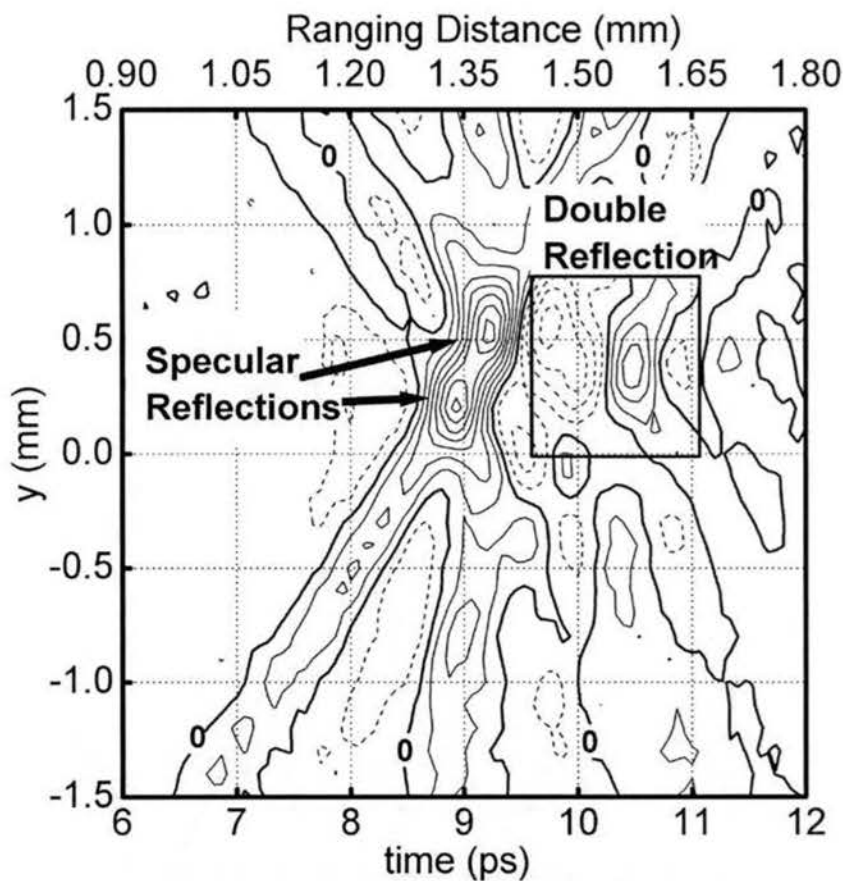


Figure 5-16. Slice at $x = 0$ through two-ball composite image. Contours are separated by 7 pA. Negative contours are indicated by dashed curves.

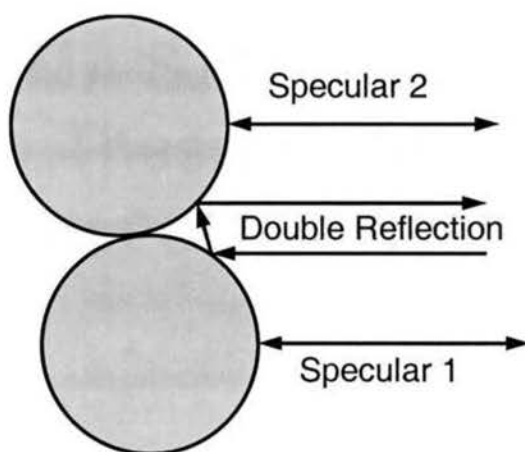


Figure 5-17. Reflection features from two 391 μm balls.

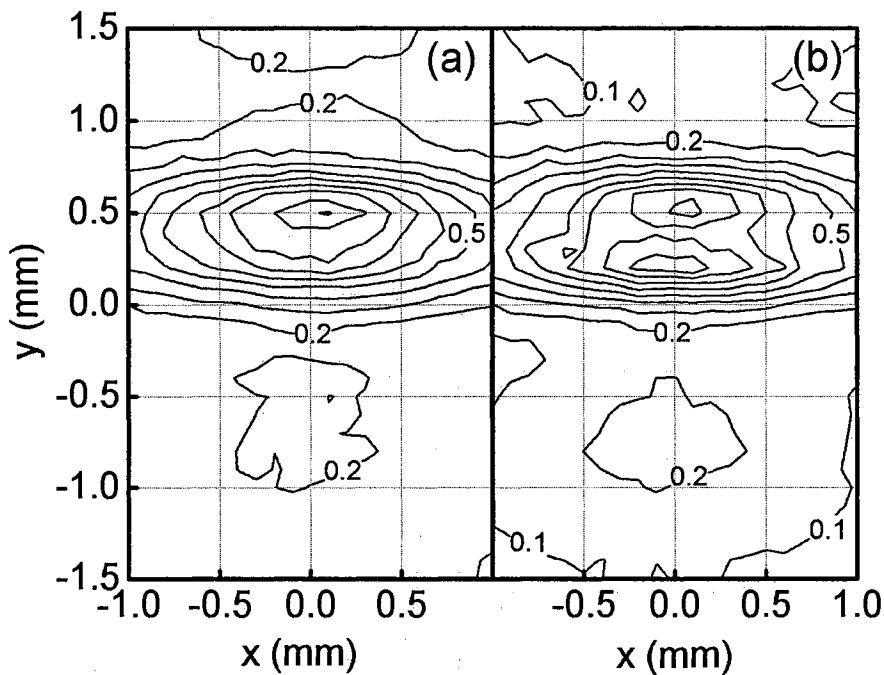


Figure 5-18. Transverse energy image for two 391 μm balls. (a) image containing double reflection feature. (b) image with double reflection feature time-excluded prior to integration.

By excluding the data containing the double reflection ($t > 9.6$ ps) from the integration, the detrimental effect is removed. Figure 5-18b shows the same energy image as Fig. 5-18a after time-excluding the double reflection feature. The resolvability of the balls reappears in the transverse image.

Figure 5-19 shows another transverse image obtained by plotting the surface of a volume wherein the raw amplitude data have a value greater than a fixed threshold. In this case the threshold value is 40 pA, approximately 80% of the peak value. The data is processed in a binary fashion where only values of sufficient amplitude are retained and all other values are discarded. The transverse image of the two balls is then plotted as the surface of the volume containing the retained values. This method removes the double reflection features while retaining the stronger, specular features.

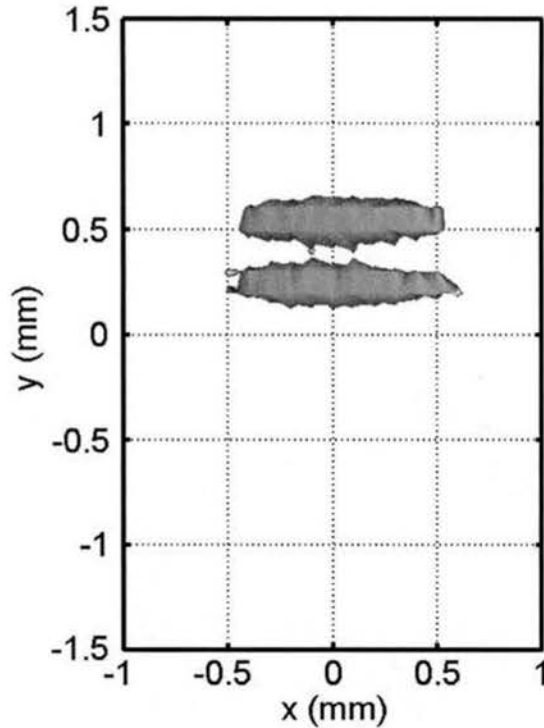


Figure 5-19. Transverse isoamplitude plot of two 391 μm balls. Surfaces contain data values which have amplitude of greater than 40 pA. (or 80% peak amplitude).

The images of Figures 5-18 and 5-19 clearly show the resolution gain in the y direction allowing discrimination of the two 391 μm balls, despite the fact that they are somewhat temporally blended together. Artificial aperture doubling and the accompanying resolution gain in the y direction is present as expected, and no resolution gain is present in the x direction.

The images also demonstrate a few of the image processing and enhancement techniques available to this system by digitally storing the coherent, phase-referenced individual images. Such techniques permit imaging of smaller or less reflective objects, imaging of objects in clutter, and filtering of undesired features. Unwanted image

anomalies are often distinguished by later arrival, weaker amplitude response and/or altered spectral response. Hence, temporal feature exclusion, amplitude thresholding, and frequency filtering, in both the temporal and spatial domains, are all valid signal processing techniques.

5.7.2 Ambiguous Phase Reference

During the phased-array imaging of the single point source, the images were phase locked to each other by ensuring that the waveforms of the spatial samples at the origin overlapped exactly. This task required that these reference waveforms be very similar in shape and size for both images. This was not a problem for the single point source since the only feature present in the waveforms was the single specular reflection from the ball, unchanged by re-orientations. However, this was a significant problem for imaging the two 391 μm balls. Based on previous calculations, the THz system has range resolution of 81 μm . But the z -separation between the two balls during this experiment was only about 50 μm . Consequently the specular reflections from the two balls blended together in time, making it impossible to use either of them as a reference. Figure 5-20 shows the reference waveform for the 0° orientation as the solid curve. The specular reflections from the two balls (at about 8.5 ps) have blended together into one peak. The phase reference problem is further aggravated by the other imaging orientations. When the scan plane was tilted about the x -axis the time-delay between the specular reflections changed; this reshaped the waveforms and made them impossible to properly overlap. Figure 5-20 shows the reference waveforms for the $+10^\circ$ and -10° orientations as dashed

and dash-dot curves respectively. To clarify the figure, the $+10^\circ$ and -10° waveforms are shifted by $+20$ pA and -20 pA, respectively.

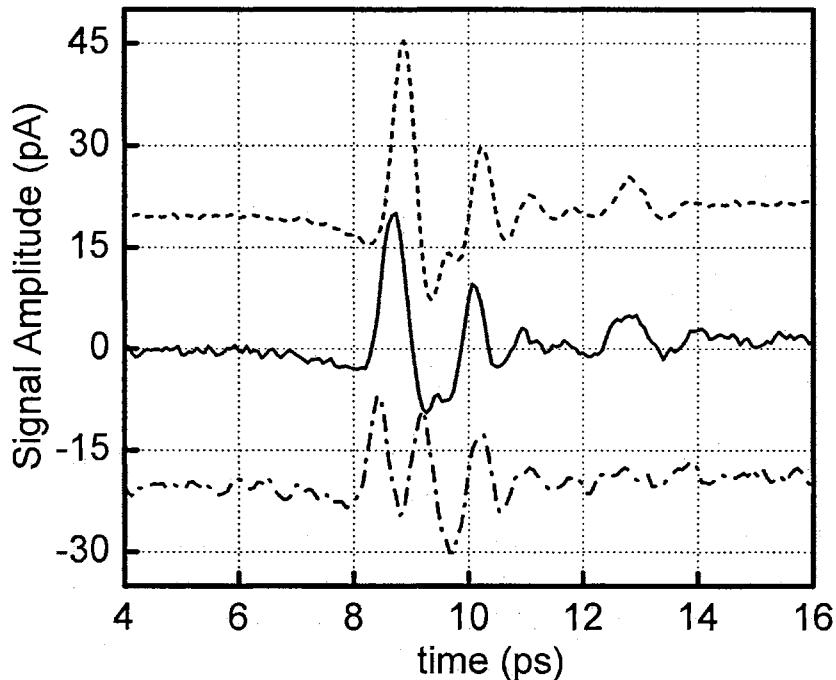


Figure 5-20. Phase reference waveforms for three images of the $391 \mu\text{m}$ balls. Solid curve for 0° , dashed curve (shifted 20 pA) for 10° , dash-dot curve (shifted -20 pA) for -10° orientations.

The specular reflections became resolved when the object was tilted in the -10° orientation because the tilt caused the spatial ball separation in the z direction to increase beyond the range resolution limit. The specular features interfered more constructively in the $+10^\circ$ waveform than in the 0° waveform, thus making the $+10^\circ$ waveform attain greater amplitude. The local maximum at about 10.2 ps corresponds to the double reflection.

Though it was not possible, ideally the phase relationship would have been established by overlapping the waveform portions corresponding to the specular

reflection from only one of the balls. This would ensure that the location of this reference ball would have been common for all orientations and would establish an absolute phase reference. For lack of a better alternative, the reference waveforms were positioned such that their features were simply near each other. This locked the images together in some phase relationship albeit an incorrect one.

5.7.3 Image Reconstruction

Since the proper phase reference was not established during imaging, some image reconstruction was necessary. In that sense this experiment demonstrated the problems associated with most AS system wherein such reconstruction is constantly necessary. The difficulty of this reconstruction process was in the fact that the amount of phase error between the images was heretofore unknown and therefore un-correctable.

One important property of the individual images, however, was that all their spatial samples had the same phase error as each other. Since the phase error is manifest as timing shifts, all the spatial samples of any single image had the same undesired temporal shift. Therefore, to get the correction to the phase error of an entire image, it was only necessary to find the errant temporal shift in one spatial sample. By applying the necessary time-shift correction equally to every sample, it was possible to correct an entire image.

To begin finding the error it was necessary to temporally isolate the single specular reflection from the reference ball in each reference waveform. Upon isolation, the temporal location of this specular reflection could be measured for each orientation.

Assuming the reference ball should have a common location at the origin for all three images, the differences between these temporal location measurements would establish the phase error.

To begin the analysis, it was assumed that the overall waveforms consisted of a specular reflection from each ball and the double reflection feature. As the tilt of the scan plane changed, the temporal separation between these individual features also changed, and caused their superposition waveform to change shape, as shown in Figure 5-20. To better understand this reshaping, four more reference waveforms, similar to those in Figure 5-20, were collected, each at different scan plane orientations. The additional orientations were $+5^\circ$, $+15^\circ$, -5° and -15° . Figure 5-21 shows all the reference waveforms together. It is noted that, in this plot, the vertical axis is used to designate the scan plane orientation, not the amplitude of the waveforms. Also, all the waveforms are scaled equally in amplitude. The figure clearly shows two pulses merging together into one and passing through each other as a function of scan plane orientation. These are the specular reflections from the balls. The double reflection feature stays almost fixed in this figure.

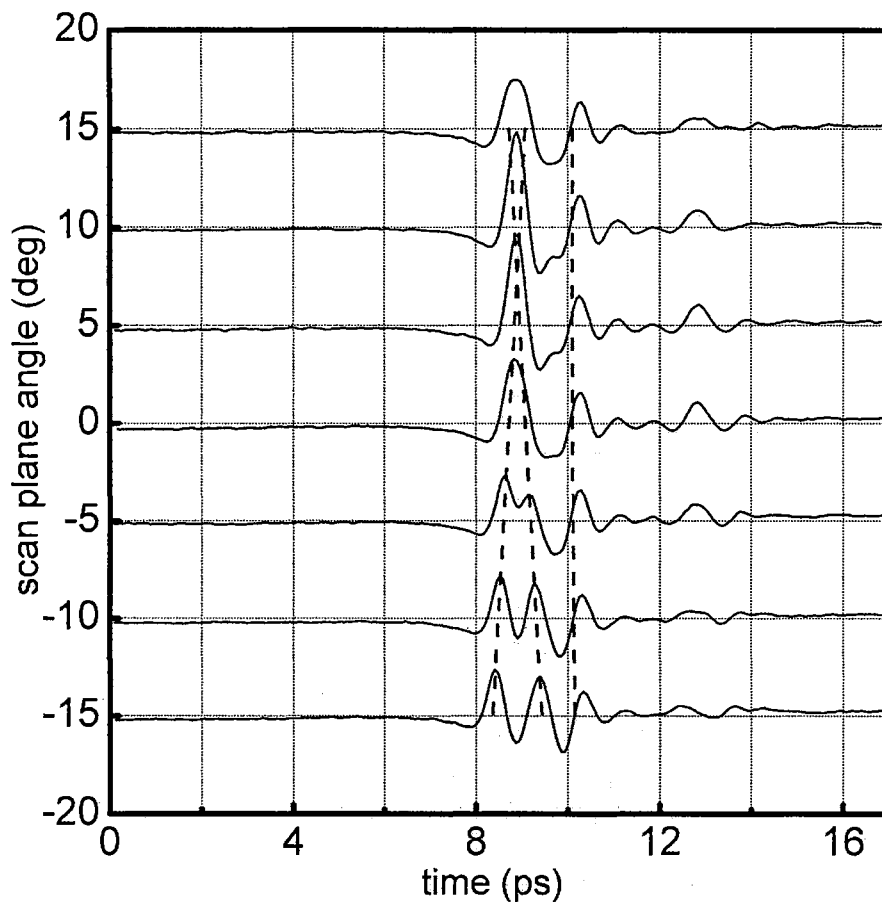


Figure 5-21. Reference waveforms for seven scan plane orientations and calculated timing changes of reflection features (dashed lines).

Using geometry, the expected timing changes for the individual reflection features can be calculated as a function of scan plane orientation. The result of this calculation is shown as the three heavier, dashed lines passing through the waveforms in Figure 5-21. The lines show excellent agreement with the behavior of the individual reflection features in the waveforms indicating the behavior of these features was understood. It is noted that the reference waveforms were shifted in time to line up properly with the calculation results but this doesn't affect the relative timing relationships between the individual reflection features themselves.

The calculated information showed where the waveforms were supposed to be to establish a phase reference. For example, if the desired phase reference was the double reflection pulse then we would expect this feature to remain fixed in time regardless of orientation, almost exactly how it appears in Figure 5-21. The actual data waveforms would then have to be shifted in time such that they appear as they do in Figure 5-21. Shifting the entire image equivalently would then lock the images in proper phase.

To establish proper timing relationships more accurately, model pulses were constructed to mimic the data. These models were the superposition of three component waveforms, each corresponding to a reflection feature from the object. The individual components could be shifted in time relative to each other to examine how their superposition would change shape. The shape of the waveform from a single specular reflection was already known from previous experiments, and an idealized version of it was used to create the model components corresponding to the specular reflections. A slightly modified version was used to model the double reflection. By properly adjusting the temporal location of these components it was possible to sum them together and create waveforms which were very similar in appearance to the actual data. Modeling the data as such revealed where the individual components of the actual data were temporally located. Comparing this to their desired location (previously calculated) it was possible to extract the timing (phase) error.

Figure 5-22 shows one model waveform overlapping actual data. In this figure, the model waveform components are shown together with their superposition and the actual reference waveform for the 0° orientation.

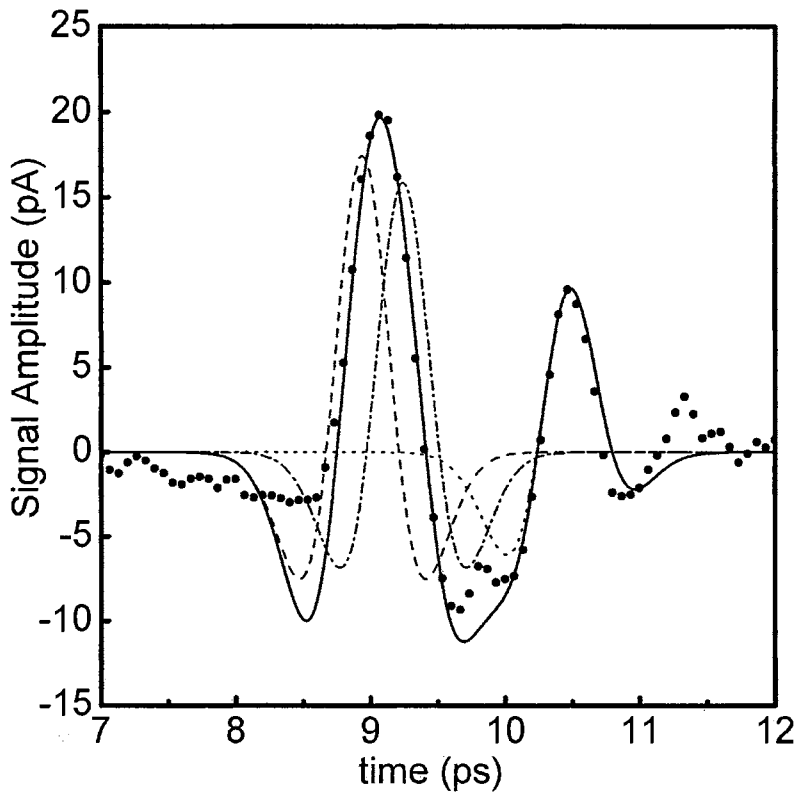


Figure 5-22. Overlap between actual 0° reference waveform, shown as filled circles, and matching model waveform with its components. The specular reflection models are shown as the dashed and dot-dashed curves. The double pulse model is shown as the dotted curve and the superposition of all three model waveforms is the solid curve.

The actual data, shown by the filled circles, overlaps well with the superposition model, indicating that the model components reasonably mimic the reflection features from the actual data. By assuming the components in the actual data were in the same location as the components in the model data, the timing of each individual reflection feature in the actual data was isolated. By applying different relative time-shifts to the *same* three model components it was possible to model the actual reference waveforms of the other six orientations with similar fits. Figure 5-23 illustrates three of these fits. It is stressed that the model waveform components were not changed in shape but only shifted in time to achieve these matches. In this way the temporal location of the components of

the actual data waveforms was established, as well as the phase error.

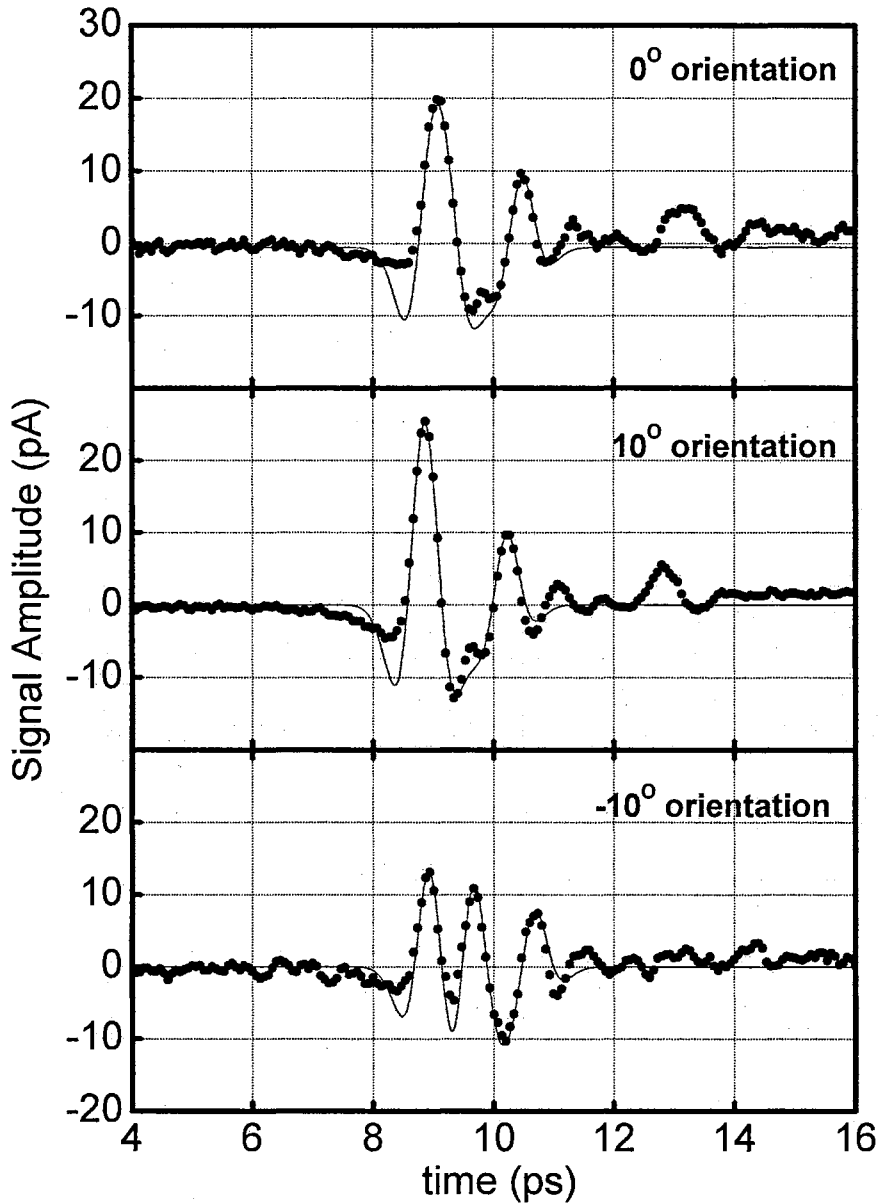


Figure 5-23. Overlap between model waveforms and actual data.

By assuming the phase was already correct in the 10° data it was only necessary to correct the error in two images. It was found that the 0° data had to be shifted 392 fs later and the -10° data had to be shifted 492 fs later. The images shown in Figures 5-16,

5-18 and 5-19 all incorporated this phase correction, which was necessary for the discrimination of the balls.

5.7.4 Array Steering

In section 5.7.1, a couple of forms of image processing were used to recover the resolution in the image of two 391 μm balls. Due to its coherent nature, there are many types of unique image processing or enhancement techniques available to the THz system. Array steering is one such technique and illustrates one of the major benefits of phased-array radar systems: the ability to steer the beam electronically rather than mechanically. One method by which this is done is by applying phase shifts to individual array components, similar to the shifts used to correct the phase reference for the THz images of the two 391 μm balls. The following experiment showed that array steering can also be applied to the phased-array THz imaging system.

The phase error correction which was successful in recovering the image of the two 391 μm balls was accomplished by using the specular reflection off the lower ball as a phase reference. It was only assumed throughout the analysis that the origin samples (at $x = 0$, $y = 0$) were used to establish that phase reference. If this were the case, the reference (lower) ball would have been located at $y = 0$ in the images of Figure 5-16, 5-18 and 5-19. Instead, the images showed the reference ball was centered at approximately $y = 200 \mu\text{m}$. This demonstrates the fact that, in actuality, the $y = 200 \mu\text{m}$ waveforms were used as phase references. By using these waveforms, it was assumed that the lower ball was centered at $y = 200 \mu\text{m}$. Then, using these waveforms to repair the phase error

consequently phase locked (steered) the array to this point.

In a similar fashion, it was possible to use either the specular reflection off the other ball or the double reflection to reference the images. This was done by once again adjusting the phase of the images such that the desired reference features from each orientation perfectly overlapped in the reference waveforms. Figure 5-24, an $x = 0$ slice, shows the result of using the second specular reflection (the upper ball) as a phase reference. The entire image has shifted down in the y direction by approximately $382 \mu\text{m}$, indicating that the array was now steered to a spot about $382 \mu\text{m}$ above the original. This corresponds almost exactly with the relative position of the upper ball with respect to the lower ball. Again the $y = 200 \mu\text{m}$ waveforms were used to establish the phase lock; therefore the upper ball became centered at this point.

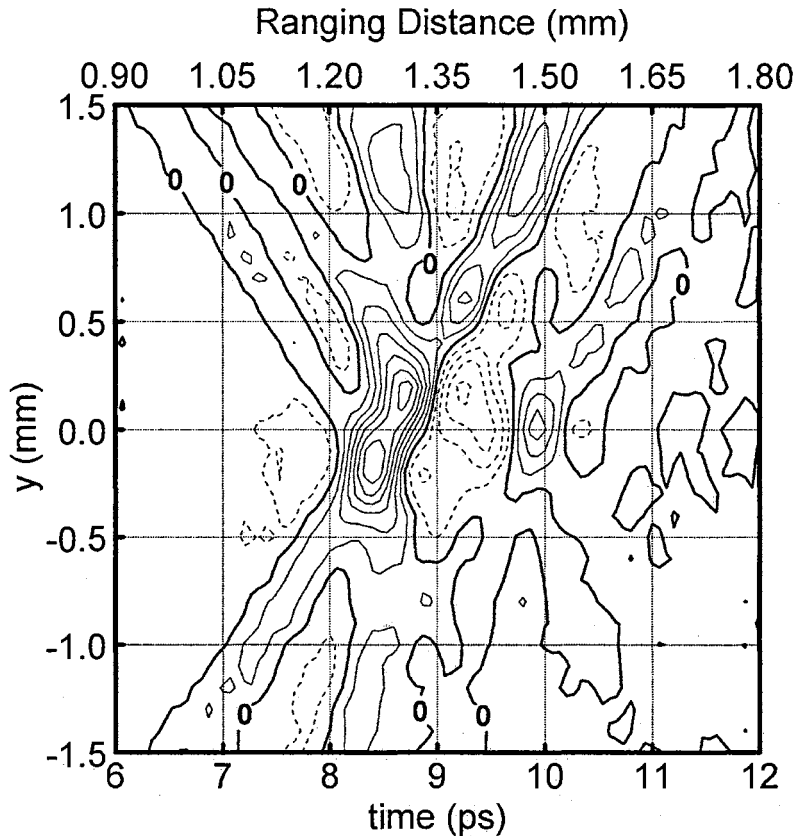


Figure 5-24. Slice at $x=0$ through image of two $391\ \mu\text{m}$ balls with array steered to upper ball phase reference. Contours are separated by $7\ \text{pA}$. Negative contours are indicated by dashed curves.

It was also shown that the array could be steered to some arbitrary point in space which did not correspond to any physical object at all. Since the composition and behavior of the reference waveforms were understood from previous work, it was possible to extrapolate their relative timing changes to determine what they would look like locked to some arbitrary reference. By shifting the actual data to match these calculations, the phase reference was locked to an arbitrary location somewhere above the upper ball. Figure 5-25 shows the result of this experiment.

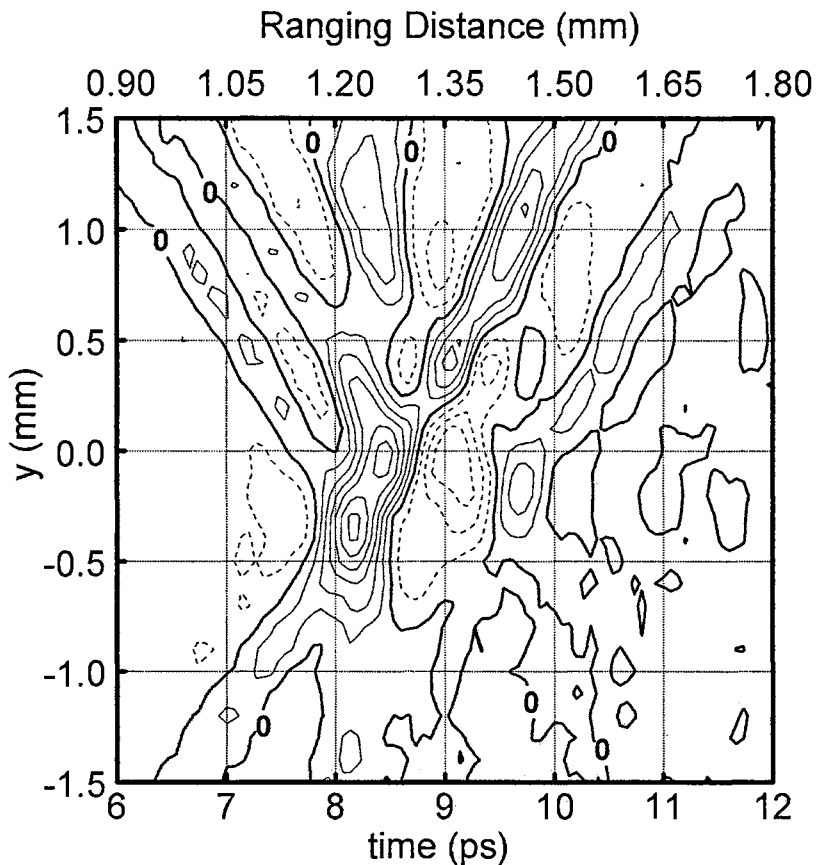


Figure 5-25. Slice at $x = 0$ through image of two $391 \mu\text{m}$ balls with array steered to arbitrary phase reference above upper ball. Contours are separated by 7 pA . Negative contours are indicated by dashed curves.

Clearly the image had shifted again in the y direction, this time by about $530 \mu\text{m}$ down from the original. This shows the possibility of array steering and demonstrates the ability of the system to *extrapolate* image information where it was never actually recorded. The validity of this data certainly doesn't extend out indefinitely, but for small regions around the normal arrangement it is clearly usable.

Much of the image processing shown here was possible only because of *a priori* knowledge of the object. Array steering, for example, was first accomplished by locking array elements to known features on the object. Such information is not generally

known, but similar methods can still be used. Once the elements of the array are in some known phase relationship, they can be steered to look in a desired direction regardless of object characteristics. This was demonstrated by steering the array to a point in space not occupied by the object at all.

Finally, it is noted that all phase correcting, filtering, and steering was done after the data was fully collected. All the capability to form the high-resolution image was stored in the individual images. To actually form that image, it was only a matter of finding their correct timing relationship. This demonstrates both the power and flexibility of the coherent THz imaging system and coherent, quasi-optical imaging systems in general.

5.8 Two-Dimensional Phased-Array Imaging

Having shown the system's phased-array capabilities in the vertical direction it was necessary to ensure similar behavior in the horizontal direction. To accomplish this a new object was constructed out of a single $391 \pm 3 \mu\text{m}$ diameter, chrome-plated, steel ball and two small cylindrical strips of solder, each having a diameter of about $420 \pm 10 \mu\text{m}$, and fashioned together into the shape of a T. The T portion lied in the plane perpendicular to the system optical axis. Figure 5-26 shows a scale diagram of the T-ball object.

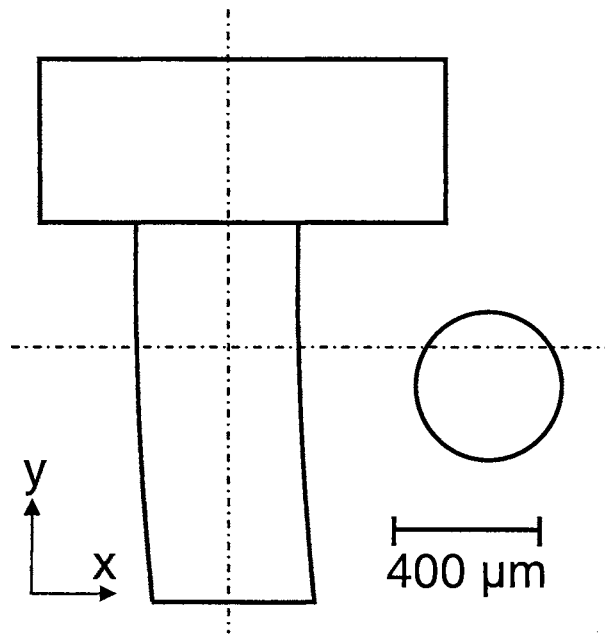


Figure 5-26. Scale diagram of T-ball object. The dash-dot lines indicate the center of the data set.

To avoid the phase reference problems present in the previous experiment the ball was mounted such that it was closer to the spherical mirror along the z direction by about $260\ \mu\text{m}$. As a result, the reflection from the ball arrived at the receiver about $1.7\ \text{ps}$ earlier than the reflection from the T so the ball could act as the lone phase reference regardless of scan plane orientation.

To increase resolution in both the x and y directions, and to reduce side lobes, five images were recorded, each having a different orientation of the scan plane. The first image was recorded with the scan plane in the normal orientation, or 0° tilt. The second and third images were recorded with the scan plane tilted $+10^\circ$ and -10° about the y -axis to mimic synthetic mirrors located to the left ($-x$ direction) and right ($+x$ direction) of the spherical mirror, respectively. The fourth and fifth images were recorded with the scan plane tilted $+10^\circ$ and -10° about the x -axis to mimic a synthetic mirror located above and

below the spherical mirror, respectively. Spatial samples were taken in both the x and y dimensions so the resulting data set had the form $E(x,y,t)$. In all five images a total of 837 spatial samples were recorded; 31 samples in y by 27 samples in x . Spatial sample spacing was $100\ \mu\text{m}$ in both directions thus the image spanned a total of 2.6 mm in x and 3.0 mm in y . Each spatial sample was a 17 ps, time-dependent waveform that consisted of 256 data points, each spaced by 66.7 fs. Peak SNR's ranged from about 25 to 100.

The images were collected with the proper phase relationship by using the specular reflection from the ball as the reference. Therefore, the images were simply superposed to form the composite image. Due to the relative complexity of the object it was more difficult to find a method whereby it could be displayed. Individual slices through the volumetric data proved unusable for visualization. Therefore, it was determined that energy images, obtained by integrating sections of temporal data, would work best.

For this method to work it was necessary to somewhat process the data. Instead of integrating over the entire temporal span, the data was split into two sections. The first section consisted of the temporal region extending from $t = 0$ to 5.6 ps. This region incorporated only the occurrence of the specular reflection from the ball. The second section consisted of the temporal region extending from $t = 5.6$ to 17 ps; incorporating only reflections from the T. Each section was squared and integrated over time to form two partial-energy images. These images were then *separately* normalized to yield the images shown in Figure 5-27a and 5-27b.

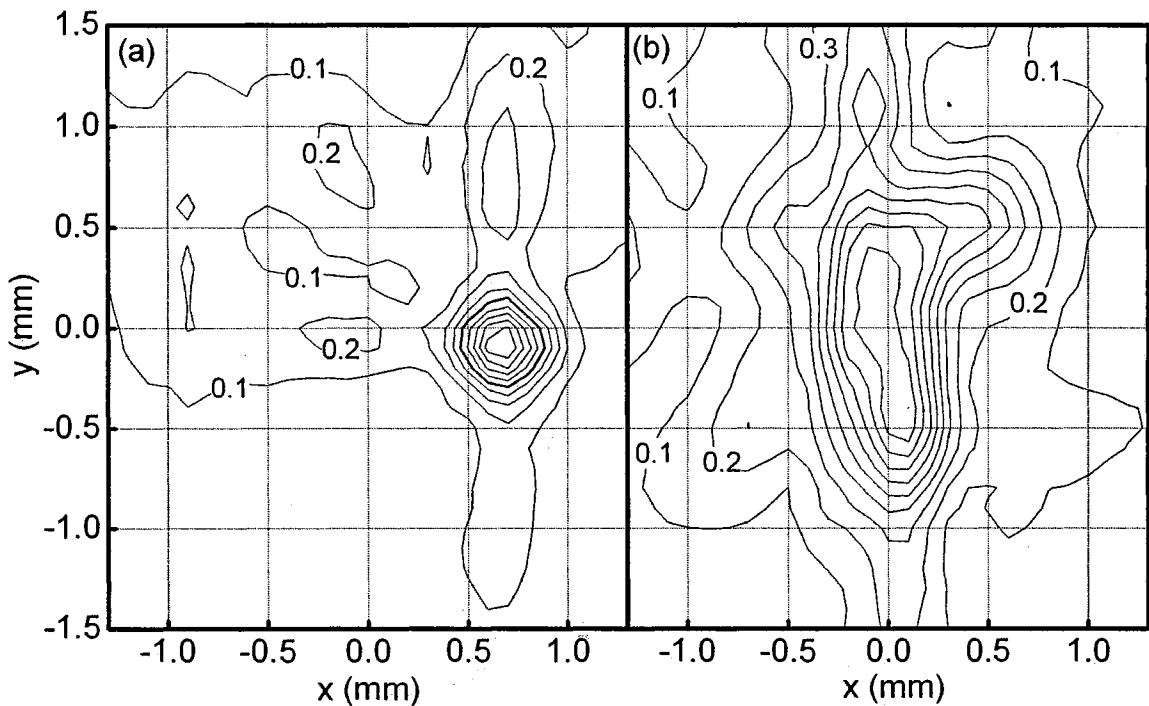


Figure 5-27. Partial energy images of the T-ball object, both separately normalized. Contour separation is 0.1. Heavy contour shown in (a) is used to illustrate FWHM of the dual-axis arrayed image of a point source.

The ball is clearly resolved in Figure 5-27a and shows that the phased-array imaging was successful in both the x and y directions. The FWHM measurement of the ball, in this energy picture, is $435\ \mu\text{m}$ in both the x and y directions. The T, shown in Figure 5-27b also exhibits features which are evident only because of the increased resolution in both directions. The physical pieces of solder comprising the T were not very uniform and could explain why the T appears thicker than the ball. Nevertheless, when both of these images are overlapped, the transverse resolution between them becomes apparent. This overlapped image is shown in Figure 5-28 and the method by which it was obtained will be further discussed shortly. Note, however, that the T and the ball are both located where they are supposed to be and are resolved in both the x and y directions.

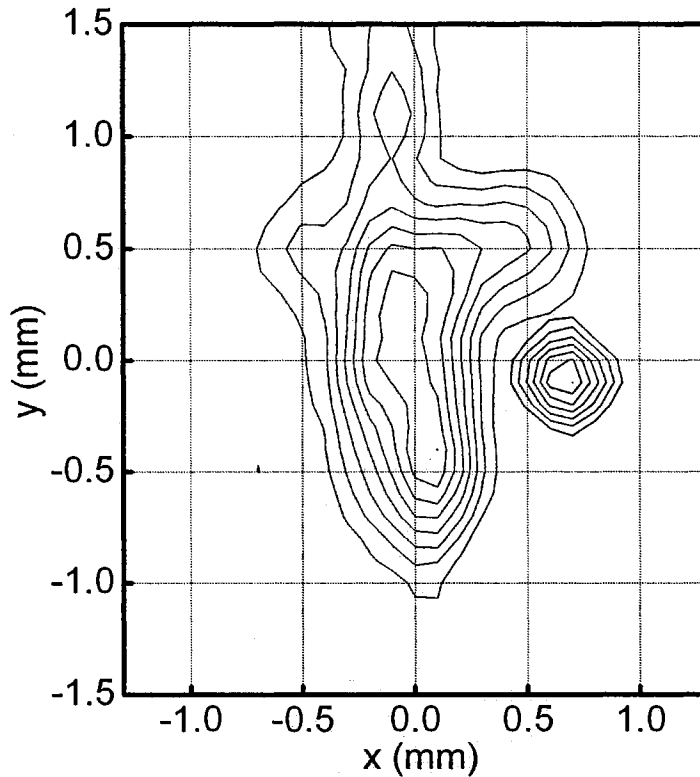


Figure 5-28. Overlap of normalized T and ball partial-energy images. Contours for 0.1, 0.2 were removed from both pictures. Contour for 0.3 also removed from ball picture.

Further explanation is required to help understand the image in Figure 5-28. No contours are labeled on it because the normalization factor for the ball and the T were quite different. The T, having cylindrical surfaces, reflected far more THz than the ball and its energy image was stronger than the ball's. In order to make the ball visible against the T, each was normalized separately. If this was not done, the small amount of energy in the ball reflection would be masked by the large energy of the T reflection. Figure 5-28, therefore, shows the energy images from 5-27a and 5-27b, separately normalized and overlapped, but not added together. Figure 5-29 shows the energy image resulting from actually *adding* the T energy image to the ball energy image, without first

normalizing them separately. Since the peak energy in the T is about 8 times higher than the peak energy in the ball, the resulting image looks almost exactly like Figure 5-27b and the structure of the ball is almost completely invisible.

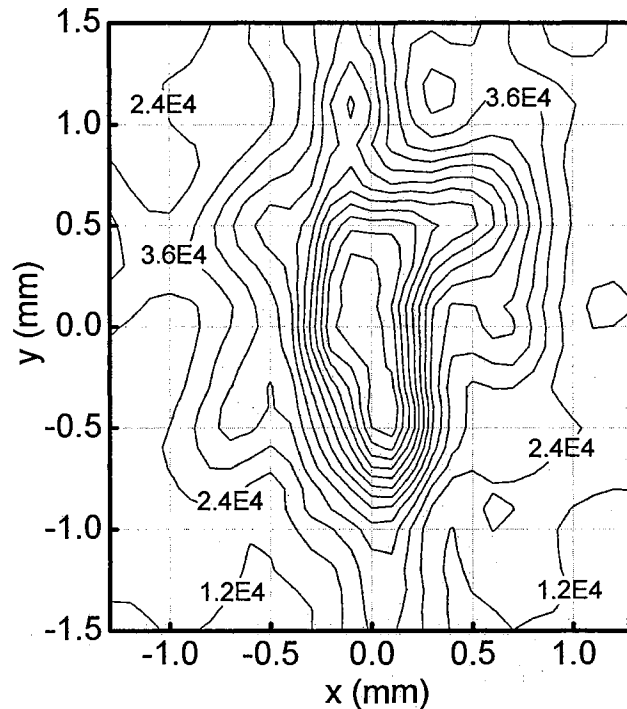


Figure 5-29. Energy image of T-ball with no separate normalization for T and ball portions. Contour separation is 1.8×10^4 and the peak value is 1.68×10^5 expressed in arbitrary energy units.

5.8.1 Object Stealth

One thing to notice on Figure 5-27b or 5-28 is the lack of image fidelity exhibited in the top (horizontal) portion of the T. This region of the image is far weaker than the vertical region just below it. This effect is yet another owing to the fact that the object is not self-luminous. As illustrated in Figure 5-30, both portions of the T lie in a plane perpendicular to the system optical axis so that, in the normal scan plane configuration (0° tilt), the top portion of the T reflects the THz as a horizontal cylindrical wave

spreading in a direction which is not coincident with the spherical mirror. However, the bottom portion reflects a vertical cylindrical wave which compensates for the off-axis illumination, and thereby intersects the mirror. This stealth behavior is present in any object with flat features.

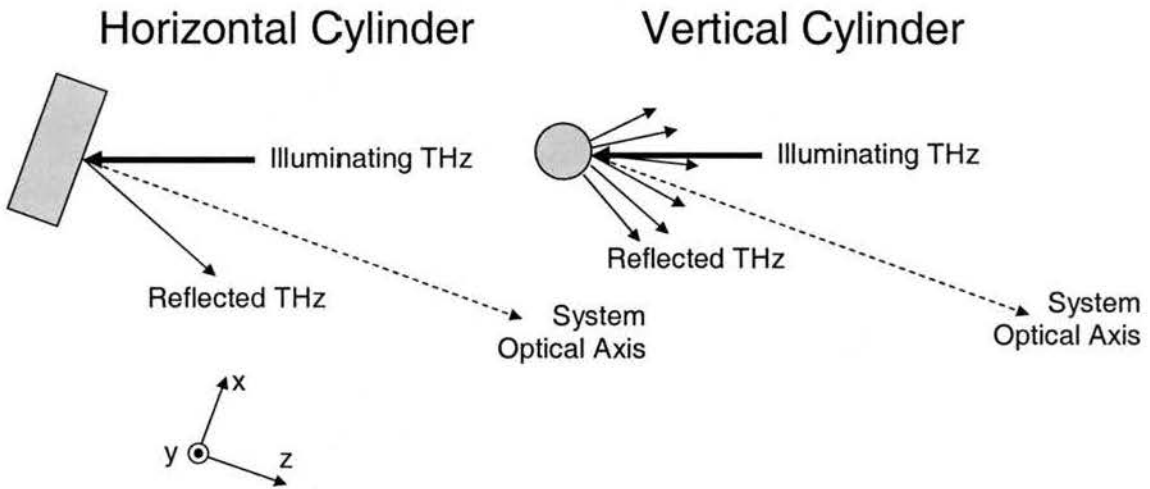


Figure 5-30. Object stealth behavior for horizontal and vertical cylinders.

The situation is also altered by the different orientations of the scan plane. For example, when the scan plane is rotated $+10^\circ$ about the y-axis, the normal to the horizontal T portion almost bisects the 17° angle between the illumination and the system optical axis. This allows the top part of the T to reflect some radiation back to the spherical mirror. On the other hand, the -10° orientation only aggravates the stealth condition because the THz is reflected even farther from the spherical mirror. Varying orientations about the y-axis does not affect the vertical T portion because of its cylindrical shape.

In a similar fashion the orientations rotated about the x-axis do not affect the

response of the horizontal T portion, but they do affect the vertical portion. Therefore, the vertical T portion has three of five orientations wherein its response is very significant. Fortunately, these three orientations are also those needed to produce the increased resolution in the x direction. The horizontal T portion, however, has only one of five orientations wherein its response is significant. Hence, it does not register well on the overall image. It is noted, however, that the surfaces of the T are not perfectly smooth; therefore the diffuse reflections from its surface allow the T to be more visible than geometric considerations alone would predict. As expected, no stealth properties are apparent on the ball since it scatters radiation toward the spherical mirror regardless of its orientation.

Chapter 6

Theoretical Analysis

In an effort to gradually improve the description of the THz imaging system, three different models were used, each incorporating more of the physical characteristics of the system. Regardless of the specific approach, all the models used a combination of ray-tracing and diffraction theory, to some extent. Ray-tracing, or geometric optics, was used to determine the field distribution in or near a certain plane containing the exit pupil. From this point the remainder of the modeling was done with diffraction theory. This combined method is well-known [26] and has two important benefits: relative simplicity and maintenance of the ability to accurately describe the complex focal region.

6.1 Formulation of Models

To begin the analysis, the THz imaging system must be thought to consist of two separate imaging sub-systems. In the first sub-system, the spherical mirror forms an intermediate image of the object in a plane located about 17 mm in front of the receiver. In the second sub-system, this intermediate image is, once again, imaged onto the receiver dipole antenna by the silicon lens. As previously discussed, the spherical mirror forms the exit pupil (and is the most limiting aperture) in the system, so the silicon lens system can be

sufficiently modeled with ray tracing techniques alone, whereas the model of the spherical mirror system must include the effects of diffraction. For this reason, it was initially assumed that the silicon lens system was well-corrected and introduced no new diffraction effects. It was also assumed that the dipole antenna was an ideal sampler of the image projected onto it. Under these assumptions the receiver as a whole, could simply be considered an ideal sampler of the image formed by the spherical mirror. Therefore, the modeling of the entire THz system needed only include the imaging of the object by the spherical mirror. This approach had the added utility of yielding results in the same form as the data. As will be shown, these assumptions proved to be valid in accurately describing the behavior of the THz imaging system.

6.1.1 Input Pulse

For all the models, the same idealized version of a THz pulse was consistently used to define the input to the calculations. Objects were considered self-luminous with radiation in the form of this ideal THz pulse. The pulse and its spectrum are shown in Figure 6-1. It was modeled after actual THz pulses measured in the lab with the exception that it was given a frequency independent phase shift of approximately $-\pi/2$ with respect to the pulses from the recorded data. This was intentionally introduced to offset the $\pi/2$ phase shift introduced by a $-j$ coefficient in the diffraction calculations in all three models, and thereby give the calculated results the same form as the data. As explained in section 3.7 of reference [23], this shift can be understood by noting that the field in the image plane is proportional to the time-derivative of the field in the

diffraction plane. This derivative is partially manifest as the $1/j$ term, which corresponds to a positive $\pi/2$ phase shift because of the chosen phasor notation. This will be discussed in much greater detail in section 6.1.3.

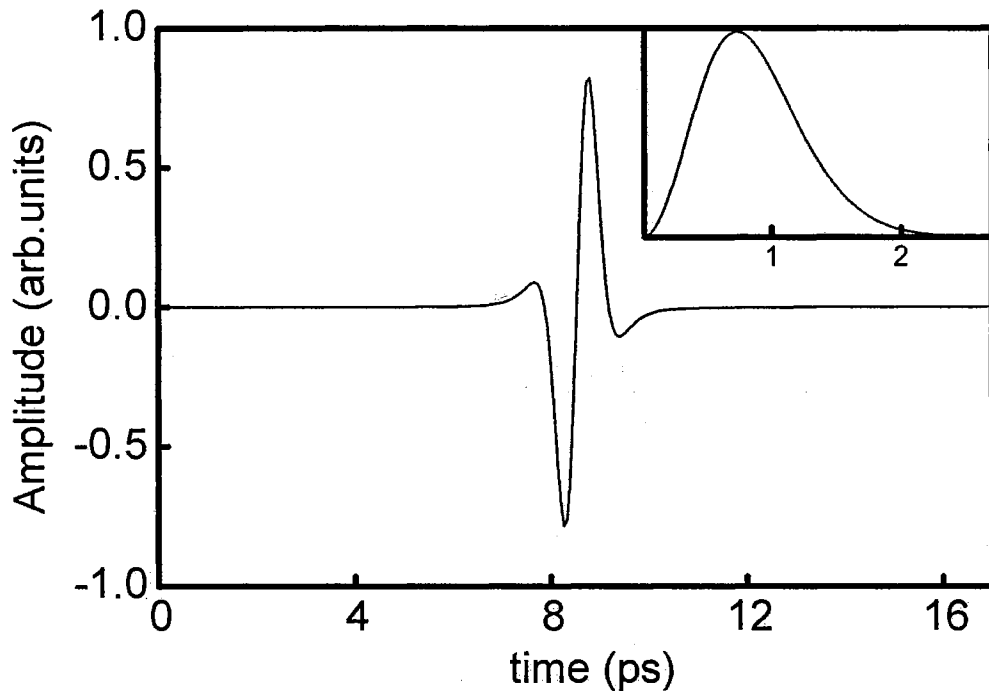


Figure 6-1. Ideal input pulse for theoretical calculations. Inset shows normalized amplitude spectrum with horizontal axis in units of THz.

6.1.2 Initial Approximations

All three models share some inherent approximations common to imaging systems analyses. The medium of wave travel is assumed to be isotropic, homogeneous, linear, non-dispersive, non-magnetic and source-free. None of the optics in the system rotates the field polarization and aperture edge effects are ignored. At the same time, the diffraction solutions are all valid solutions of the scalar wave equation and apply equally

to all components of the electric and magnetic fields. Therefore, fields can be expressed as scalars rather than vectors.

6.1.3 Phasor Notation

One of the more formidable obstacles in THz research seems to be the fact that it is often best described by a blend of several other fields of study. In some cases it follows strict electromagnetics principles, in other cases it is modeled very well by general optics principles. Sometimes, however, a mix of several principles is necessary. The problem arises in the fact that different fields of study use different mathematical notation. Such a problem is present in the study of diffraction phenomena and is manifest as a discrepancy in expressing the fields in terms of phasors.

Specifically, optics references [23-26], use a notation wherein the phasors rotate in a clockwise direction as time moves forward. Equivalently, their time-dependence is of the form $\exp(-j\omega t)$. This means that if we move in space so as to intercept portions of a wavefield that were emitted later in time, the phasor will have advanced in the clockwise direction, and the phase of the wave should become more negative, and vice-versa [23]. Using this phasor notation, we can generally express the instantaneous scalar field, $F(t)$, of a monochromatic wave as

$$F(t) = \Re[\tilde{F} \exp(-j\omega t)], \quad (6-1)$$

where $\Re[\]$ denotes the “real part of” and “ $\tilde{\cdot}$ ” is used to denote the phasor notation of F . In a related fashion, the inverse Fourier transform can be used to express the

instantaneous scalar field for a polychromatic wave as a function of its spectrum, $F(\omega)$.

More specifically,

$$F(t) = \frac{1}{2\pi} \int_{-\infty}^{\infty} F(\omega) \exp(-j\omega t) d\omega. \quad (6-2)$$

Note that this form of the inverse Fourier transform has a negative argument in the exponential. Herein lays the potential confusion. This is not the standard form of the inverse Fourier transform used in most electrical engineering disciplines, even though it is completely valid and appropriate for the chosen phasor notation. More precisely, the basis functions for the inverse Fourier transform must share the $\exp(-j\omega t)$ time-dependence assumed by the phasor notation.

For the sake of following the more useful optics references, this phasor notation will be used to describe the THz imaging system and will necessitate the version of the inverse Fourier transform in equation 6-2. Its transform pair then takes the form

$$F(\omega) = \int_{-\infty}^{\infty} F(t) \exp(j\omega t) dt. \quad (6-3)$$

It is further noted that, in this notation, a *converging* spherical wave takes the form $\exp(-jkr)/r$, whereas a *diverging* spherical wave takes the form $\exp(jkr)/r$. This unity-amplitude, diverging wave is called the free-space Green's function [23] and is at the very heart of diffraction theory. This is the common *optics* notation for the free-space Green's function and it is the basic reason the optics form of the Fourier transform must be used. Other fields, such as ultrasonic imaging [33], radar imaging [44] and general Fourier array imaging [49] use a counterclockwise phasor notation wherein the Green's

function is expressed as $\exp(-jkr)/r$, which permits the use of the electrical engineering form of the Fourier transform.

Again, since the THz imaging system is quasi-optical and most of the theoretical analysis comes from optics references, the optics notation shall be used throughout. For the monochromatic portions of the theory this notation is somewhat irrelevant, but it must be taken into account for the broadband portions.

6.1.4 Comparison to Optical & Radio Systems

Since the theoretical analysis of the system is founded in optics principles it is helpful to compare the THz imaging system to typical optical systems. This provides a reference by which the theory can be judged appropriate for the task. It also allows better understanding of the approximations that go into the theory and their effects. Additionally, a comparison to radio frequency systems is presented to help tie some concepts together and show that *all* apertured systems, regardless of frequency, operate by the same principles.

Consider the imaging of a point source using the THz imaging system. Since the system is configured for one-to-one imaging, the image produced by the system is really nothing more than a diffraction-limited *focus* of the spherical mirror. Therefore, the THz imaging system can be considered a focusing system in this configuration. Consider also the size of the optical components with respect to the wavelengths employed. At 1 THz, the diameter of the spherical mirror is about 500 wavelengths and distance from the object to the mirror (and from the mirror to the focus) is about 2000 wavelengths. For an

optical system, having the same proportions and operating with green light ($\lambda \approx 530$ nm), the mirror would be only 270 μm in diameter and the object would be only about 1 mm from the mirror. Such a system is not common so we might not expect it to behave as a typical optical focusing system. To investigate this, it is useful to introduce the *Fresnel number*, N , which quantifies the interrelationships among mirror size, wavelength, and focal distance. It is defined as

$$N = \frac{a^2}{\lambda f_d}, \quad (6-4)$$

where a is the mirror radius, λ is the wavelength, and f_d is the distance from the mirror to the focus. It turns out that systems of high Fresnel number ($N \gg 1$) behave as typical optical systems but systems with low Fresnel number ($N \ll 1$) behave quite differently, specifically with respect to the location of the point of maximum intensity. Li and Wolf [51] give an excellent discussion of systems of varying Fresnel numbers, which shall be followed presently.

Consider a typical optical focusing system with $a = 1$ cm, $f_d = 5$ cm, and $\lambda = 500$ nm. According to equation 6-4, this system has $N = 4000$. For a wave converging from the mirror in this system, the point of maximum intensity is coincident with the geometric focus. On the other hand, both the THz imaging system and a proportionally similar optical system, have $N = 32$. In this case, the reduced Fresnel number is due to the fact that the extent of the mirror encompasses far fewer wavelengths. It is clear, therefore, that the Fresnel number of a system can be decreased by decreasing a , while keeping f_d and λ fixed. The effect of such action is to relatively flatten out the phase front over the aperture of the mirror. Therefore the Fresnel number

essentially quantifies the relative flatness of the phase front over the diffracting aperture. If a was continually decreased, until $N \ll 1$, the wave converging from the aperture would begin to appear more and more like a plane wave diffracting through a circular aperture. At the same time, the point of maximum intensity would shift closer and closer to the plane of the aperture and would no longer be coincident with the geometric focus. When N finally became small enough, this situation would be better compared to a parabolic dish antenna ($a \approx 1$ m, $f_d \rightarrow \infty$) operating at radio frequencies ($\lambda \approx 30$ m), than to a typical optical system. For the radio system and any other system where $N \ll 1$, the field distribution produced by the “focused” wave is the far-field (Airy) pattern and is described by standard Fraunhofer diffraction theory.

So we see that the THz system does not behave strictly optically, where typically $\lambda \ll a$ and $f_d > a$, nor does it behave like a radio wave antenna, where typically $\lambda \gg a$ and $f_d \gg a$. That is, neither $N \ll 1$ nor $N \gg 1$ holds true. Instead, the THz imaging system lies somewhere in between and care must be taken in using optical principles to describe the system.

Since the THz imaging system is broadband, it has a continuum of Fresnel numbers ranging from 0 to about 100. Reference [51] shows that deviation from typical optical behavior at the focal region would become significant for the THz system at Fresnel numbers less than 10. This indicates that optical principles will describe the system with reasonable accuracy down to about 0.3 THz, and with greater accuracy for higher frequencies. Moreover, the spectral portion of the THz pulse below 0.3 THz represents only a small portion of the overall pulse energy; further supporting the use of optical principles.

6.1.5 Diffraction Theory Foundation

To better understand the form of the diffraction calculations it is useful to understand the foundation of scalar diffraction theory. The theory is founded on Huygen's principle, which states that every point on a propagating wavefront serves as the source of *spherical* secondary wavelets, such that the wavefront at some later time is the envelope of these wavelets [24]. Further, these wavelets propagate at the same frequency and speed as the original wave [24]. Knowing this, it is easy to see that Huygen's wavelets can be mathematically expressed by free-space Green's functions, which represent diverging spherical waves. The next step in scalar, optical diffraction theory is to determine the interference patterns in some space due to a continuous distribution of wavelets within a finite aperture. We find that this is mathematically expressed as an integral over a finite, continuous distribution of Green's functions. As will be seen, this integral is present in all the models of the THz imaging system.

6.2 Debye Model

One of the classic methods of finding the three-dimensional field distribution in the region of a geometric focus is the Debye integral as shown in Born and Wolf [25, Sec. 8.8]. Following Born and Wolf, with the exception of very minor notation changes, the treatment begins by assuming a perfectly spherical wave converging from a circular aperture of radius a . The center of curvature of the spherical wave lies at point O , the geometric focus of the wave, as shown in Figure 6-2. The scalar field distribution $h(P)$ at a typical point P is solved using the Huygens-Fresnel principle,

$$h(P) = -\frac{j}{\lambda} \frac{A \exp(-jkf_d)}{f_d} \iint_W \frac{\exp(jks)}{s} dS_W. \quad (6-5)$$

The Huygens wavelets are expressed in equation 6-5 by the free-space Green's function inside the integral. In this sense we see that the diffraction theory does little more than integrate the effects of a continuous distribution of wavelets over the surface of the finite, converging, spherical wavefront, W . Note that this form of the Huygens-Fresnel principle does not include the obliquity (or inclination) factor used to describe the varying strength of a Huygens wavelet as a function of angle. The point P is specified by position vector \mathbf{R} , relative to O . The variable s denotes the distance between some point Q on the converging wavefront W , and the observation point P . The variable \mathbf{q} denotes the unit vector in the direction of OQ . Assuming $a \gg \lambda$, $f_d \gg a$ and $f_d \gg |\mathbf{R}|$, we can approximate

$$s - f_d = -\mathbf{q} \cdot \mathbf{R}. \quad (6-6)$$

The differential wavefront surface over which the integral was specified, dS_W , can be expressed as

$$dS_W = f_d^2 d\Omega, \quad (6-7)$$

where $d\Omega$ is the solid angle differential element that dS_W subtends at O .

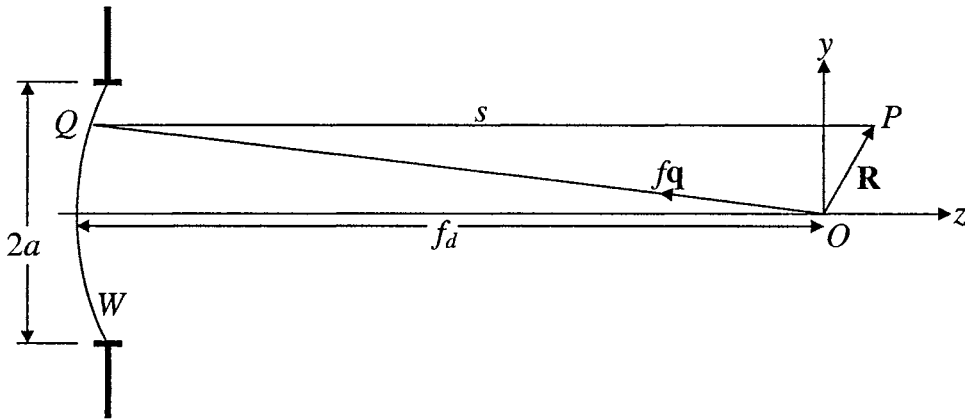


Figure 6-2. Debye model setup, diffraction of a converging spherical wave from a circular aperture.

Minor adjustments to amplitude terms do not affect the result appreciably therefore s can be replaced by f_d in the denominator of equation 6-5. After making all these substitutions, equation 6-5 becomes

$$h(P) = -\frac{j}{\lambda} A \iint_{\Omega} \exp(-jk\mathbf{q} \cdot \mathbf{R}) d\Omega. \quad (6-8)$$

This is called the Debye integral and expresses the field, h , as a superposition of plane waves of different directions of propagation [25, Sec. 8.8.1]. The variable h was used to represent the field in this instance because equation 6-8 also represents the monochromatic PSF, or spatial impulse response of the system. This notation was chosen to be consistent with the other models which will be presented later.

The THz system can actually be approximated quite well by this model. Consider the imaging system shown in Figure 6-3. The point source object, located at the center of curvature of a spherical mirror, O , emits a perfectly spherical, diverging wave in all directions. Some of the wave is intercepted by the spherical mirror and reflected. The remainder of the wave is essentially apertured out by not being reflected. Hence, the

reflection is a perfectly spherical wave converging from a circular aperture. The wave converges back to the center of curvature of the mirror, where it forms an image of the point source. Again, it is apparent that the focus of an apertured, converging, spherical wave *is* the image of the point source. This one-to-one imaging arrangement is very similar to the actual THz imaging system and differs only in that the THz system has an off-axis imaging arrangement in the x direction, such that neither the object nor the image are located at the center of curvature of the mirror.

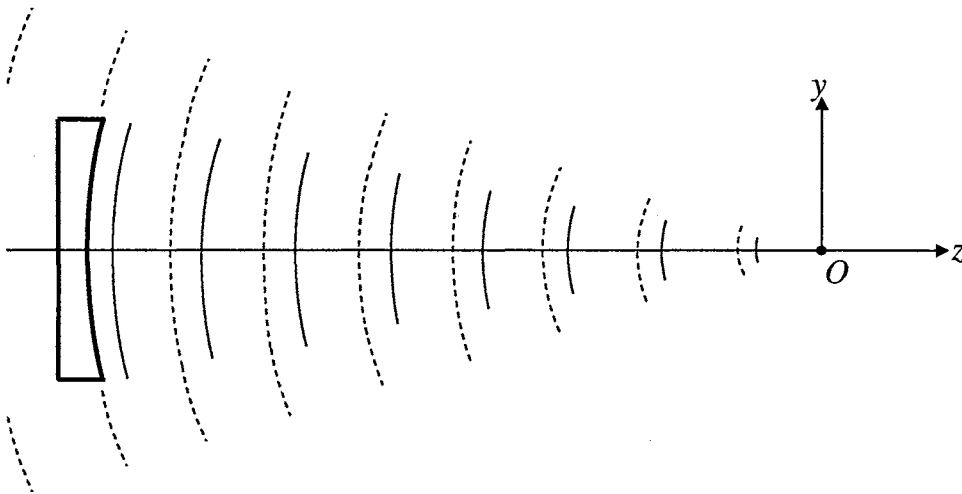


Figure 6-3. One-to-one imaging system producing perfectly spherical waves converging from a circular aperture (solid curves). Dashed curves indicate waves diverging from the point source.

6.2.1 Monochromatic Image

The analytic solution to the Debye integral can be expressed in terms of Lommel functions and is outlined in Born and Wolf [25, Sec. 8.8.1]. The solution represents the complex, scalar field distribution, which is a function of r and z only, due to the rotational symmetry of the system around the z -axis, where $r = \sqrt{x^2 + y^2}$. Figure 6-4 shows the

$y = 0$ slice of the three-dimensional focal region solution for a system with the same dimensions as the THz system, where $f_d = 610$ mm, $a = 76$ mm. The horizontal axis is labeled such that the value $z = 0$ corresponds to the geometric image plane of the mirror. This is a normalized field magnitude picture for the single frequency of 0.7 THz and is the image of a point source located at O in the system of Figure 6-3. Since the solution is rotationally symmetric about the z -axis, Figure 6-4 describes the entire three-dimensional focal region.

Figure 6-4 is not a field amplitude plot because the field is complex and the rapid phase variations obscure the overall focal structure. Plotting the field magnitude removes these variations and clarifies the structure but at the same time, produces unexpected contours, most notably around the field zeros. To clarify the contours of Figure 6-4, Figure 6-5 shows the field amplitude and magnitude patterns at $z = 0$.

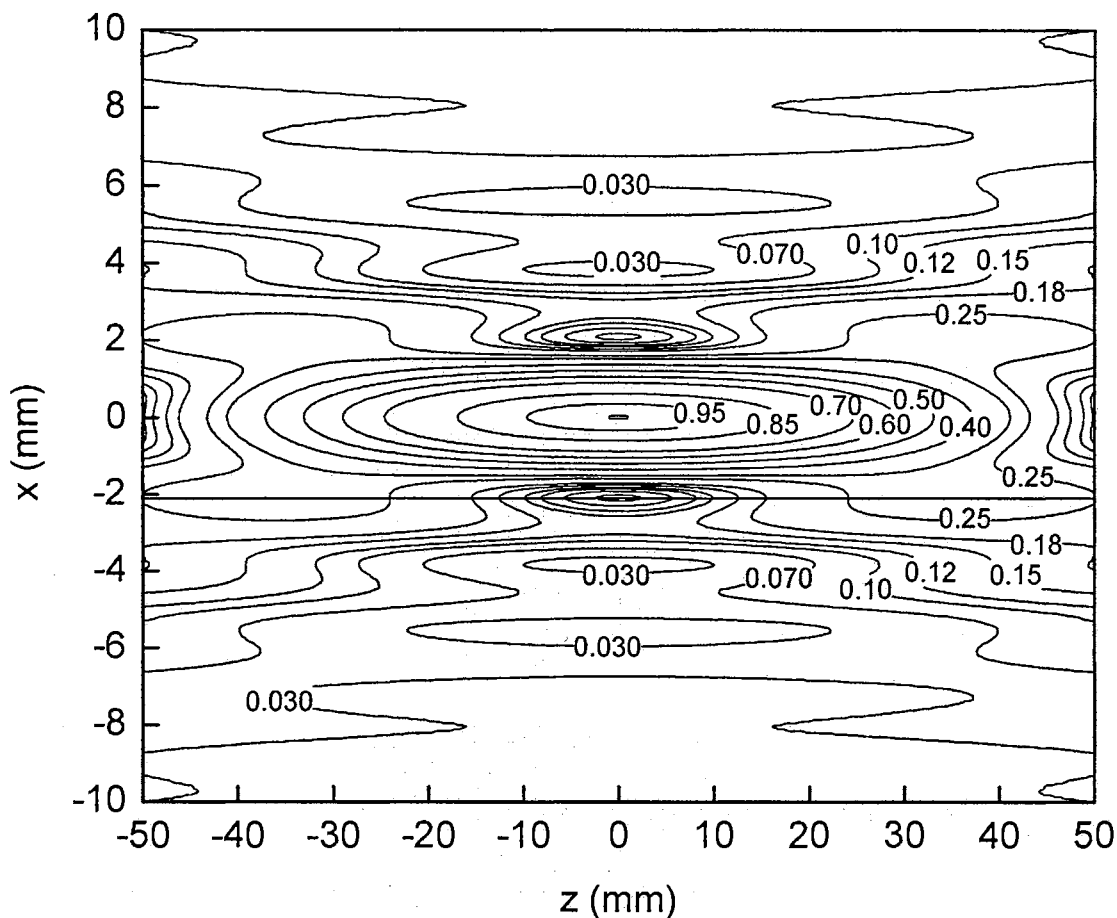


Figure 6-4. Normalized field magnitude image of a point source at 0.7 THz using the Debye integral. The geometric image plane is located $z = 0$. A horizontal line marks the position of the first field zero in the geometric image plane.

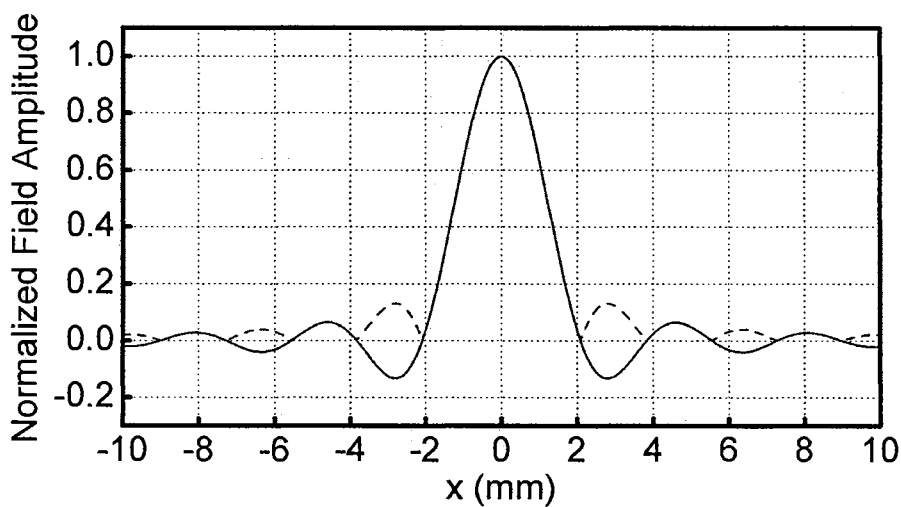


Figure 6-5. Normalized field amplitude (solid curve) at $z = 0$ of image of point source at 0.7 THz. Field magnitude is shown as dashed curve.

The most notable feature of Figure 6-4 is the elongated and tubular structure of the focus. This structure is common to focusing systems and accounts for the significant tolerance in positioning the image plane. The “length” of this tubular focus is inversely proportional to frequency. Therefore, at 0.7 THz this focal region maintains 95% of the field magnitude over a z -span of ± 10 mm, whereas at 2 THz this span would be reduced to about ± 3.5 mm. The figure also shows that the first field zero is at $x = \pm 2.1$ mm, in the geometric image plane ($z = 0$). Not coincidentally, this is exactly the distance from the peak to the first null of the Airy disk, calculated with the formula, $1.22 f_d \lambda / (2a)$. This is a consequence of the fact that the Debye integral generates the Fraunhofer, or far-field diffraction pattern at the focal plane of the spherical mirror.

6.2.2 Broadband Image

For any single frequency, the solution obtained by evaluation of equation 6-8 could theoretically be expressed in Cartesian coordinates as $U_i(x,y,z)$. This solution must be extended to account for the broadband nature of the THz imaging system and the resulting frequency-domain form is $U_i(x,y,z,\omega)$, a function of angular frequency, ω . The broadband, time-domain, THz pulse, $S(t)$, can also be expressed as a function of angular frequency by the Fourier transform,

$$S(\omega) = \int_{-\infty}^{\infty} S(t) \exp(j\omega t) dt, \quad (6-9)$$

This is a spatially independent, frequency-domain representation of $S(t)$. Since the Debye integral assumes that the wave converging from the aperture is uniform, there is no need

to specify the spatial dependence of the temporal signal. In other words, it is unnecessary to use the general form of the signal, $S(x,y,z,t)$, because it is constant over the wavefront.

Then, the imaging system can be thought of as a spatially dependent, temporal filter for the signal $S(t)$. Therefore, incorporating the frequency dependence into $h(P)$ gives $h(P,\omega) = h(x,y,z,\omega)$, which represents both the spatial impulse response and the temporal transfer function of the imaging system. By linear system theory, the frequency-domain representation of the amplitude image, $U_i(x,y,z,\omega)$, is

$$U_i(x, y, z, \omega) = S(\omega)h(x, y, z, \omega). \quad (6-10)$$

Applying the inverse Fourier transform to equation 6-10 we finally obtain the time-domain, broadband representation of the image,

$$U_i(x, y, z, t) = \frac{1}{2\pi} \int_{-\infty}^{\infty} S(\omega)h(x, y, z, \omega)\exp(-j\omega t)d\omega. \quad (6-11)$$

Equation 6-11 gives the final form of the time-domain, broadband PSF of the system, as calculated with the Debye model.

We notice here that equation 6-11 doesn't explicitly show the temporal effect of the pulsed illumination traveling from the mirror to the image plane. Since the imaging system is a temporal filter, it must account for the propagation time from the mirror to the image plane. Therefore, we might expect to see some retarded-time term in the final solution, which, in the frequency domain would manifest itself as a phase term of the form

$$\exp\left(j\omega\frac{s}{c}\right), \quad (6-12)$$

where s retains its previous definition. There is a simple reason why this term is not visible in equation 6-11. In the transformation from equation 6-5 to equation 6-8 all the phase accumulated by the converging wave as it traveled from the mirror to the origin is taken into account but given a new reference. The new phase reference for the calculation shifts from the wavefront (at the mirror) to the origin. This is true for all frequencies. Therefore the entire spectrum is now locked to a constant phase reference; which is the origin, where all the frequencies have the *same* phase. In equation 6-5 the calculation essentially begins at the wavefront and ends in the vicinity of the origin. In equation 6-8, the calculation begins at the origin and ends in the vicinity of the origin, so the retarded-time term never appears when the calculation is extended to the broadband pulse. In essence, both phase and time have simply been reset, or shifted, such that the retarded-time term is no longer present.

At the same time, the relative phase relationships between the spectral components of the pulse are maintained in its Fourier transform. Therefore, multiplying the Debye integral solution $h(x,y,z,\omega)$ by the complex pulse spectrum $S(\omega)$ applies the appropriate phase shifts, determined by the pulse, to the spatial field distribution. In this way, the solution in equation 6-11 generates both the proper phase relationship between spectral components and the proper spatial field distribution, even though the retarded-time term is not present. Since the system is time-invariant, these time shifts (or equivalently linear phase shifts) do nothing but change when the image appears, not what it looks like when it gets there.

Figure 6-6 shows the time-domain amplitude image in the geometric image plane (located 610 mm from the mirror), calculated using equation 6-11. Figure 6-7 shows two

other views of this image. To illustrate the tolerance in the z -position of the image plane, Figures 6-8 and 6-9 show the time-domain image calculated at a plane located 6 mm farther from the spherical mirror than the geometric image plane. For comparison, the time axes for all these figures have the same zero reference. As expected, the pulsed image appears in the shifted image plane about 20 ps later than it appeared in the geometric image plane, where $20 \text{ ps} = (6 \text{ mm})/c$.

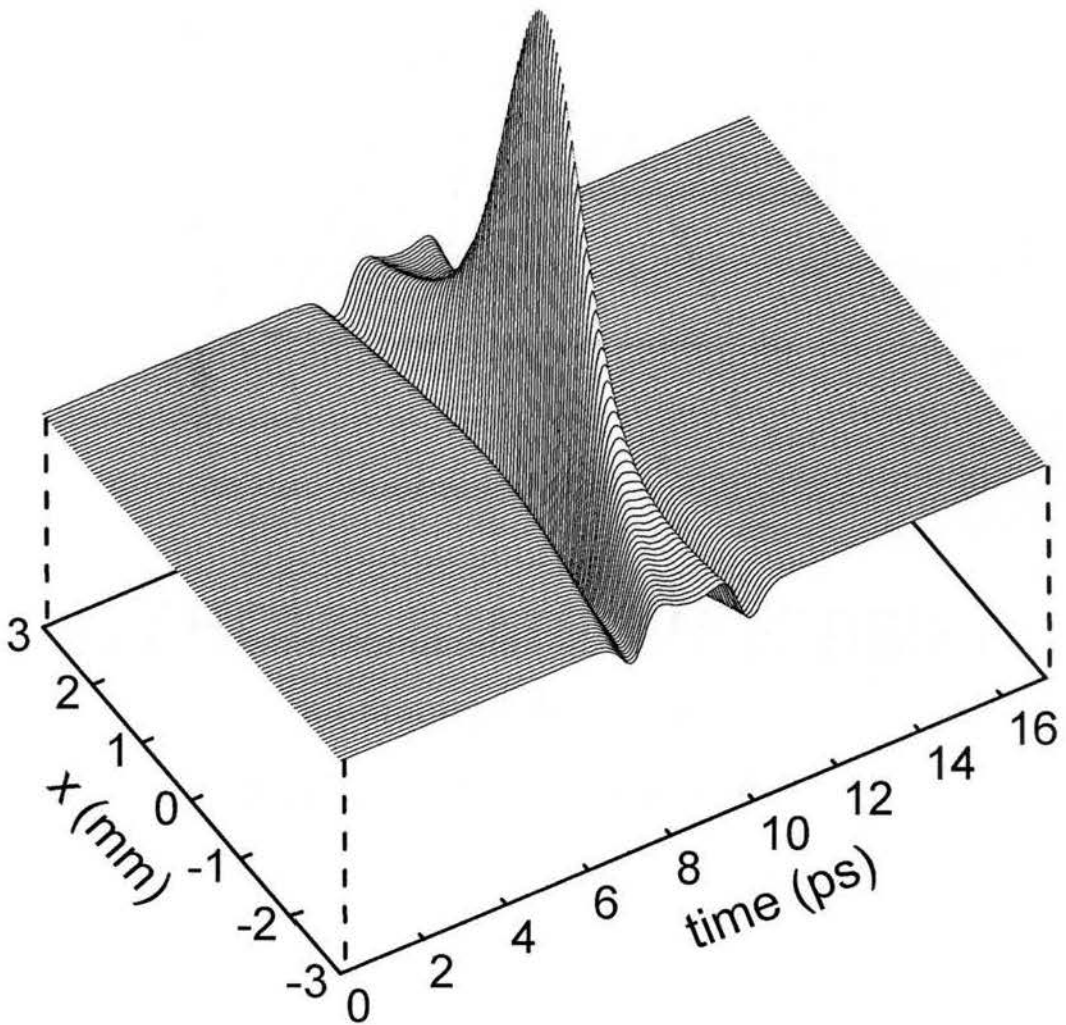


Figure 6-6. Normalized broadband amplitude image of point source in geometric image plane using Debye model. Plot consists of a set of contours corresponding to constant values in x .

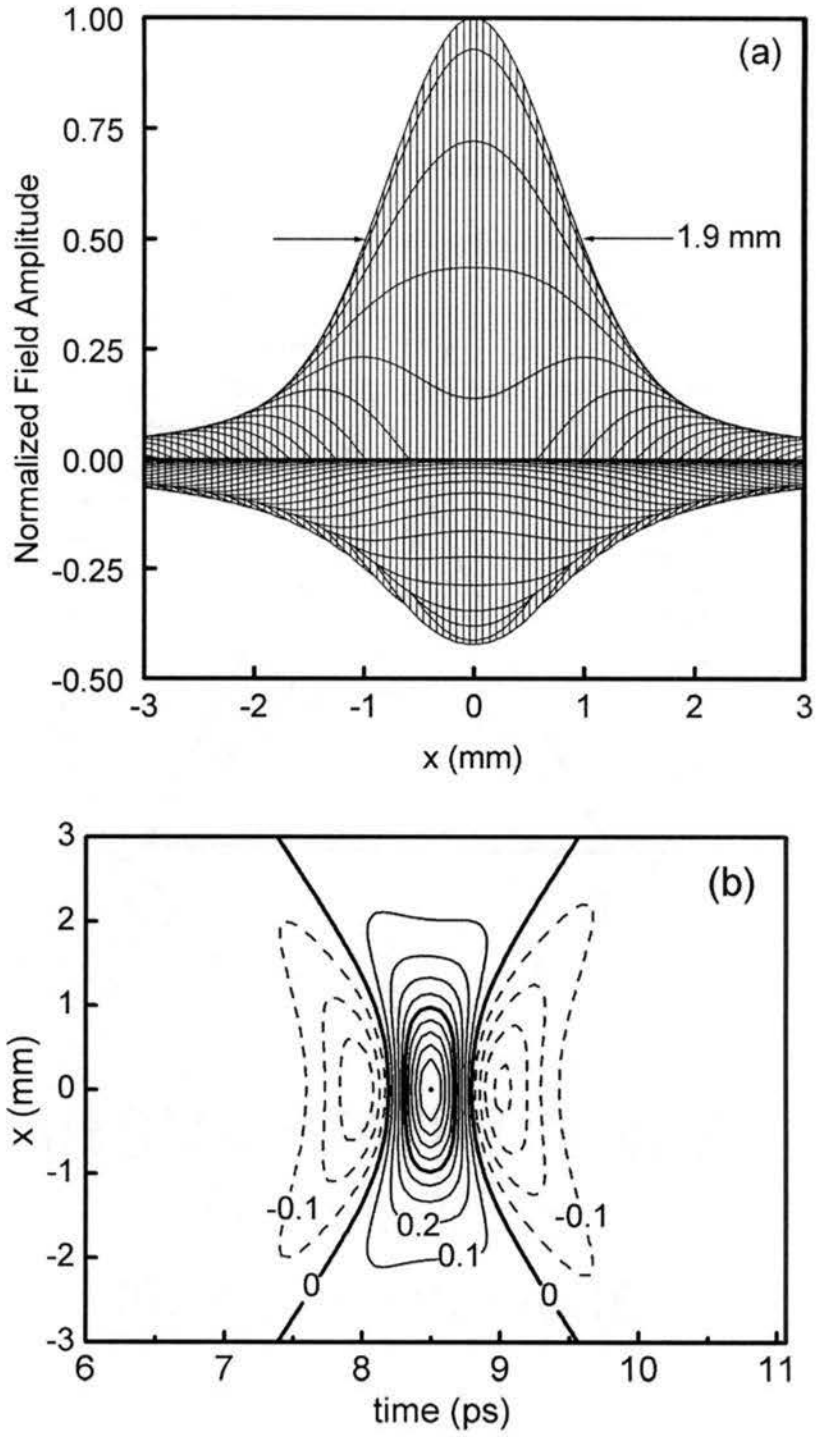


Figure 6-7. (a) Side view of Figure 6-6 consisting of contours constant in x and y . (b) Contour plan view of Figure 6-6, contour spacing is 0.1, negative contours are dashed curves, heavy contours indicate 0 and 0.5 values. The peak value of unity is designated by the dot.

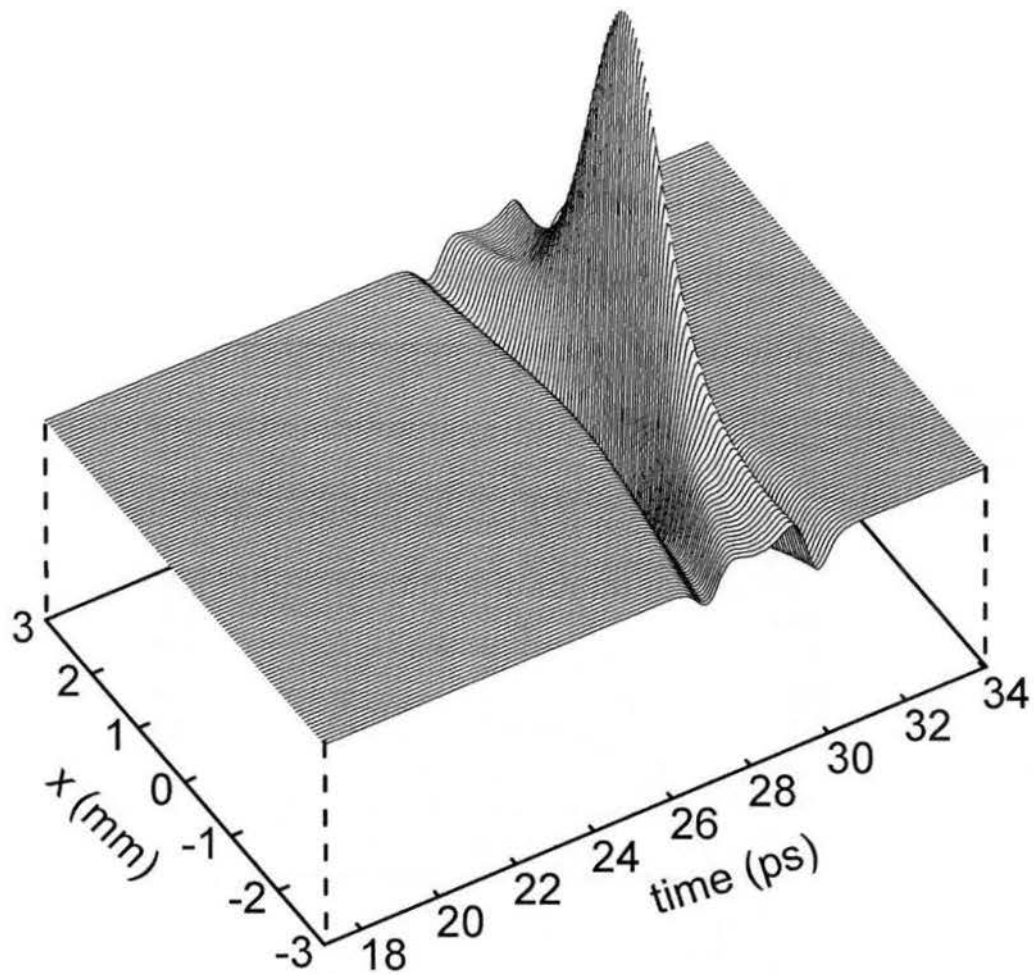


Figure 6-8. Broadband amplitude image of point source in a plane shifted 6 mm from geometric image plane. Plot consists of a set of contours corresponding to constant values in x . Amplitude has same scale as Figure 6-6.

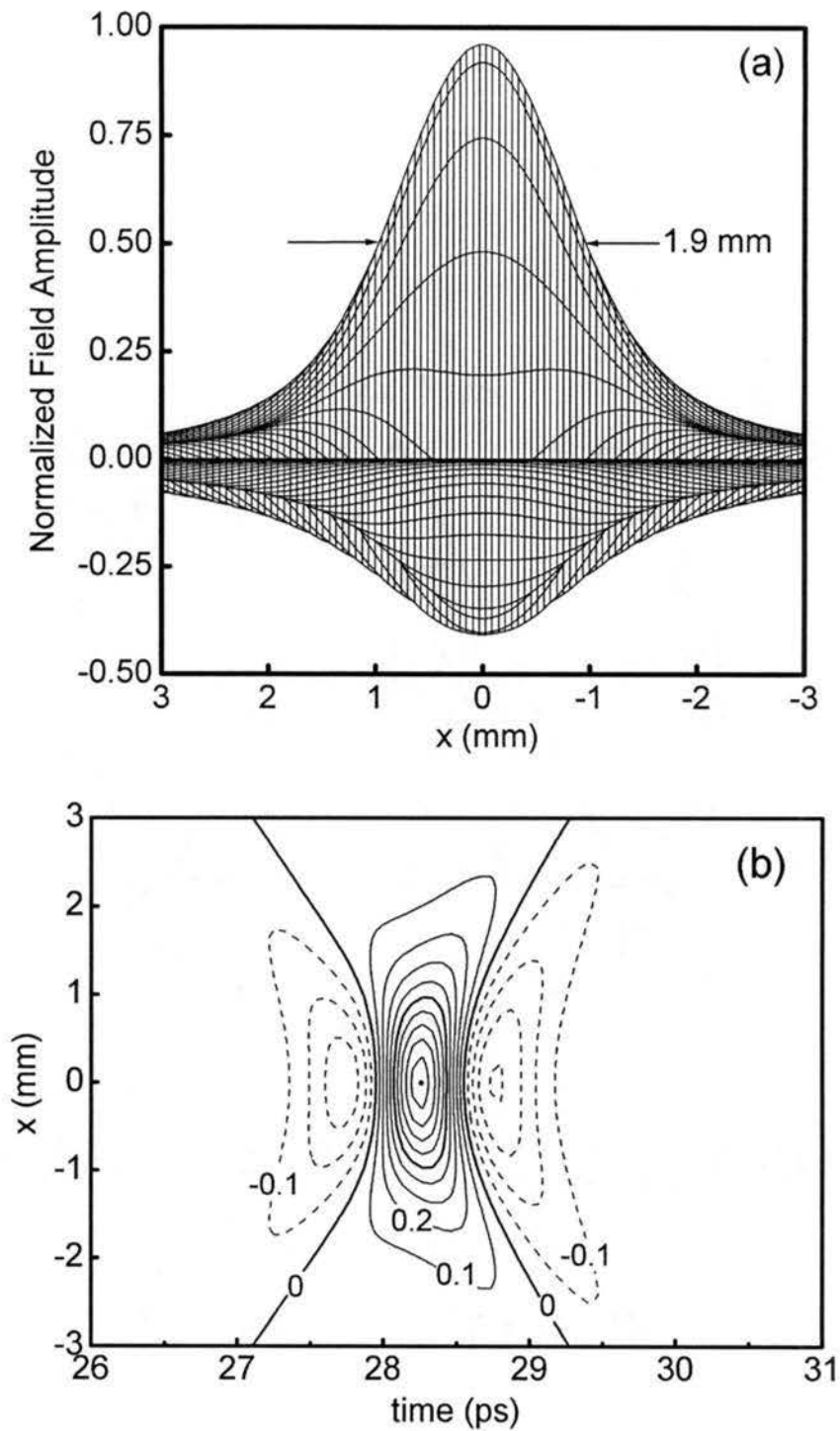


Figure 6-9. Broadband image of point source in 6 mm shifted image plane. (a) plot consists of set of contours corresponding to constant values in x . (b) negative contours indicated by dotted lines, contour spacing is 0.1, heavy contours indicate 0 and 0.5 values. Amplitude has same scale as Figure 6-7. The peak value of 0.96 is designated by the dot.

Figures 6-6 through 6-9 show why care must be taken in expressing the image $U_i(x,y,z,t)$ equivalently as either $U_i(x,y,z)$ or $U_i(x,y,t)$ as discussed in section 2.2. Changing the position of the image plane caused a minor change in the shape of the broadband image indicating that, t and z are not linearly dependent and they cannot strictly be expressed as functions of the other. This seems like it would be especially true in the immediate region of the focus where one might expect the field variation to be rather rapid. However, the elongated tubular structure of the focus provides a significant tolerance in z over as much as ± 10 mm around the geometric image plane. Furthermore, the temporal span of a THz image covers only about 17 ps, which translates into only 2.55 mm of pulse travel. Therefore, it is valid to assume that a typical THz image recorded in the geometric image plane would essentially be a time-shifted version of the image recorded in some other nearby plane. In this way, t and z can be considered linearly dependent.

6.2.3 Comparison

Figure 6-10 shows a side view comparison between the actual image data from Figure 4-4 and the theory from Figure 6-7. The angled orientation of actual images due to the illumination angle is not present in the theory but doesn't appear in the side view regardless. It is also noted that the theory doesn't account for the profile of the illumination beam, mentioned in section 4.1.1. Nevertheless, the figure clearly shows that the agreement between the theory and data is quite good.

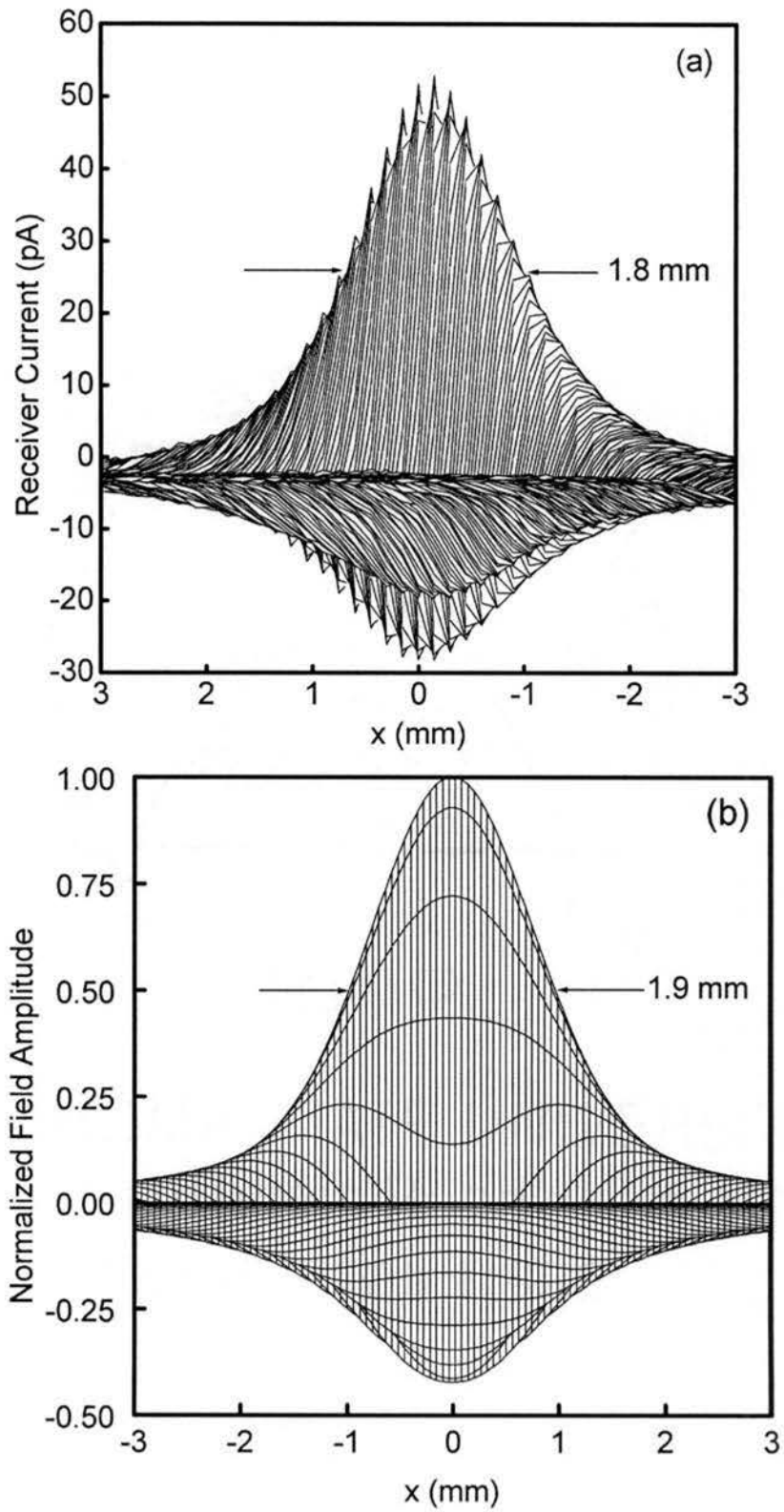


Figure 6-10. Comparison between (a) data from Fig. 4-4 and (b) theory from Fig. 6-7.

One difference is apparent in the negative amplitude portions of the images. In the actual data there appears to be an initial negative peak followed by a larger negative peak behind (later in time). In the theoretical image these negative peaks have the same magnitude. This is due to a minor reshaping of the THz pulse by a constant phase term in the spectrum and could easily be accounted for in the theory by multiplying the THz spectrum by this phase term. This is the same type of phase shift that was included in the input pulse to offset a $-j$ coefficient (see section 6.1.1). The minor correction was purposefully not included in the theory to bring out the point that such reshaping can change relative magnitudes of the positive and negative portions of the amplitude image. Under certain circumstances, such as with dielectric objects or small objects in very close proximity (under the range resolution limit), this could change overall image appearance by causing features to interfere differently. In fact, such effects could cause features to disappear from the image. This is another coherent resolution effect like the one mentioned in section 4.2, and could be described as a form of the speckle effect found in many coherent imaging systems [23 Sec. 6.5.3]. Due to the short duration of the THz pulse and the accompanying ranging behavior, the speckle effect is generally not as noticeable as it is in other systems.

The THz pulse reshaping effect can also change the way in which image data is processed. For example, it may be difficult to filter the image by applying a peak-picking algorithm (as in the image of the two 391 μm balls in section 5.7.1), because such a reshaping might cause peak identification problems. This effect was not a problem for the THz imaging system due to the relatively symmetric form of the received pulse.

6.2.4 Debye Approximations

Like the physical-optics (Kirchoff) approximation, the Debye integral prescribes some method by which the edge effects of the aperture are handled. The Kirchoff boundary conditions imply that the field and its normal derivative inside the aperture in a plane immediately behind the screen are assumed to be equal to the values they would have if the screen were not present and assumed to vanish at points outside the aperture in the same plane. In contrast, the Debye approximation assumes that the angular-spectrum of the incident field, not the field itself, is abruptly cut off by the edge of the aperture [26]. The notable effect is that the calculated focal region always appears symmetric on either side of the geometric image plane. Such an assumption is not valid when the Fresnel number, N , of the system is low. The Debye integral can be expected to return good results if $N \gg 1$, where again,

$$N = \frac{a^2}{f_d \lambda}, \quad (6-13)$$

and if $f_d \gg a \gg \lambda$ [25,51]. Based on the calculated images, the Debye integral seems to be fairly well suited for the THz system.

Wolf and Li provide a theoretical fix to the focal region reshaping in systems with low Fresnel numbers [51], but the Debye model has other problems. One problem, in particular, is that in using the Debye integral to model the THz imaging system, it is impossible to remove the object from the origin. This makes strict modeling of any object other than a point source at the origin impossible. The theory always assumes a perfectly spherical wave converging to a single spot on the optical axis. Any offset of the point source from the axis of the mirror would result in the converging wavefront

deviating from perfect sphericity. Such an effect could be ignored if the system was assumed to be space-invariant. To ensure that the space-invariance assumption was valid, however, other models were pursued.

6.3 Goodman Model

Goodman [23 Sec. 5.1-5.3] provides a simple example of a one-to-one imaging system which models the THz system quite well. This is more general than the Debye model because it allows the source to be moved slightly from the system optical axis. In Goodman, the physical system is modeled by a point source in some object plane, a single optic, and an image plane, as shown in Figure 6-11. Goodman's notation is followed closely except for the swap of variables specifying the xy -dependencies in the object and lens planes. To maintain consistency with the previous definitions used in this dissertation the object and lens planes are assigned the variables (x,y) and (ξ,η) , respectively. These are reversed in Goodman. Also, Γ is used to specify the image plane whereas U_i is reserved for the scalar image field within that plane.

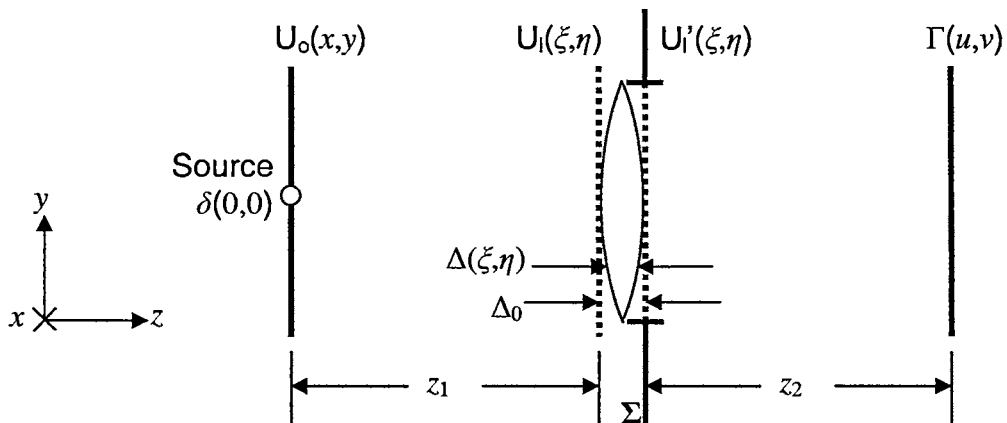


Figure 6-11. Goodman model, one-to-one imaging system with a point source.

The mirror of the THz imaging system is modeled by a lens lying between planes U_1 and U_1' . This is valid since both mirrors and lenses are similar phase transformers. The point source, δ , is located in the object plane U_0 at $x = 0$ and $y = 0$. To match the THz system, z_1 and z_2 must be equal and the entire optical path length from the source to the image plane Γ must be 1.220 meters, including both the thickness, Δ_0 , of the lens and the effects of its index. Since the lens will be approximated as a thin-lens later in the analysis, its effect can be summarized by simply specifying its focal length, f_L , to be 305 mm. Then z_1 and z_2 are specified as 610 mm.

The analysis of this system starts from the assumption of a monochromatic, spherical wave diverging from the point source. It is incident upon the lens, which acts as the most limiting aperture, or exit pupil, in the system, and also transforms the diverging wave into a converging spherical wave by the phase function $\Delta(\xi, \eta)$. The resulting field distribution in plane U_1' is used in the First Rayleigh-Sommerfeld diffraction integral to determine the field on the image plane. Specifically,

$$U_i(u, v) = \frac{z_2}{j\lambda} \iint_{\Sigma} U_1'(\xi, \eta) \frac{\exp(jkr_{01})}{r_{01}^2} d\xi d\eta, \quad (6-14)$$

where r_{01} is the distance between some observation point (u, v) and some differential area $d\xi d\eta$ lying in U_1' , within the pupil at point (ξ, η) . Again, the free-space Green's function appears in the integral, this time multiplied by the complex field at the output plane of the lens, $U_1'(\xi, \eta)$. If $U_1'(\xi, \eta)$ is assumed to be a converging spherical wave and $z_2 \approx r_{01}$, then equation 6-14 is almost exactly the same as equation 6-5, thus showing the consistency between the Goodman and Debye approaches.

Many features of this analysis depend on the calculation of the distance between two points in three-dimensional space. And, the system has many spherically shaped features, such as the wavefronts and lens faces, between which these distances are calculated. So it is common to see terms similar to

$$r_{01} = \sqrt{z_2^2 + (u - \xi)^2 + (v - \eta)^2} \quad (6-15)$$

throughout the analysis. To simplify these calculations, the binomial expansion,

$$\sqrt{1+b} \approx 1 + \frac{1}{2}b \quad (6-16)$$

permits the removal of most higher order terms. Equation 6-15 becomes

$$r_{01} \approx z_2 \left[1 + \frac{1}{2} \left(\frac{u - \xi}{z_2} \right)^2 + \frac{1}{2} \left(\frac{v - \eta}{z_2} \right)^2 \right] \quad (6-17)$$

and is valid only for paraxial rays. To simplify the calculation, this expression is substituted into the phase term, $\exp(jkr_{01})$, of equation 6-14. Similar approximations simplify the phase term of the diverging spherical wave from the source, and simplify the mathematical description of the lens faces. These expressions are embedded in the term $U_1'(\xi, \eta)$ in equation 6-14. The amplitude term, $1/r_{01}$ is not so critical in obtaining an accurate solution therefore it is approximated as $1/z_2$. Together, these amplitude and phase simplifications comprise the *Fresnel approximation*.

The expansion of equation 6-14, incorporating the diverging wave from the point source, the behavior of the lens, and the application of the Fresnel approximation throughout, collectively comprises the monochromatic PSF, $h(u, v; x, y)$. It is expressed as

$$\begin{aligned}
h(u, v; x, y) = & \frac{-j}{\lambda^2 z_1 z_2} \exp\left[j \frac{k}{2z_2} (u^2 + v^2)\right] \exp\left[j \frac{k}{2z_1} (x^2 + y^2)\right] \\
& \times \iint_{\Sigma} \exp\left[j \frac{k}{2} \left(\frac{1}{z_1} + \frac{1}{z_2} - \frac{1}{f_L}\right) (\xi^2 + \eta^2)\right] \\
& \times \exp\left\{-jk \left[\left(\frac{x}{z_1} + \frac{u}{z_2}\right) \xi + \left(\frac{y}{z_1} + \frac{v}{z_2}\right) \eta\right]\right\} d\xi d\eta.
\end{aligned} \tag{6-18}$$

The detailed procedure to arrive at equation 6-18 is given in [23, Sec 5.3.1]. Equation 6-18 is equivalently the general form of an image formed in the image plane Γ at some point (u, v) from a point source in the object plane U_o at point (x, y) . The double integration limits are bounded by the pupil, Σ , which in this case is just defined by the circular, transverse extent of the lens. Again, the variable f_L is the focal length of the lens as determined by a standard thin-lens treatment and, to model the THz imaging system, is $f_L = 305$ mm.

6.3.1 Monochromatic Image

The solution of Equation 6-18 must be solved numerically and represents the complex, scalar field distribution, which is a function of u and v only. The calculation can be performed for many values of z_2 to obtain the image of Figure 6-12, which shows the $v = 0$ slice through the three-dimensional, monochromatic focal region; equivalently the monochromatic image of a point source.

For this image, the source is located at $x = 0$ and $y = 0$ so the system has rotational symmetry and it is sufficient to show only the single slice to describe the entire focal region. To mimic the THz system, $z_1 = 610$ mm, $\Delta_0 = 0$ since the lens is assumed to be thin, Σ is bounded by $\sqrt{\xi^2 + \eta^2} \leq 76$ mm, and z_2 varies between 560 mm and 660 mm.

In the figure, the horizontal axis is labeled such that the value $z = 0$ corresponds to the geometric image plane, Γ , located at $z_2 = 610$ mm. Figure 6-12 is a normalized field magnitude image for the single frequency of 0.7 THz.

As a point of clarification, we note that the imaging system has no magnification; so there is a one-to-one scale relationship between the variables (u,v) and (x,y) . Therefore, images produced by the Goodman model, which have a (u,v) dependence, can be directly compared to experimental images and images produced by the Debye model, which have a (x,y) dependence. Similarly, images produced by the hybrid model, which will be discussed in section 6.4, can also be directly compared to all the others.

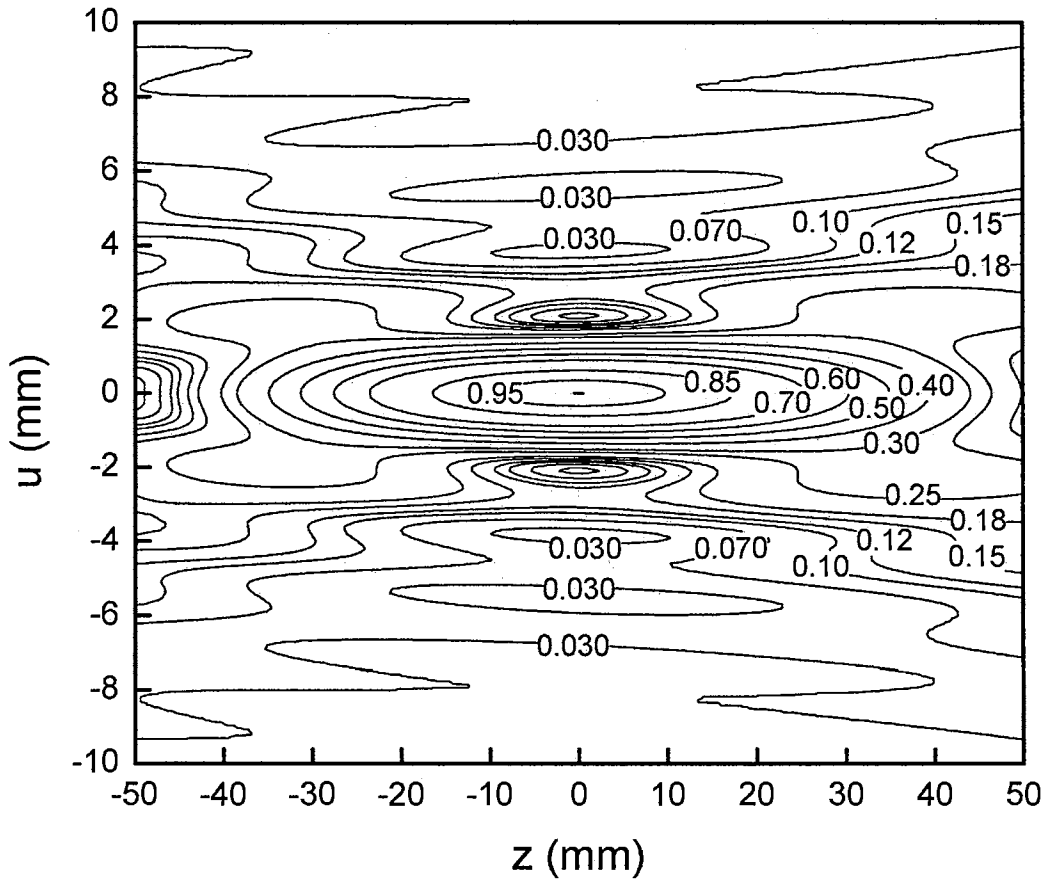


Figure 6-12. Normalized field magnitude image of a point source at 0.7 THz.

One of the first things to notice about Figure 6-12 is the absence of symmetry on either side of the geometric focal plane at $z = 0$. This non-linear “stretching” of the focal region indicates that Goodman’s approach automatically takes into account at least some of the effects of low Fresnel numbers. Other parts of the image are strikingly similar to that of the Debye treatment. The transverse width of the image is almost identical to that of the Debye treatment, especially at the geometric focal plane, and the general structure of the focal region is essentially unchanged. Further comparisons will be given in later sections after all three models have been discussed.

6.3.2 Broadband Image

Extending the solution of the Goodman model to account for the full THz spectrum is similar to that of the Debye model. But unlike the Debye model, the Goodman model is not re-expressed in terms of solid angles so it is possible to show the time-retarded phase term. To explicitly express equation 6-14 as a function of frequency, we can rewrite it as

$$U_i(u, v, \omega) = \frac{z_2}{j\lambda} \iint_{\Sigma} U_1(\xi, \eta, \omega) \frac{\exp\left(j \frac{\omega r_{01}}{c}\right)}{r_{01}^2} d\xi d\eta, \quad (6-19)$$

where the wavenumber, k , has been replaced using $k = \omega/c$. For the THz system analysis, the index of the medium is $n = 1$ therefore $k = \omega/c$. We can also express U_i in the time-domain via the inverse Fourier transform,

$$U_i(u, v, t) = \frac{1}{2\pi} \int_{-\infty}^{\infty} U_i(u, v, \omega) \exp(-j\omega t) d\omega. \quad (6-20)$$

Substituting equation 6-19 into equation 6-20 we get,

$$U_i(u, v, t) = \frac{1}{2\pi} \int_{-\infty}^{\infty} \frac{z_2}{j\lambda} \iint_{\Sigma} U'_1(\xi, \eta, \omega) \frac{\exp\left(j\frac{\omega r_{01}}{c}\right)}{r_{01}^2} \exp(-j\omega t) d\xi d\eta d\omega, \quad (6-21)$$

Rearranging terms yields

$$U_i(u, v, t) = \frac{1}{2\pi} \int_{-\infty}^{\infty} \frac{z_2}{j\lambda} \iint_{\Sigma} U'_1(\xi, \eta, \omega) \frac{\exp\left(-j\omega\left(t - \frac{r_{01}}{c}\right)\right)}{r_{01}^2} d\xi d\eta d\omega. \quad (6-22)$$

Equation 6-22 includes the expected retarded-time term, $\exp[-j\omega(t - r_{01}/c)]$, accounting for the time it takes for the waves to propagate from the output of the lens to the image plane.

Up to the exit pupil, only ray tracing is used to keep track of the phase behavior of the system. Therefore $U'_1(\xi, \eta, \omega)$ is nothing more than the spectrum of a delayed version of the original source pulse, $S(t)$, where the delay, Φ , is a function of spatial location (ξ, η) . Hence, it can be expressed as

$$U'_1(\xi, \eta, \omega) = \int_{-\infty}^{\infty} S(t - \Phi(\xi, \eta)) \exp(j\omega t) dt, \quad (6-23)$$

where $\Phi(\xi, \eta)$ is the time-delay of the original pulse, S , at location (ξ, η) . Knowing this we can see that equation 6-22 is the inverse Fourier transform of the product of the spatial field distribution and the time-shifted, complex spectrum of the broadband pulse. However, we also recognize that the solution of equation 6-18 already accounts for all the spatially varying phase delays, $\Phi(x, y)$, encountered by $S(t)$ throughout the entire system. Therefore the total time-domain solution, can be simplified to

$$U_i(u, v, t) = \frac{1}{2\pi} \int_{-\infty}^{\infty} S(\omega)h(\omega)\exp(-j\omega t)d\omega, \quad [6-24]$$

where $S(\omega)$ is the complex pulse spectrum and $h(\omega)$ is the PSF of equation 6-18 calculated at all the frequencies, ω , in the bandwidth of the source pulse. Equation 6-24 gives the final time-domain form of the broadband PSF in the Goodman treatment. Clearly this solution is very similar to the Debye treatment, shown in equation 6-11, with a few exceptions; such as the choice of diffraction integral.

Like the Debye treatment, the solution is time-invariant so that $t = 0$ can be shifted anywhere to easier display the data. Figure 6-13 shows the time-domain image in the geometric focal plane, calculated using equation 6-24. Figure 6-14 shows two other views of this image.

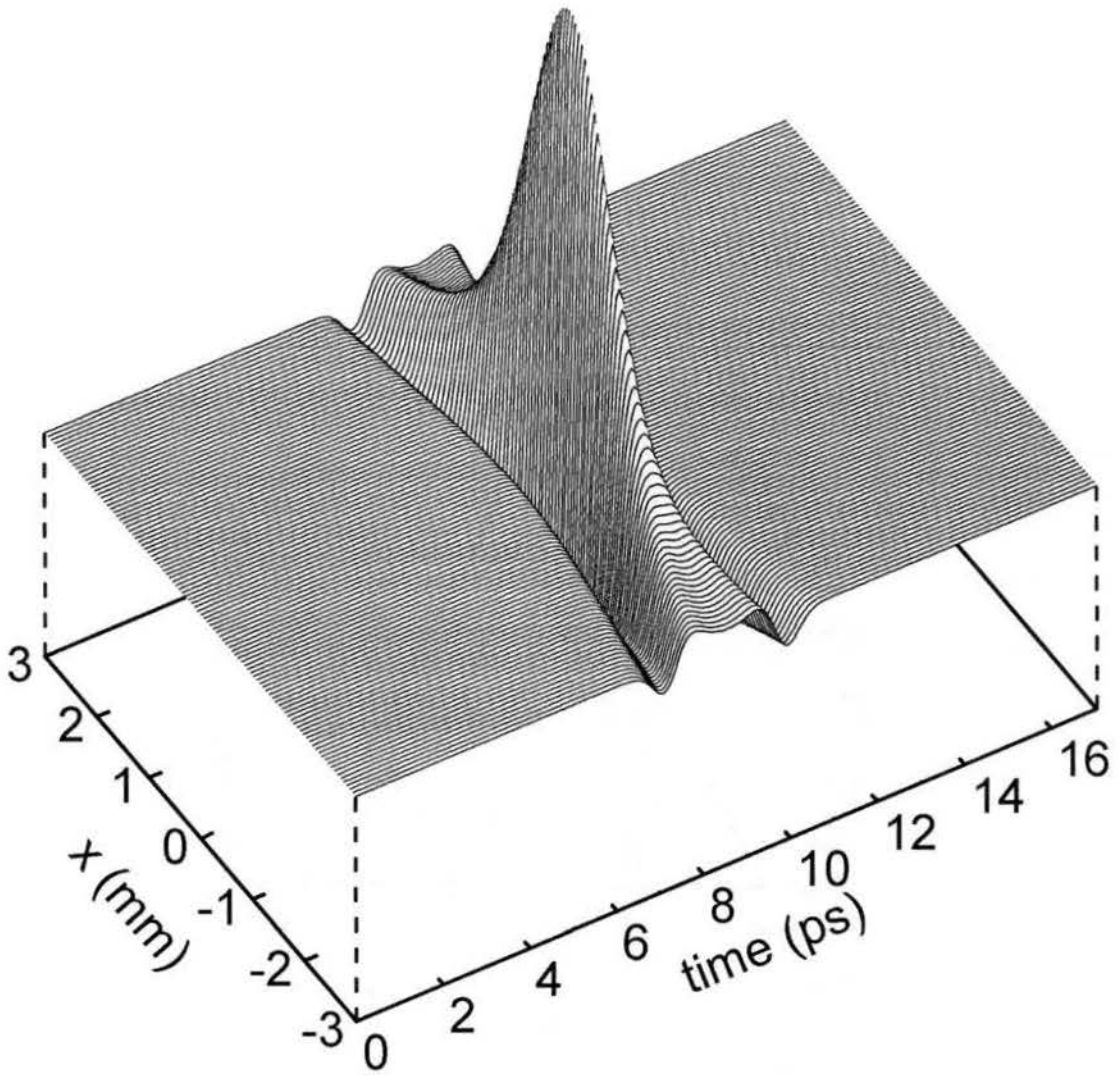


Figure 6-13. Normalized broadband image of point source in geometric image plane. Plot consists of a set of contours corresponding to constant values in x .

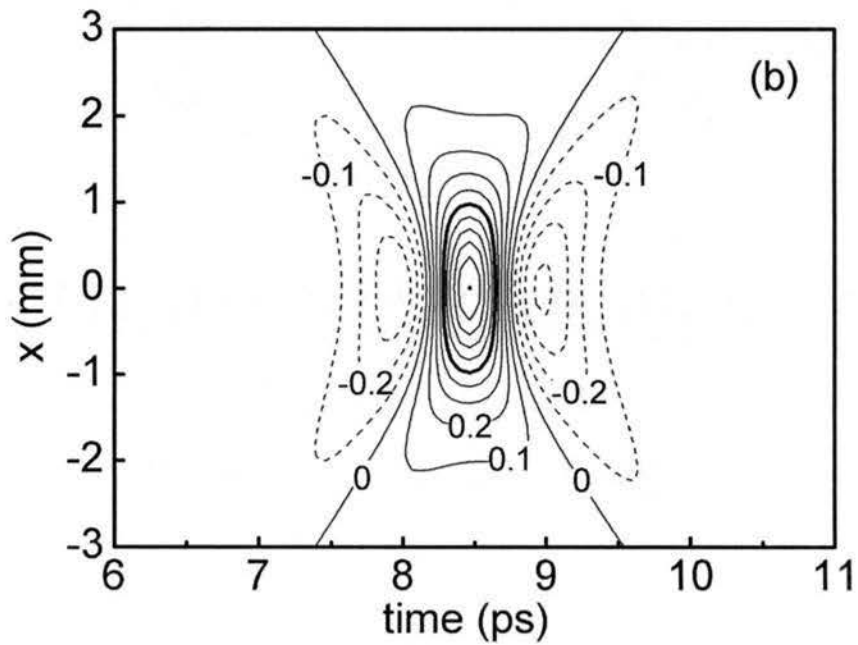
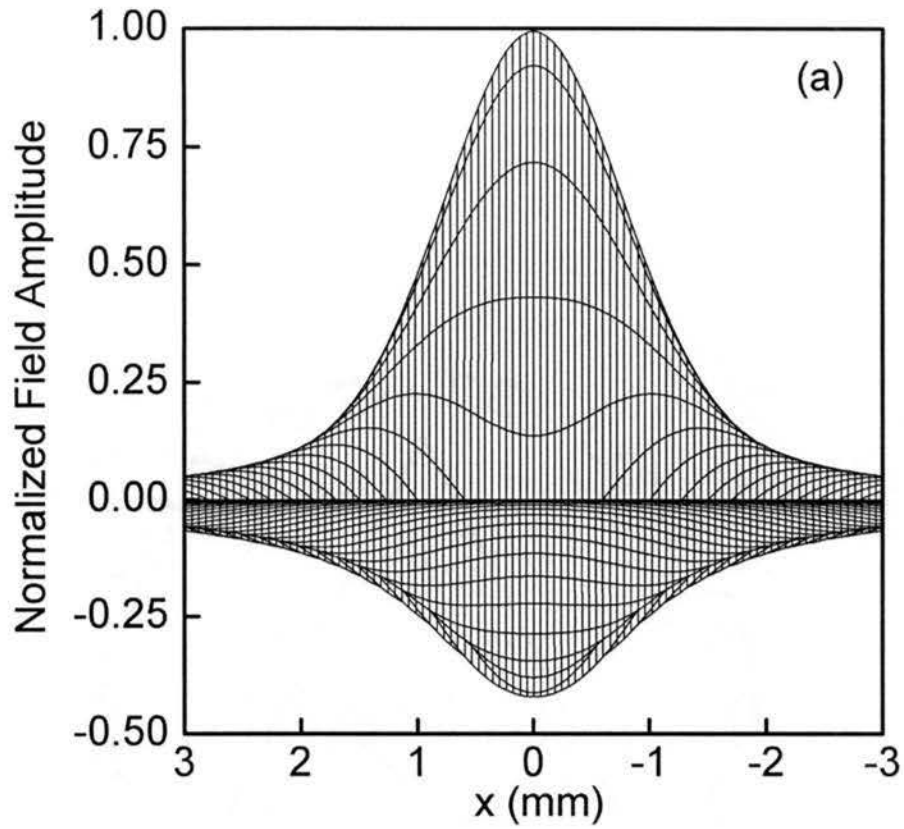


Figure 6-14. (a) Side view of Figure 6-13 consisting of contours constant in x and y . (b) Contour plan view of Figure 6-13, contour spacing is 0.1, negative contours are denoted by dashed curves, heavy contour indicates 0.5 value. The peak value of unity is designated by the dot.

6.3.3 Comparison

Figures 6-13 and 6-14 are almost identical with the figures generated by the Debye treatment (Figs. 6-6 and 6-7). The side-by-side comparisons of the Debye and Goodman model results will be presented after all three models have been discussed. For now it is sufficient to say that the match between actual data and the Goodman model is very good, as it was in the Debye model. Clearly, both approaches work well for describing the THz imaging system, but the Goodman model has more flexibility. The lack of symmetry in the monochromatic field pattern on either side of the geometric image plane obtained by the Rayleigh-Sommerfeld diffraction integral doesn't seem too noticeable due to fact that overall image is the superposition of all the frequencies of the THz pulse. Since this symmetry issue would only be significant at low frequencies its effect is muted in the broadband image.

6.3.4 Approximations

The First Rayleigh-Sommerfeld integral involves the use of a modified version of the Kirchoff boundary conditions to account for the effects of the edge of the aperture. Specifically, the Kirchoff boundary condition is applied to the field alone, not its derivative. Also, as in most scalar diffraction treatments, it was assumed that the radius of the aperture and the distance from the aperture to the observation plane were both much larger than a wavelength.

6.4 Hybrid Rayleigh-Sommerfeld Model

Though it was not presented, it was possible to obtain the theoretical image for something other than a point source at the origin by using the Goodman model. This made the Goodman model more versatile than the Debye model. However, it was still rich in approximations and not really designed for off-axis systems. To account for the off-axis geometric aberrations in the system, particularly astigmatism, a hybrid model was formulated, having the same layout and dimensions of the THz system.

The Debye and Goodman models had the advantage of neglecting the complex diffraction treatment of aberrations and this omission greatly simplified calculations. In [25], Born and Wolf devote all of chapter 9 to the diffraction theory of aberrations; but this theory is very complex and not readily adaptable to a real imaging system wherein many aberrations occur at once. The hybrid theory accounts for aberrations by using a geometric optics analysis up to a specific plane within the system. At this point, diffraction theory accounts for the remainder of the analysis. The calculations are performed numerically with the end goal being the simple computation of the image, not the any analytic expression for it. Simple diffraction integrals for THz systems are not a significant challenge to computers with standard math software, so this hybrid method takes advantage of computing speed to formulate an image without the use of overly difficult mathematical methods.

6.4.1 Calculation Duration & Precision

Even though computing speed is available to quickly perform multiple diffraction calculations for the THz imaging system, the same is not universally true for any system. Numerical calculations require a discrete representation of the waves and diffraction integrals. For a given system, the phase of a wave over the diffraction aperture varies much more slowly for THz frequencies than for optical frequencies, so far fewer points (or a sparser grid) can be used to accurately represent the wave. Therefore, far fewer points need to be integrated over and the duration of the calculation is drastically reduced. In this respect it is clear that calculation duration can be directly related to the Fresnel number of the system. For systems with large Fresnel numbers, such as typical optical systems, calculation times could be exceedingly long. Systems with equal Fresnel numbers should have nearly equal calculations times.

For reference, a typical, one-dimensional, broadband THz image in a single z-plane, like the one in section 6.3.2, takes less than 30 seconds to calculate for a 2.8 GHz Pentium 4 processor with 1 GB of memory. The upcoming calculations for the hybrid model are two-dimensional and therefore the calculation time is usually increased by a factor of about 60. For a typical two-dimensional, broadband THz image in a single z-plane, the calculation time is about 10-15 minutes. One can see that if the calculation for a typical optical system required 10 times the number of data points in each transverse dimension to represent the diffracting wave, then the calculation time would be increased by about 100 times, making such calculations very long and far less usable. In this respect we can see that the THz system has a significant advantage with respect to

calculation times, due to its relatively small Fresnel numbers.

For the THz system, a good trade-off between accuracy and speed was found if the calculations were performed with a bundle of rays that formed a spatial grid of 151×151 points over the face of the spherical mirror. Even though this grid density is not strictly sufficient to unambiguously map the phase distribution over the diffraction plane at higher frequencies (>1.5 THz), it was found to yield results with good accuracy in the aforementioned calculation times. To ensure the accuracy of these results, additional broadband calculations were performed with grids of 351×351 . This grid density provides over two data points per every oscillation of the phase distribution of the wavefront over the diffraction plane, up to approximately 2 THz. For lower frequencies, this condition is improved. It was found that calculations using the 151×151 grid size matched larger grid results very well. Additionally, since a very large portion of the THz bandwidth exists at lower frequencies centered around 0.7 THz, even smaller grid sizes, down to 51×51 , still produced similar broadband results.

One final issue of importance in the calculations was numerical precision. This problem represents a potentially significant obstacle when performing calculations with sub-mm wavelengths over distances exceeding half a meter. In such instances, numerical precision could possibly alter the phase of a wave enough to completely change its interference behavior at the image plane. Fortunately, this is not the case for the THz system. Consider the shortest wavelength used by the THz system, approximately $125 \mu\text{m}$. For phase precision to $1/10^{\text{th}}$ a wavelength, calculations over 600 mm must be accurate to about one part in 50,000. This is clearly no challenge for math software, even when operating in single precision mode where 23 mantissa bits are available for

precision to about 7 decimal places, or one part in 10,000,000. This indicates that even optical images could be calculated with almost $\lambda/10$ phase precision in the same system. Moreover, the math software used in the THz calculations (MATLAB[®] Version 6.1) [52] performed operations in double precision mode, thereby alleviating any concern for numerical precision.

6.4.2 Hybrid Model Setup

The hybrid model of the THz system begins with a point source located at point O with coordinates (x,y,z) as shown in Figure 6-15.

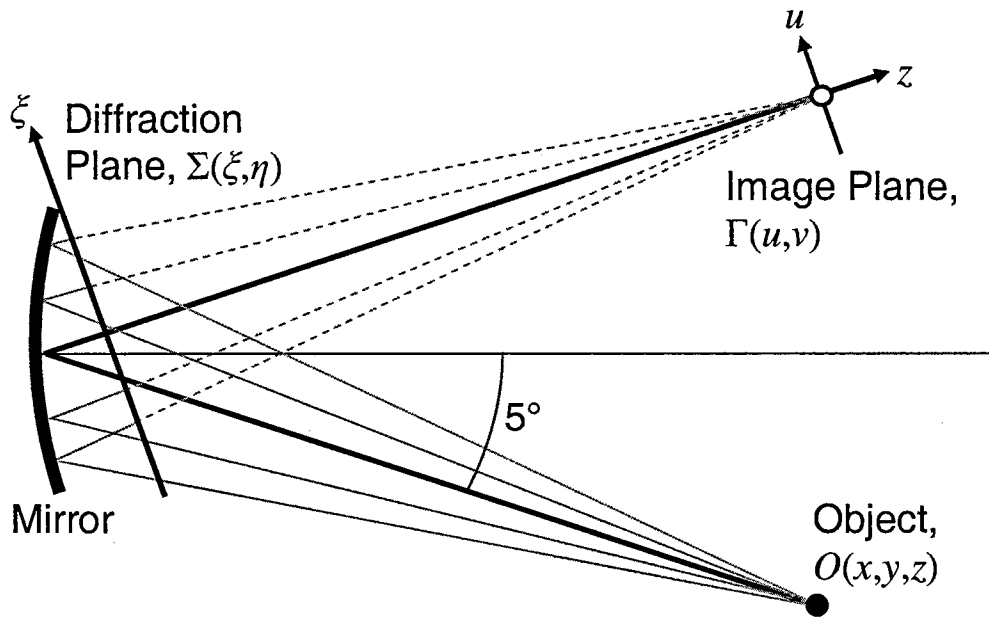


Figure 6-15. Layout of hybrid model of THz imaging system.

The object is assumed to be a point source emitting an isotropic, diverging spherical wave. This wave is represented in a geometric optics fashion by a bundle of rays (shown in Figure 6-15 as solid gray lines) propagating toward the spherical mirror.

Using the law of reflection from a metal surface the rays are reflected from the mirror and intersect with the diffraction plane, Σ . The location of each ray and the overall distance it has traveled when it intersects with Σ is then calculated with basic geometry. Knowing the distance traveled and the wavelength of the radiation provides a phase distribution over the plane Σ . Rays that never intersect the mirror are not reflected to the diffraction plane; therefore the extent of the spherical mirror is automatically projected onto the diffraction plane to define the exit pupil of the system. It is also noted that, due to the off-axis setup, the shape of the exit pupil is somewhat elliptical from the vantage of the axial image point. This is automatically taken into account by the ray tracing. Having treated the system with geometric optics, the calculated field distribution inside Σ already accounts for the relevant geometric aberrations.

All the rays from the source are assumed to have the same strength at the diffraction plane, Σ , therefore the entire field distribution is known therein. With this planar field distribution, the First Rayleigh-Sommerfeld diffraction integral (equation 6-14) is used to calculate the resulting field distribution in the image plane, Γ . Figure 6-16 shows the setup for this leg of the model. As in the Goodman model, the distance between the diffraction and image planes is z_2 , and the distance between the differential element $d\zeta d\eta$ and the observation point P is r_{01} . Integration takes place over the region of the diffraction plane bounded by the pupil.

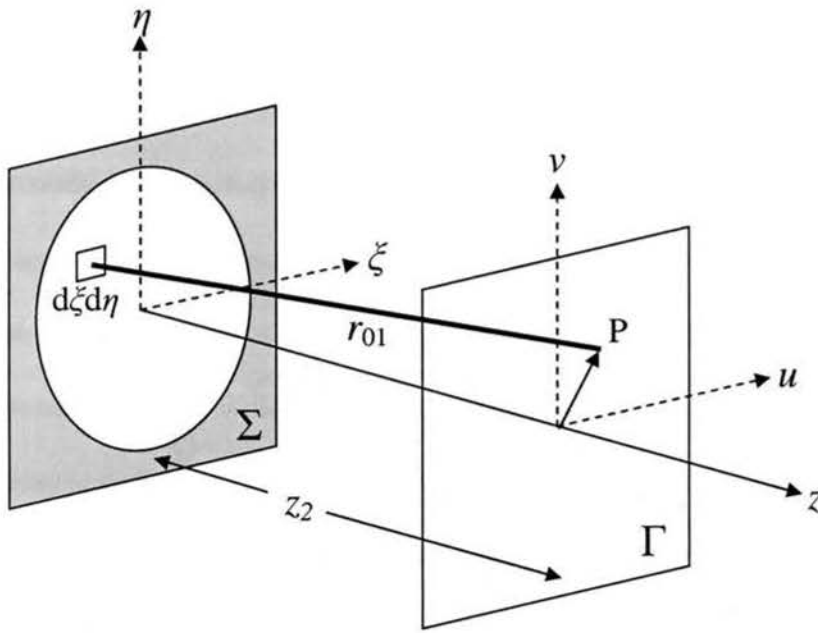


Figure 6-16. Setup for diffraction leg of hybrid model.

The model is designed to take advantage of computing power, so no further approximations are made to any of the phase terms or distances. For example, r_{01} is computed exactly as it is shown in equation 6-15.

6.4.3 Monochromatic Image

The monochromatic image is finally obtained by numerically integrating equation 6-14, where the field distribution in Σ , calculated by geometric optics, is substituted in for the term $U'_1(\xi, \eta)$. As before, the calculation can be performed for many values of z_2 to obtain the images of Figure 6-17, which shows the $u = 0$ mm and $v = 0$ mm slices through the three-dimensional image. With the inclusion of the off-axis layout, the system no longer has rotational symmetry and it is necessary to show the image in several slices to describe the entire focal region. To mimic the THz system, $z_2 = 598$ mm, and the pupil is

Like the Goodman treatment, the hybrid model images show a non-linear stretching of the focal region, which is present in systems of low Fresnel number. The general shape of the focal region is not too different from the other treatments and the focal region maintains its tubular shape and still has a similar overall structure. This indicates that there is still significant tolerance in positioning the image plane, though not as much as before. Nevertheless the focal region retains 95% of its peak value over a z -span of about ± 7 mm at 0.7 THz. The most striking feature of Figure 6-17 is the cylindrical asymmetry about the optical axis. The cause of this asymmetry is almost entirely astigmatism. This was expected since the astigmatism portion of the aberration function follows a square dependence on the off-axis imaging angle, whereas other aberrations follow a singular dependence at most. The astigmatism is easily visible by looking at transverse plots of the image. Figures 6-18 and 6-19 show several transverse contour plots of the three-dimensional image of a point source at 0.7 THz. Figure 6-19 shows the PSF in the geometric image plane for 0.7 THz.

As expected from geometric optics the primary image, also called the tangential line focus, is vertical in orientation and lies nearest to the spherical mirror. The secondary image, also called the sagittal line focus, is horizontal in orientation and lies farthest from the spherical mirror. Using geometric optics, the spatial separation between the tangential and sagittal foci can be found to be only about 9 mm. The specific locations of these foci are not easily identifiable in the images of Figure 6-17 because the effects of astigmatism are not nearly as significant as those of diffraction. Between these two foci lies the plane containing the circle of least confusion (COLC) wherein imaging

is most correct. Figure 6-19 shows the image in this plane. At 0.7 THz the image retains this shape quite well over a z -span of ± 5 mm from the plane containing the circle of least confusion. At 2 THz this span would be reduced to about ± 1.75 mm.

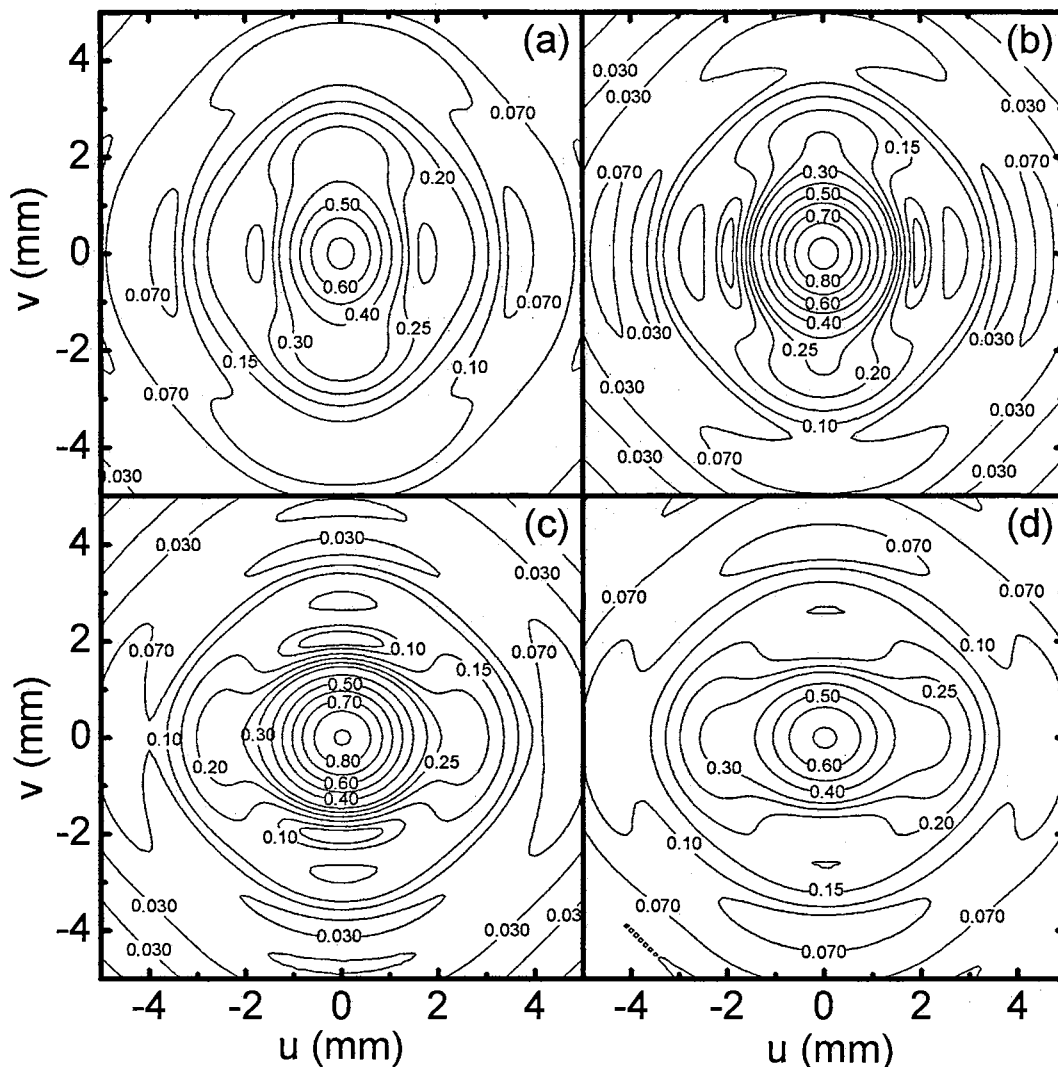


Figure 6-18. Transverse images of point source at 0.7 THz in (a) $z_2 = 574$ mm, (b) $z_2 = 586$ mm, (c) $z_2 = 610$ mm, (d) $z_2 = 622$ mm. All images have same amplitude scale.

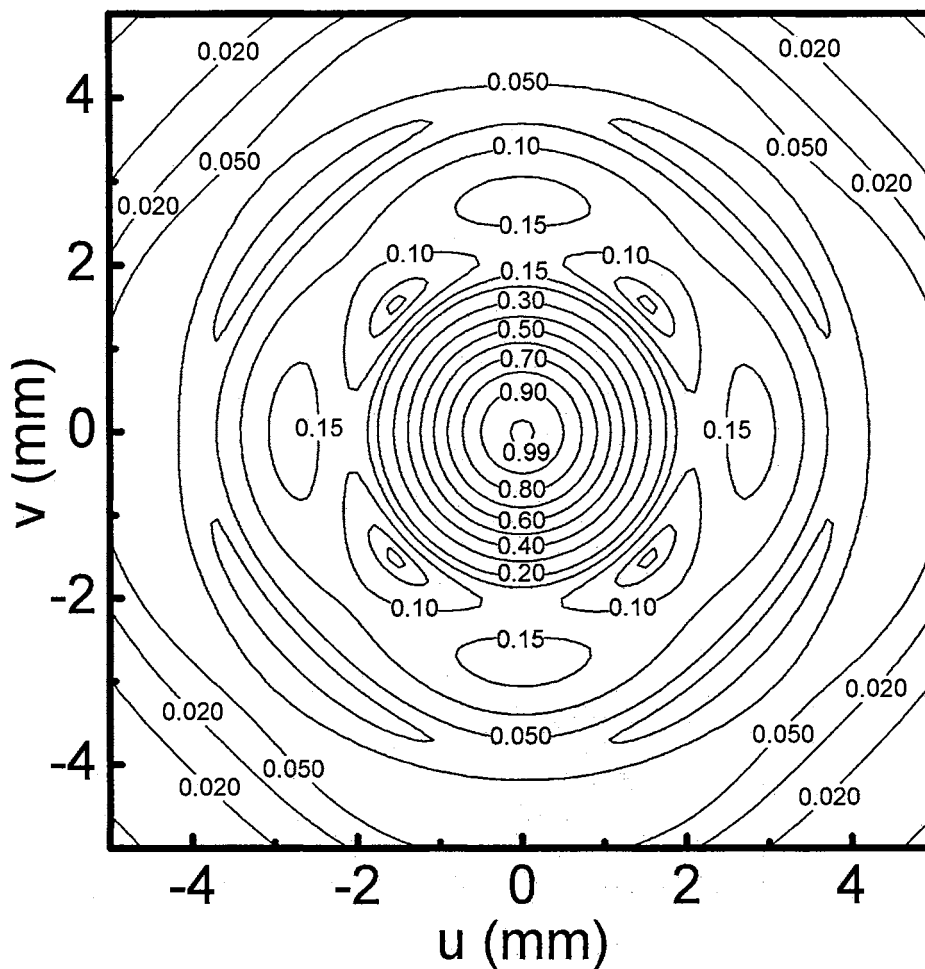


Figure 6-19. Transverse image of point source at 0.7 THz at circle of least confusion ($z_2 = 598$ mm). The amplitude scale is the same as that used in Figure 6-18.

6.4.4 Broadband Image

Accounting for the full spectrum of the THz pulse is equivalent to previous methods. As in equation 6-24, the spectrum of the pulse $S(\omega)$ is multiplied by the frequency dependent spatial field distribution (PSF) and the broadband image is the inverse temporal Fourier transform of this product. The only difference is that the PSF, represented by $h(\omega)$, is slightly different due to the off-axis system. Again, absolute time shifts can be neglected due to the time-invariance of the system. Figures 6-20 and 6-21

show the $u = 0$ and $v = 0$ slices through the two-dimensional broadband image of a point source calculated via the hybrid method. The image plane for these figures was positioned at the circle of least confusion, $z_2 = 598$ mm.

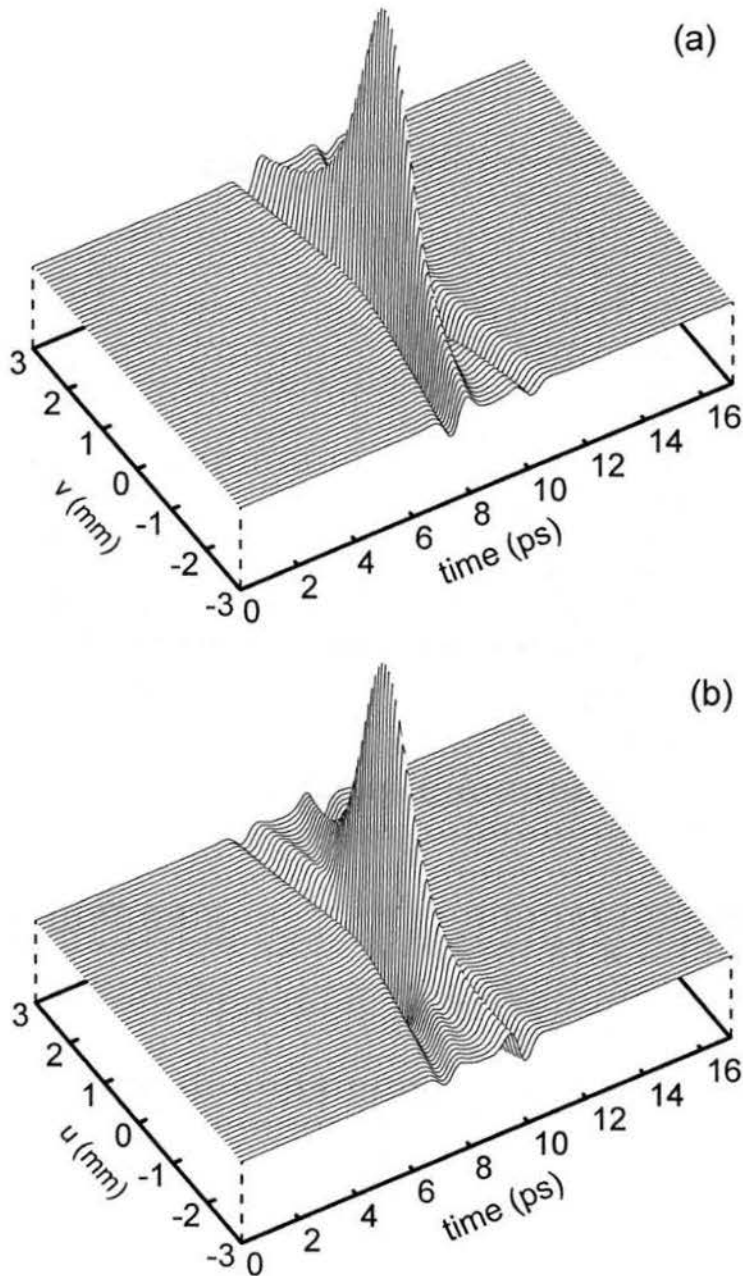


Figure 6-20. Normalized broadband image of point source using hybrid model, (a) $u = 0$ slice, (b) $v = 0$ slice.

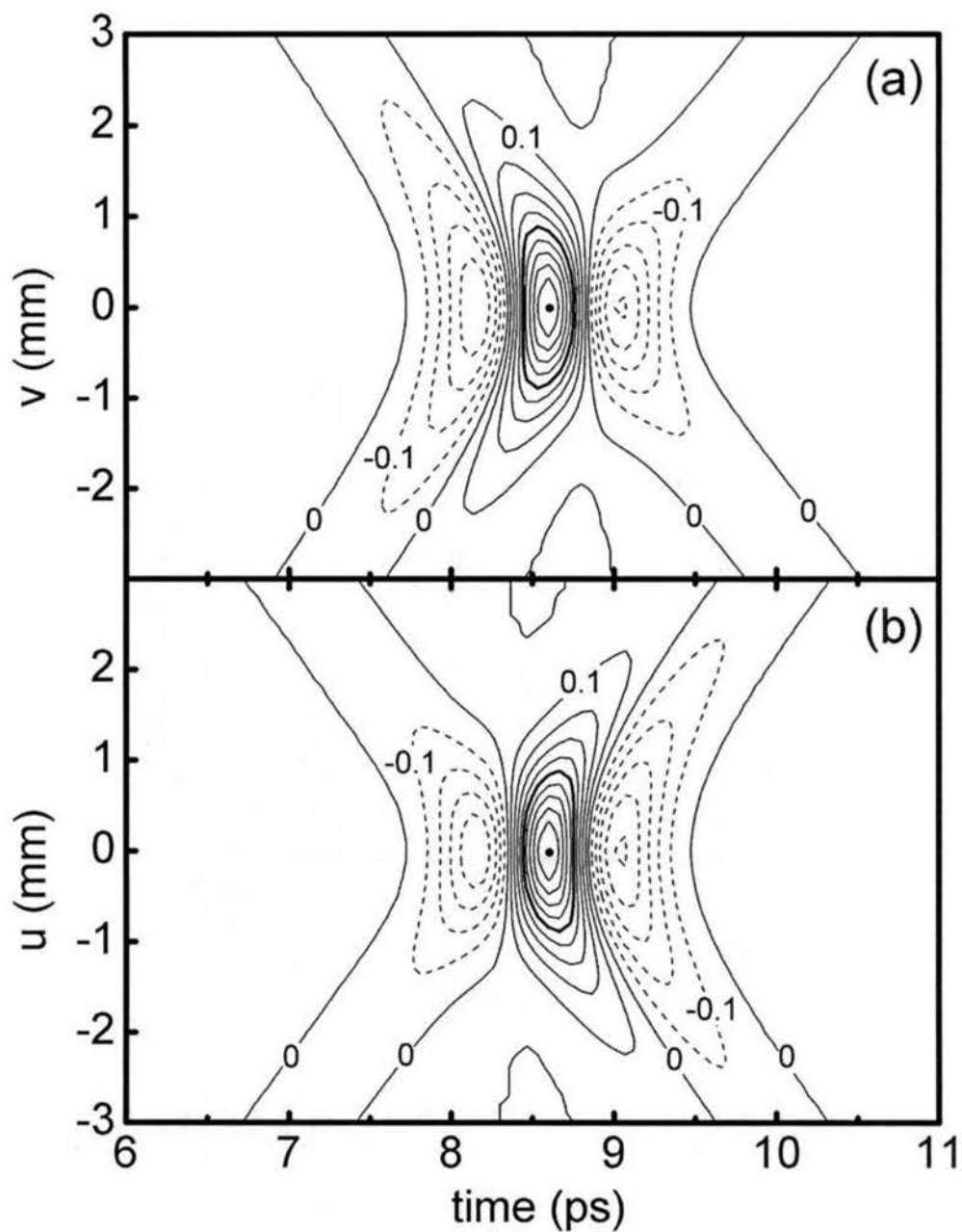


Figure 6-21. Normalized contour plan view of broadband point source image calculated with hybrid model. (a) $u = 0$ slice, (b) $v = 0$ slice. Contour spacing is 0.1, negative contours are denoted by dashed curves, heavy contour indicates 0.5 value. The peak value of unity is designated by the dot.

6.4.5 Comparison

In order to see their similarities, both the monochromatic and broadband images from all three models are shown in the following figures. Figure 6-22 shows the monochromatic images at 0.7 THz for all three models.

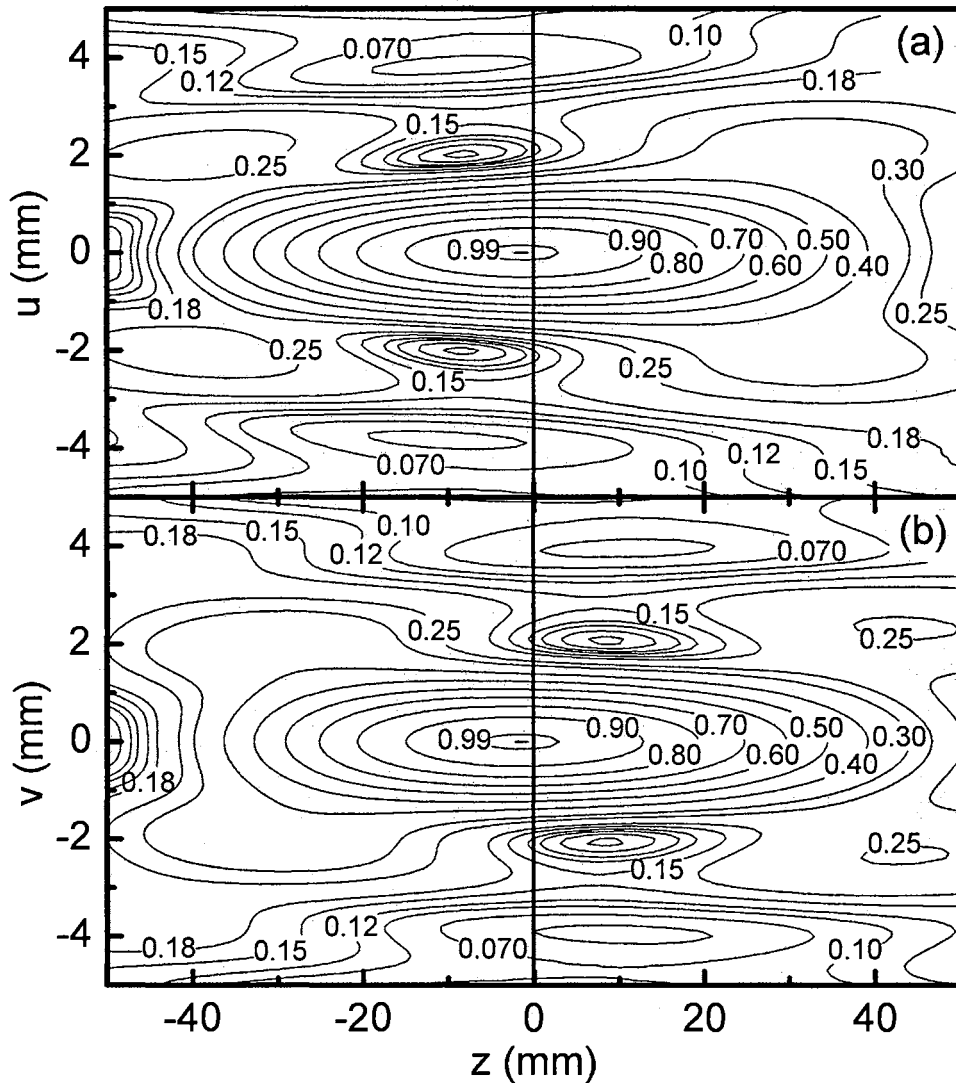


Figure 6-22. Monochromatic comparison images of point source calculated at 0.7 THz using (a) hybrid model, $v = 0$ slice, (b) hybrid model, $u = 0$ slice.

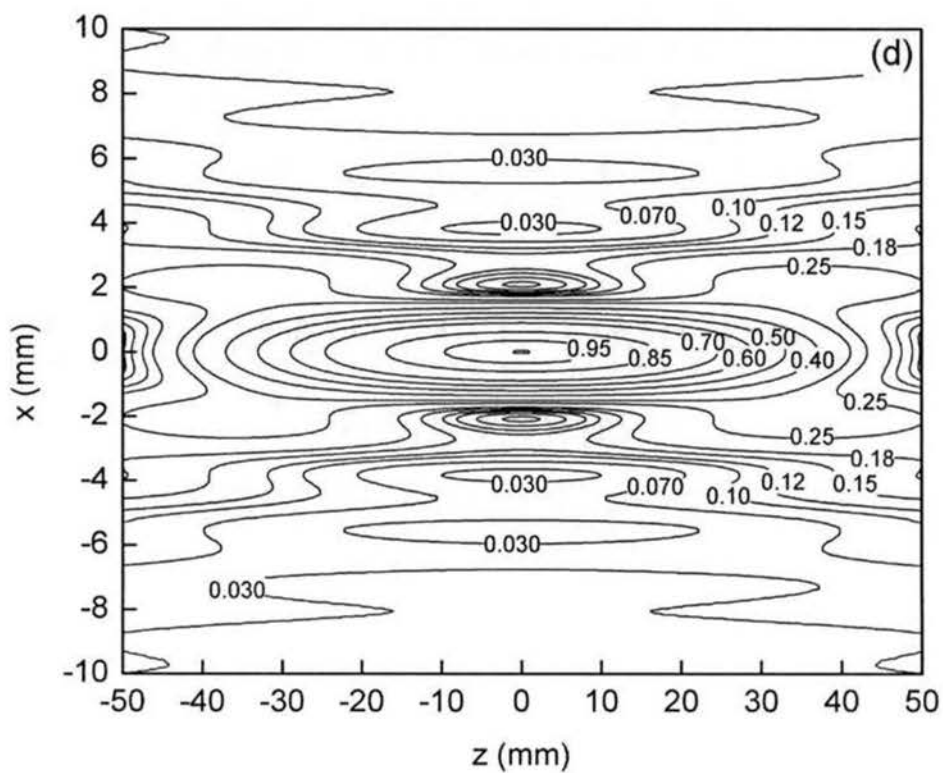
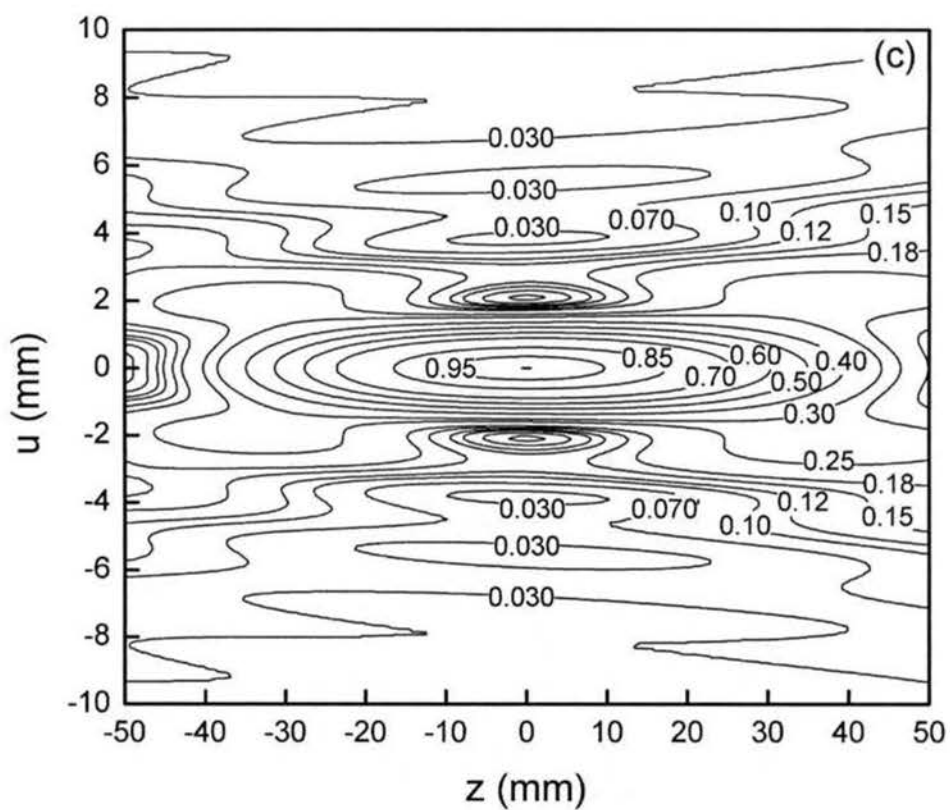


Figure 6-22. (cont.) Monochromatic images of point source calculated at 0.7 THz using (c) Goodman model, (d) Debye model.

Figure 6-23 shows the one-dimensional broadband images of a point source using all three models.

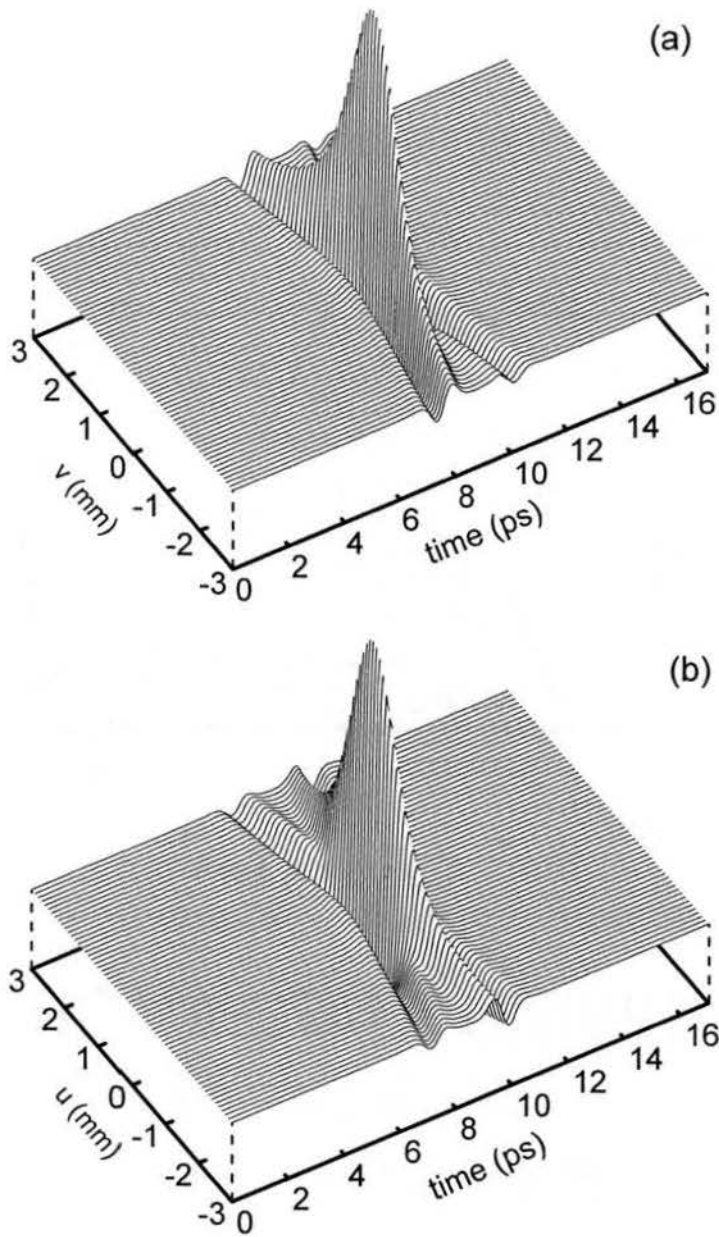


Figure 6-23. One-dimensional broadband image of point source using (a) hybrid model, $u = 0$ slice, (b) hybrid model, $v = 0$ slice.

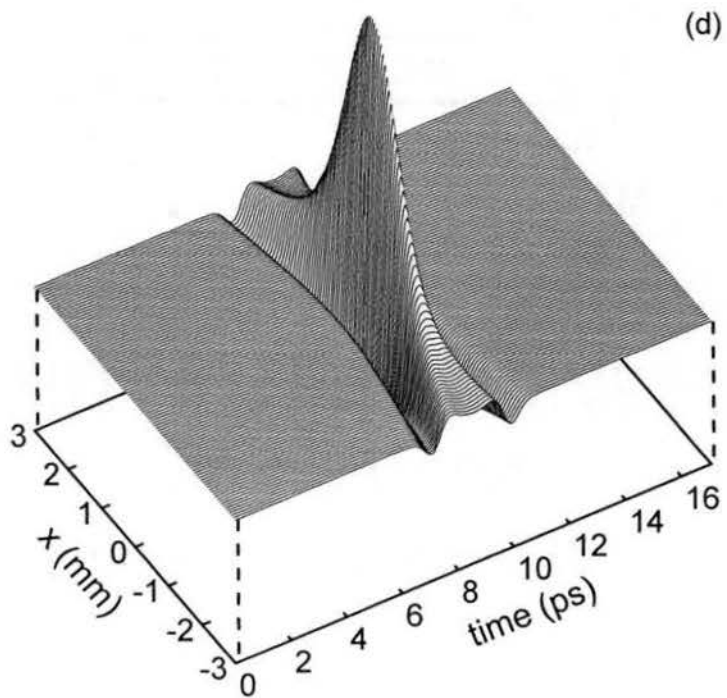
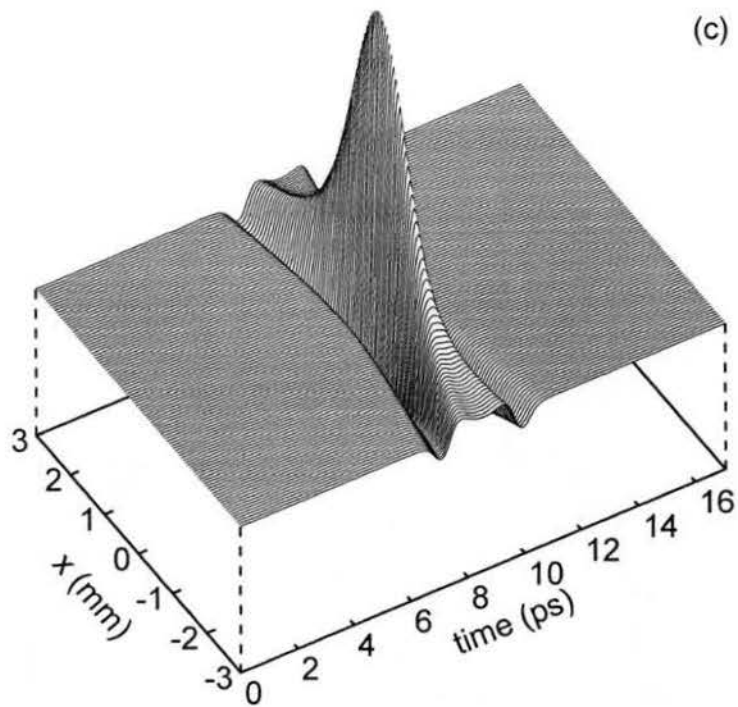


Figure 6-23. (cont.) One-dimensional broadband image of point source using (c) Goodman model, (d) Debye model.

The comparisons show that all three models return very similar results. The most notable differences in both the broadband and monochromatic images are found in the hybrid model. As already discussed, astigmatism causes the asymmetry in the monochromatic image calculated by the hybrid model. The continuing effect of astigmatism is also apparent in the broadband image where the wings of the image are slightly reshaped. To ensure these effects weren't caused by calculation inaccuracies, the hybrid model was also tested in a configuration wherein the off-axis angle of the system was set to zero. This allowed direct comparison to the images calculated by the other models. This experiment removed the effects of astigmatism and yielded images extremely similar to the other model images.

These comparisons indicate that all the models work quite well at describing the THz system but the direct accounting for aberrations and the flexibility afforded by the hybrid model make it the most useful. For this reason, the hybrid model was chosen for all the remaining comparisons to actual data.

6.4.6 Illumination Angle

Since all the models assumed a self-luminous object, some accounting was necessary for the fact that, in the real system, this is not the case. Based on the agreement between theory and data so far, it would appear that this is not a significant issue. For completeness, however, the theoretical correction for this situation is now discussed. We note first that the only prominent effect of the illumination angle is the skewed appearance of the image. In comparing theory and data it appears as though each spatial

sample is not changed significantly in shape but is only shifted in time. This is actually the case because in the normal imaging setup, the object never actually translates in z ; therefore the image plane also remains fixed in z . However, in its transverse motion, the object does pass through the angled illumination creating different pulse arrival times. Therefore, the obvious accounting of this phenomenon is to temporally shift each spatial sample in the theoretical image. The shift amount is determined by recalling that as the object moves δx in the $+x$ direction, it moves nearer to the transmitter by an amount $\delta x \cdot \sin(17^\circ)$, given the geometry shown in Figures 3-1 and 3-2. The illumination travels at c , therefore the time shift of each spatial sample should be $\delta x \cdot \sin(17^\circ)/c$, which is equal to $\delta x \cdot 0.97457$ ps/mm, δx being expressed in mm. For positive and negative δx this is a shift earlier and later in time, respectively. However, as discussed in section 4.1, the sampling nature of the system causes the receiver to sample the $-x$ side of the image as the object moves in the $+x$ direction. Therefore, positive and negative δx translate into shifts later and earlier in time, respectively. Since u and x are equivalent in scale, shifting the individual spatial samples by the amount prescribed yields the new broadband image shown in Figures 6-24 and 6-26. Only the $\nu = 0$ image data is shown because the angled illumination doesn't affect the image in the ν direction. These figures show the final form of the theoretical image of a point source and therefore represent the final form of the theoretical, broadband, amplitude PSF for the system. For comparison to data, Figures 6-25 and 6-27 show the actual image of a point source from section 4.1.

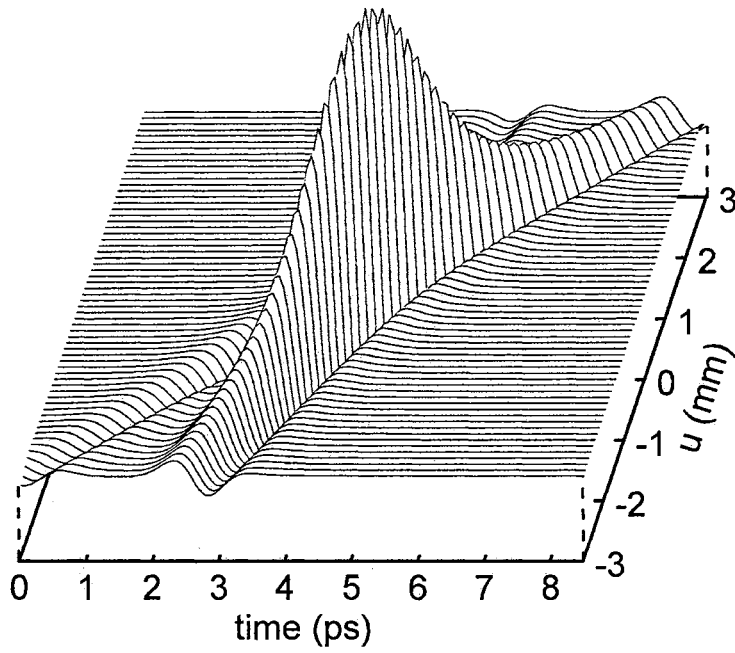


Figure 6-24. Slice $\nu = 0$, through two-dimensional THz image of point source under angled illumination. Final theoretical, broadband PSF of THz imaging system.

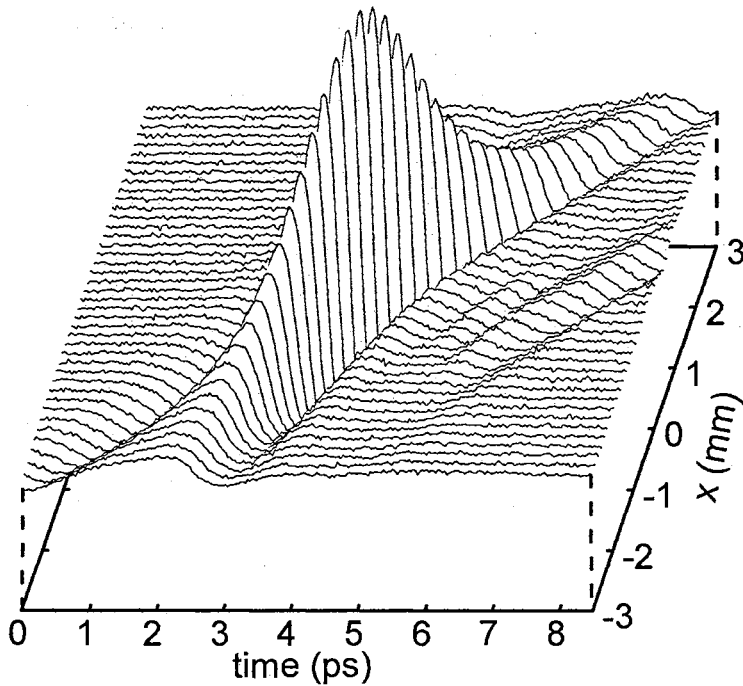


Figure 6-25. THz image of point source. Experimental, broadband PSF of THz imaging system.

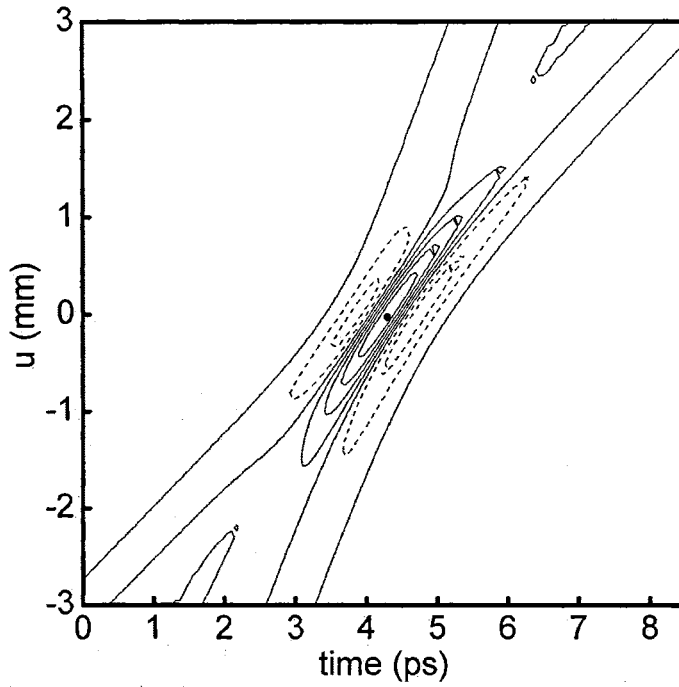


Figure 6-26. Contour plan view of Figure 6-24. Contour spacing is 0.2, negative contours are dashed curves. The peak value of unity is designated by the dot.

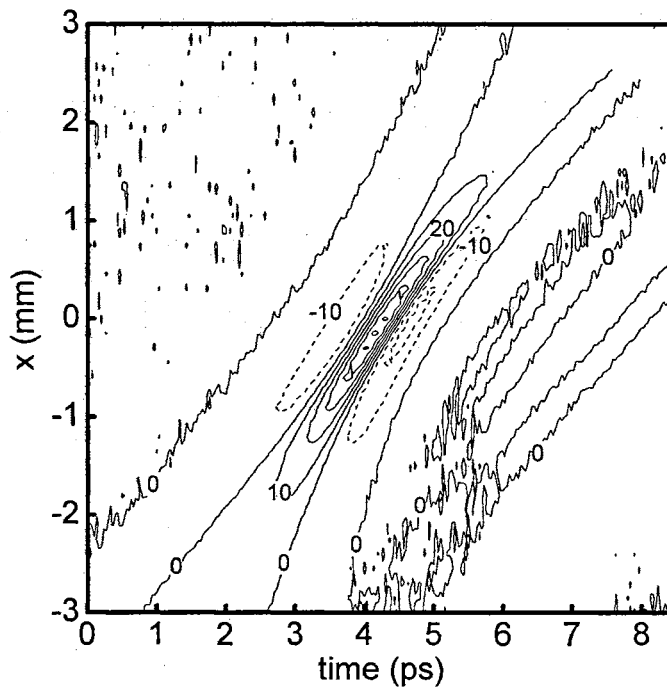


Figure 6-27. Contour plan view of Figure 6-25.

6.4.7 Diffraction Test by Mirror Size Reduction

In section 4.1.1, it was shown that halving the diameter of the spherical mirror resulted in a 1.72 times increase in the FWHM of the image of a point source. It was also stated that this is consistent with the theory for a diffraction limited system. This fact is now demonstrated. Figure 6-28a shows the side view of the image generated by the hybrid model using a spherical mirror with a 76.2 mm diameter, and Figure 6-28b shows the same theoretical image with the profile of the illumination beam taken into account. Figure 6-28c shows the side view of the experimental data for comparison.

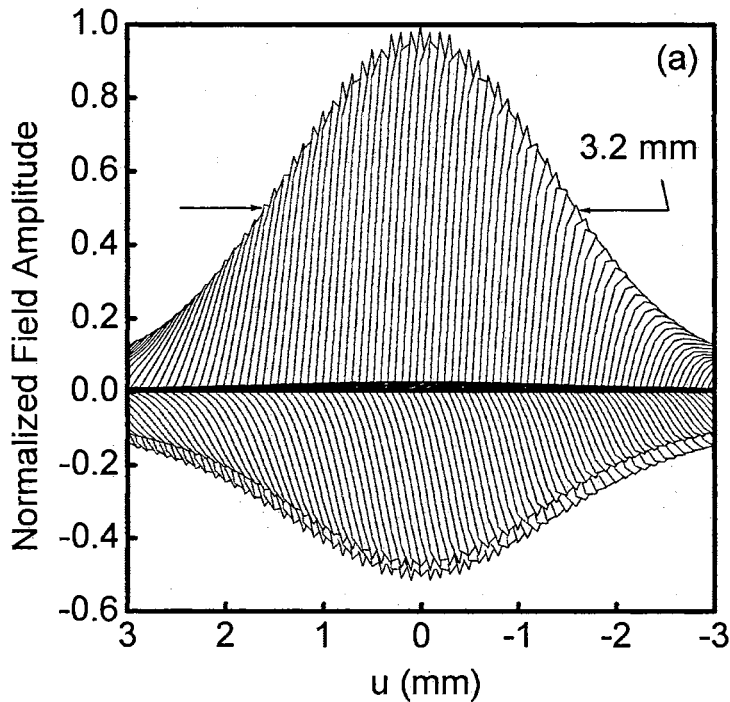


Figure 6-28. Comparison between theory and data for image of point source with 76.2 mm diameter spherical mirror. (a) theory image, no account for illumination beam profile.

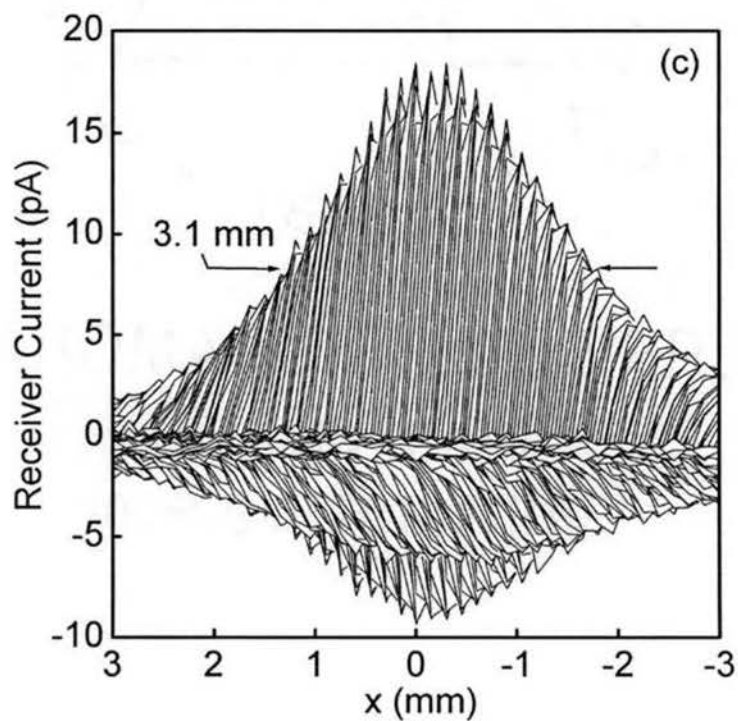
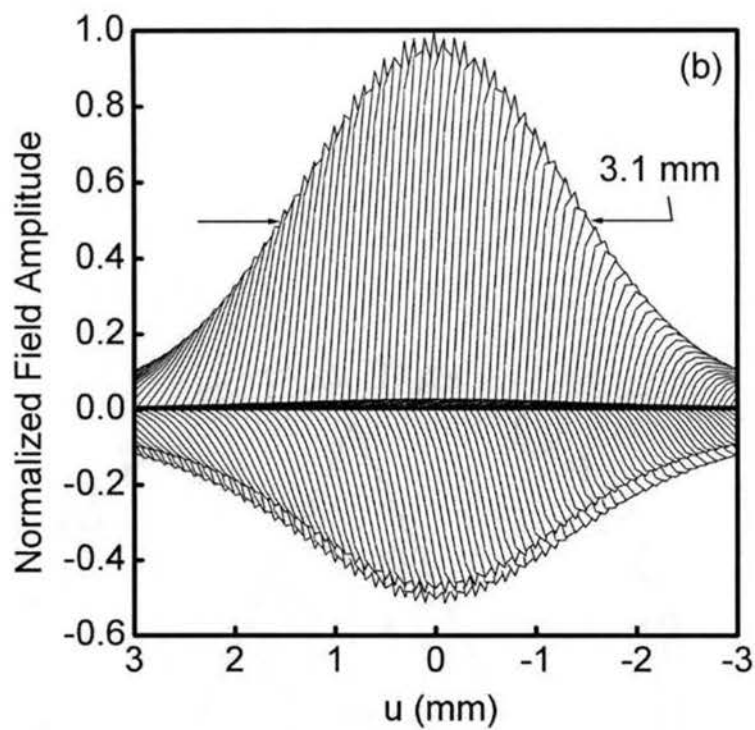


Figure 6-28. (cont.) (b) theoretical image with illumination beam profile accounted for
 (c) actual data from section 4.1.1.

The match between theory and data is quite good indicating that the THz imaging system is well-corrected. Since the receiver is not included in the theoretical models, these data reinforce the assumption that the effect of the receiver on the image is negligible.

6.4.8 Two Point Sources

There are two methods by which one can obtain the theoretical image of an object consisting of two point sources situated near each other. The first is to fully calculate the two individual images and superpose them. This most closely resembles what occurs in the actual THz imaging system and is the more correct solution. The second is to assume the THz system is both space-invariant (isoplanatic) and time-invariant, and then convolve the broadband PSF with two delta functions located in the positions of the point sources. One potential problem associated with this method is the assumption of space-invariance. The THz system is not strictly isoplanatic because image magnification and the geometric focal plane locations change as the object moves in the z direction. Also, image aberrations, astigmatism in particular, become greater as the object moves farther from the system optical axis. For large enough object translations, the effects of these aberrations would be greater than those of diffraction. However, the elongated, tubular shape of the image alleviates much of the space-variance problem by providing tolerance in the z -position of the object. Furthermore, the region bounding the transverse extent of the object in the THz system is sufficiently small, so the system behaves isoplanatically therein.

It is noted that the operation of the actual THz system involves translating the object such that the image translates in front of the fixed receiver. The theoretical image, however, is generated by assuming a fixed object and an array of receivers. In the theory, an object with large transverse extent would not be a good candidate for the assumption of space-invariance. For the actual system, however, every spatial sample of the image is observed from the same fixed point, as the image passes by. This also means that the object, as it moves, is always viewed by the system from the same fixed point. Now, the THz image of a point source is small enough that the source can be moved only 2 mm from center before most parts of the diffraction limited image fall from view. This means that any object, passing farther than 2 mm from the “seeing” point of the system falls out of view. Therefore, as long as the assumption of space-invariance is good over a circular transverse region with radius of 2 mm, the entire actual imaging system can be considered isoplanatic. This assumes the object is confined sufficiently in z such that magnification and focusing are not issues. All this means that the actual THz imaging system should be able to accurately image objects with much larger extent than the isoplanatic patch. It also means that the convolution method of determining the overall theoretical image should be very accurate, given objects with limited extent in the z dimension.

Figures 6-29 and 6-30 show the result of both the superposition and convolution methods of analysis, respectively. Both figures show the one-dimensional images of two point sources separated by 1.4 mm in x and 1.1 mm in z . They are in the same form as Figure 4-15 for comparison.

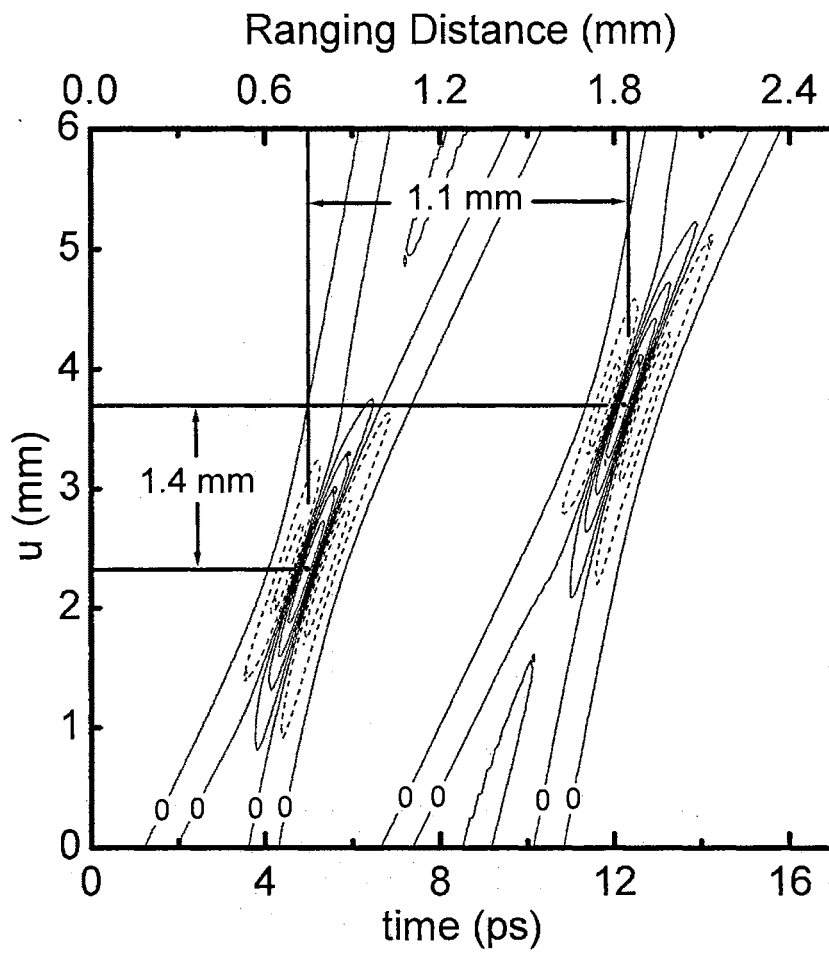


Figure 6-29. Superposition of two normalized point source images. Contours are separated by 0.2. Negative contours denoted by dashed curves.

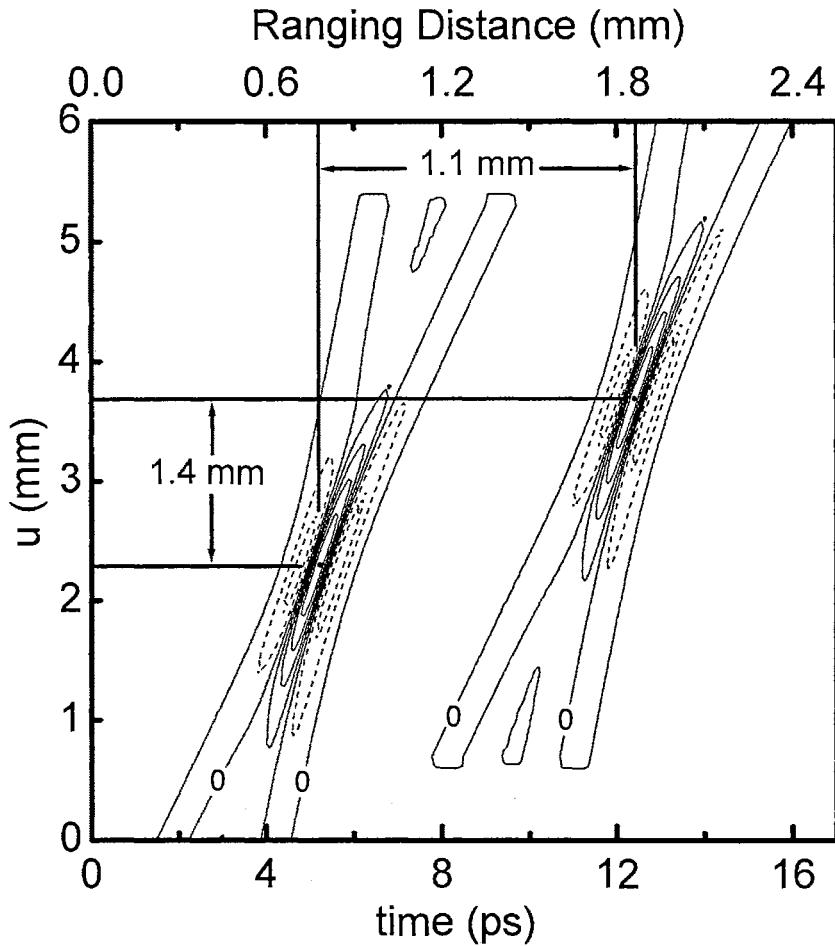


Figure 6-30. Two-dimensional convolution of two delta functions with the THz PSF. Contours separated by 0.2. Negative contours denoted by dashed curves.

Figure 6-30 shows the two-dimensional convolution of two delta functions with the PSF. The sharp cutoff features located at about $u = 5.3$ mm and 0.7 mm are artifacts of the convolution process and the fact that the PSF was only defined over a 0 to 6 mm transverse range. The image of Figure 6-29 was made by first calculating the image of a single point source, then calculating the image again after moving the point source 1.1 mm in z and 1.4 mm in x . The two resulting images were finally superposed. Since both calculations were performed over the entire observation range the cutoff artifacts are not present. Figure 6-31 shows a side-by-side comparison between Figure 6-29 and 4-15.

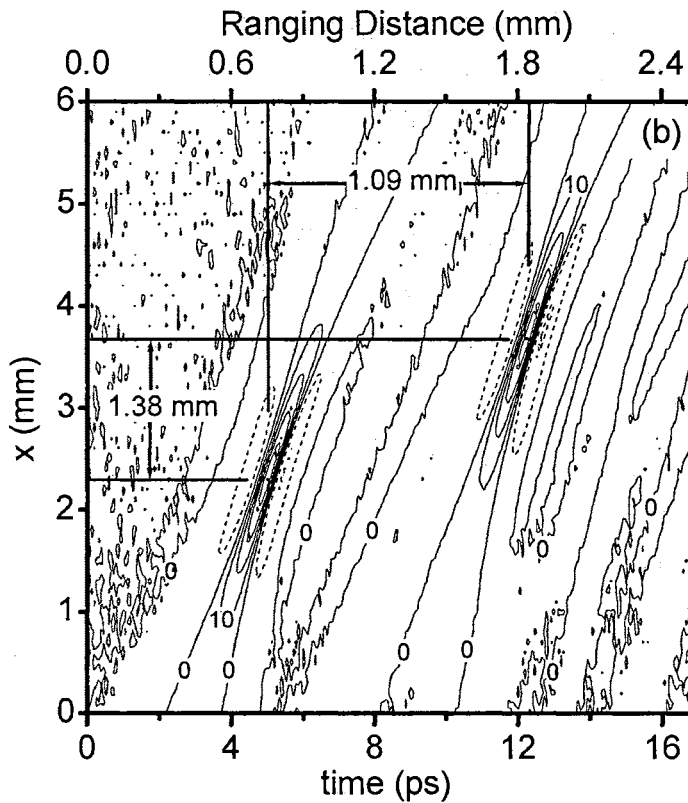
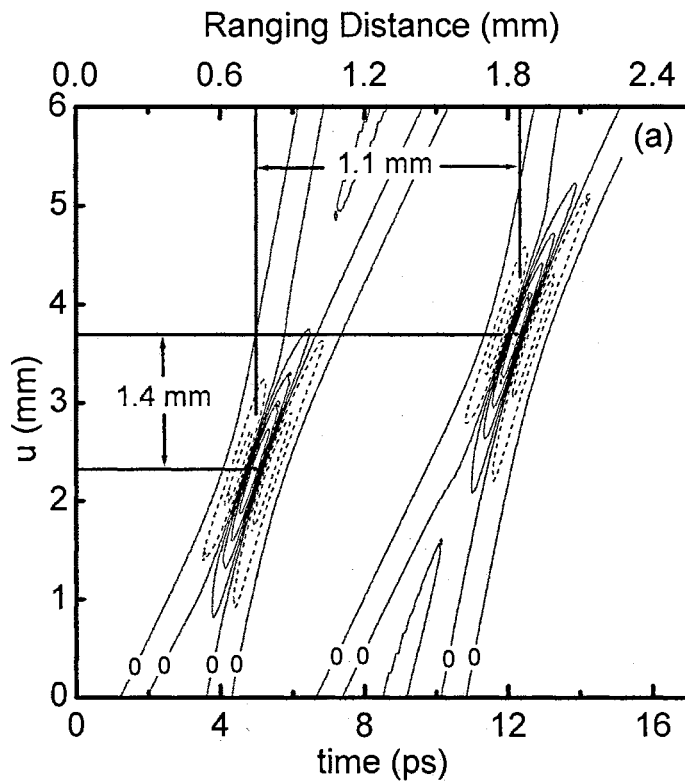


Figure 6-31. Comparison between (a) normalized theory, and (b) data from section 4.2. Negative contours are denoted by dashed curves.

The similarity between the convolution and superposition images illustrates the fact that the system is essentially space-invariant. Therefore, it is possible to predict the image of a much more complicated object by simply convolving the object with the PSF. It is noted, however, that the theory assumes a self-luminous object and then later corrects the timing effects of the angled illumination and the ranging nature of the system. This is not strictly equivalent to the experimental arrangement because stealth effects like those illustrated in Figure 5-30 could make extended objects invisible to the system. While the theory may predict a visible image, the experimental arrangement will, in certain cases, yield dissimilar results.

6.5 Arrayed Images

Having already formed a working model for the image of a point source it is very easy to extend the theory to arrayed imaging. Just as is in the actual system, theoretical arraying requires only the superposition of images to obtain an overall arrayed image. For all the following theoretical arrayed images the broadband, hybrid model was used to generate the individual images. In addition, all the individual images were calculated with a proper phase relationship among them such that arraying would be successful.

The elongated cylindrical shape of the focal region permits the following approximation to be made when considering arrays wherein the angular separation between array elements is sufficiently small ($< 20^\circ$). Recall that the object is scanned in an angled configuration to achieve the effects of a synthetic mirror. Consequently the scan plane has a slight z -dependence when it is tilted about either the x or y axis.

Therefore most of the spatial samples of the image will be recorded when the object had some non-zero z -location. For small angular separation between array elements this z -motion can be neglected as far as its effect on the spatial field distribution goes. The z -motion must be accounted for in timing, however, but this can easily be done in conjunction with the timing shifts used to correct for the illumination angle. Simple time-delays are appropriately added to the spatial samples depending on their (u,v) positions and the angular separation between the array elements. Recall that the illumination path length change for tilted scan planes caused an effective doubling of the overall phased-array aperture size. This phenomenon also occurs for theoretical arrayed imaging, as expected.

6.5.1 Single 1 mm Ball

It was mentioned in section 5.6 that the arrayed image of a single 1 mm ball (point source) matched well with theoretical predictions. Therefore the theoretical arrayed image of a point source is now demonstrated. For this calculation the source was located at $x = y = 0$ and two images were calculated with scan plane orientations tilted at 0° and -16° about the x -axis. The results of this calculation are shown in Figures 6-32 and 6-34 and are shown along with the actual data images from section 5.6.2 in Figures 6-33 and 6-35.

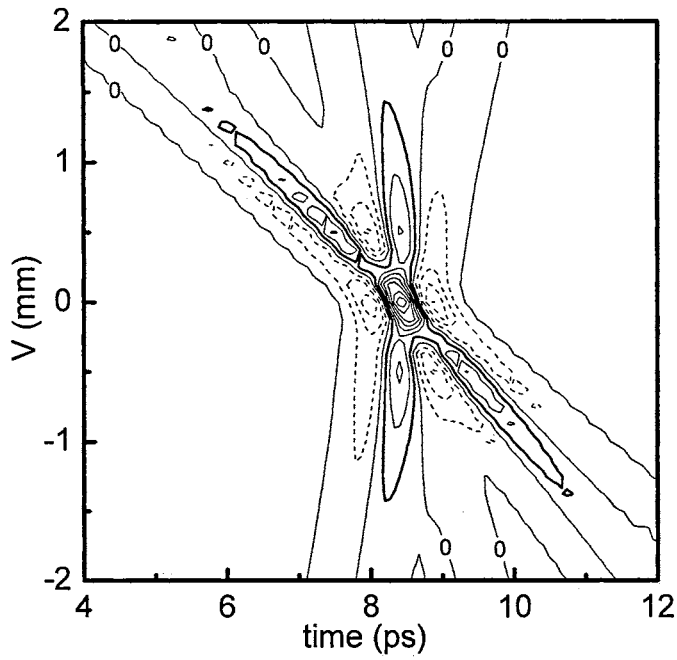


Figure 6-32. Slice $x = 0$ through normalized theoretical phased-array image data. Contours separated by 0.125. Negative contours denoted by dashed curves. Contour at 0.125 shown as heavy curve to outline pulse peaks.

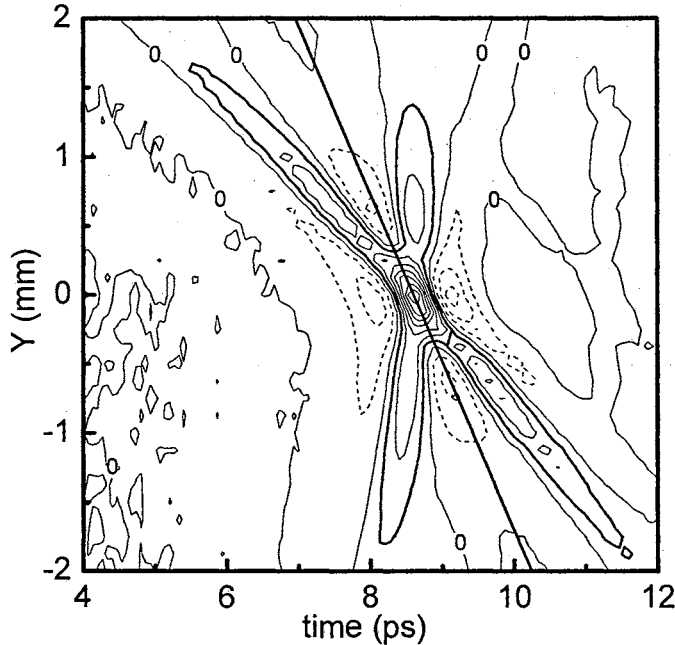


Figure 6-33. Slice $x = 0$ through normalized, experimental, phased-array THz image of a point source. Contours separated by 0.125. Negative contours denoted by dashed curves. Contour at 0.125 shown as heavy curve to outline pulse peaks.

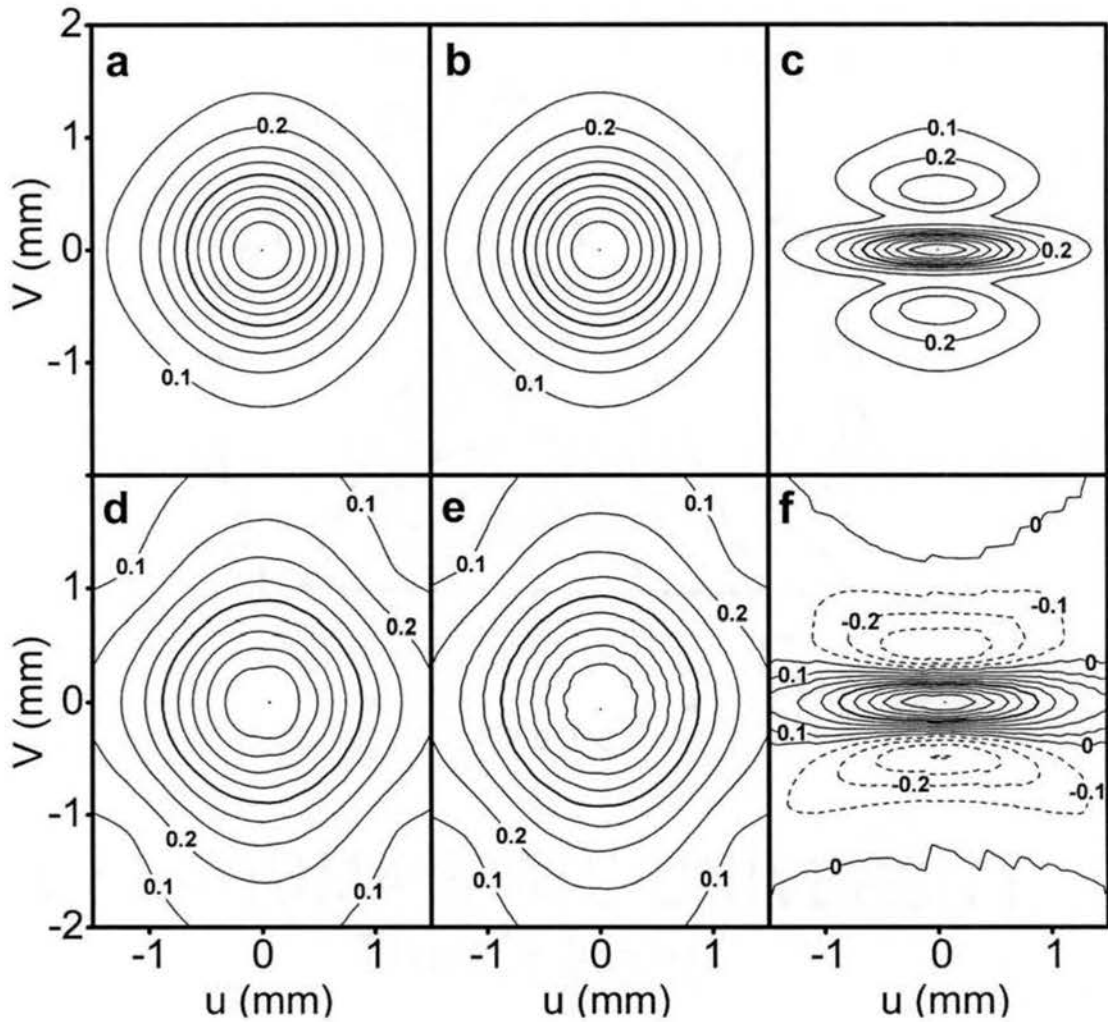


Figure 6-34. Normalized theoretical transverse images of THz point source. (a) 0° energy image (b) 16° energy image, (c) phased-array energy image, (d) 0° amplitude image, (e) 16° amplitude image, (f) phased-array amplitude image. Contours separated by 0.1. Negative contours denoted by dashed curves. Contour for 0.5 shown as heavy curve.

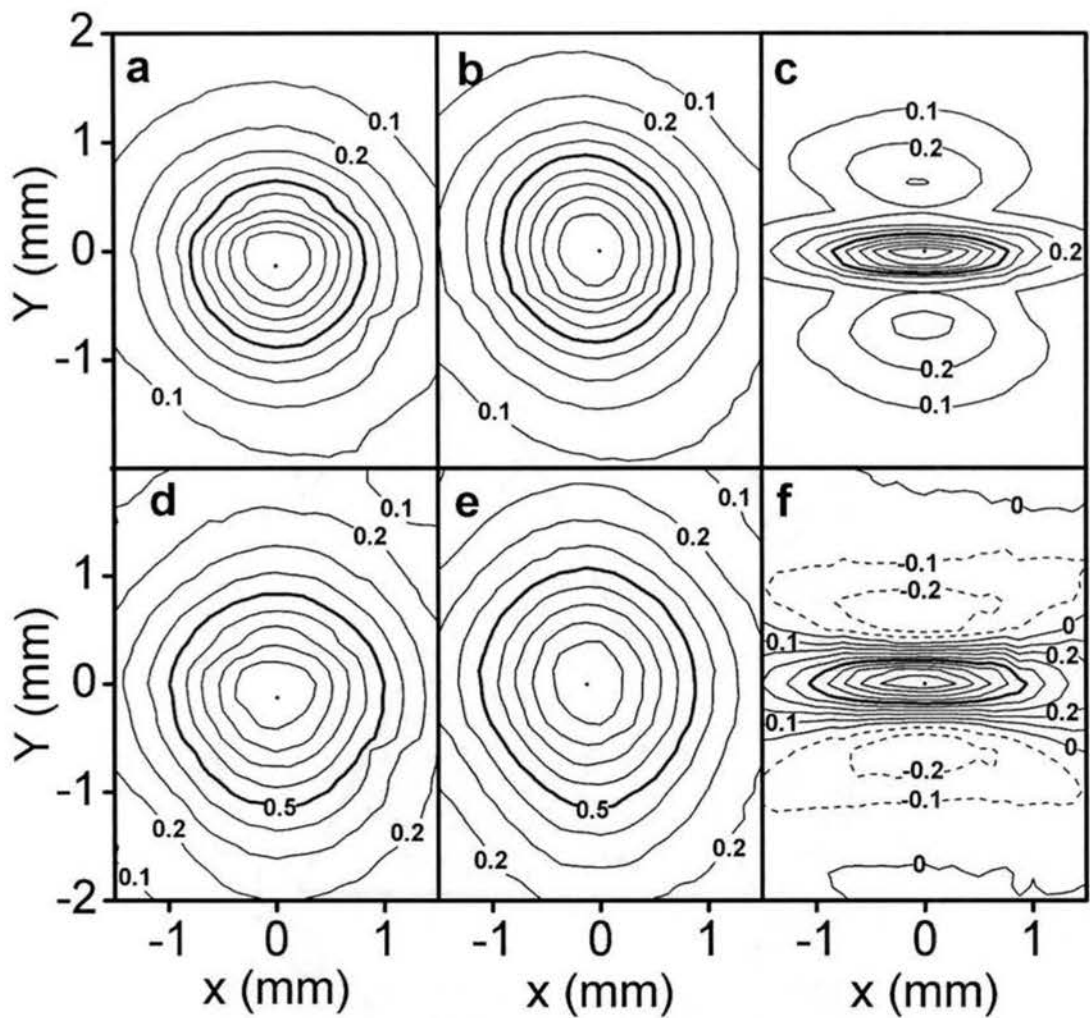


Figure 6-35. Normalized experimental transverse images of THz point source. (a) 0° energy image (b) 16° energy image, (c) phased-array energy image, (d) 0° amplitude image, (e) 16° amplitude image, (f) phased-array amplitude image. Contours separated by 0.1. Negative contours denoted by dashed curves. Contour for 0.5 shown as heavy curve.

The theoretical images show a good agreement with the data in terms of both transverse resolution and side lobe amplitude, indicating that the theoretical approach to describing the arrayed images is valid.

6.5.2 Two 400 μm Balls

For more comparisons to actual data, the theoretical arrayed image of two point sources separated by 400 μm in y and 50 μm in z was calculated. These sources have essentially the same layout as the two 391 μm balls used to obtain Figures 5-16, 5-18, and 5-19 in section 5.7.1. Arraying was done in the vertical direction only and array orientations were 0° , 10° and -10° , just as in the actual data. Again, the theory corrects the timing effects of the angled illumination and the ranging nature of the system, but assumes a self-luminous object. Therefore the double reflection feature which was present in the experimental data did not appear in the theory. Figures 6-36, 6-38a and 6-39a show the calculated array images for this object. Figures 6-37, 6-38b and 6-39b show the actual imaging data from section 5.7.1 for comparison. Recall that in Figures 6-38 and 6-39 the experimental images are shifted up 200 μm in y , relative to the theoretical images due to the method by which the phase lock was established. This does not affect the comparison.

Again, the agreement between theory and data suggests the system is operating very near to theoretical limits as assumed. Moreover it shows the validity of using time-delays to mimic the z -motion of the object, thus demonstrating, once again, the tolerance in z and the effective equivalence in t and z .

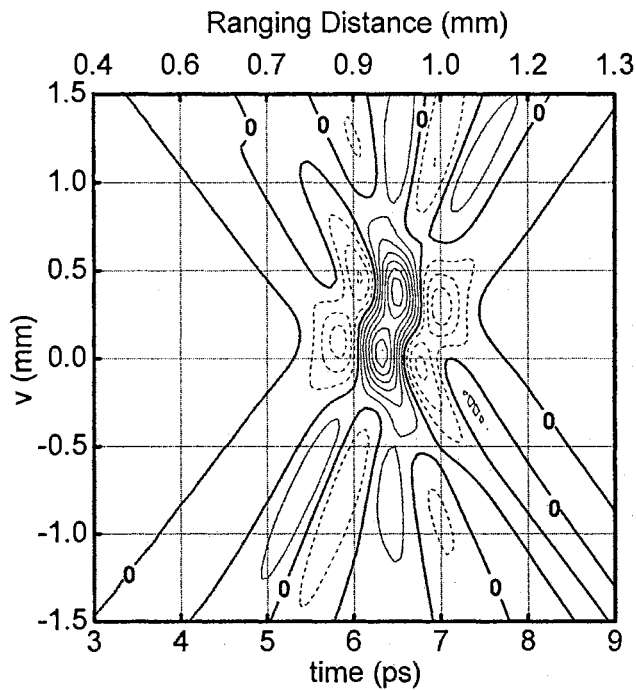


Figure 6-36. Slice $u = 0$ through normalized, theoretical, phased-arrayed image of two point sources. Contour separation = 0.15. Negative contours are indicated by dashed curves.

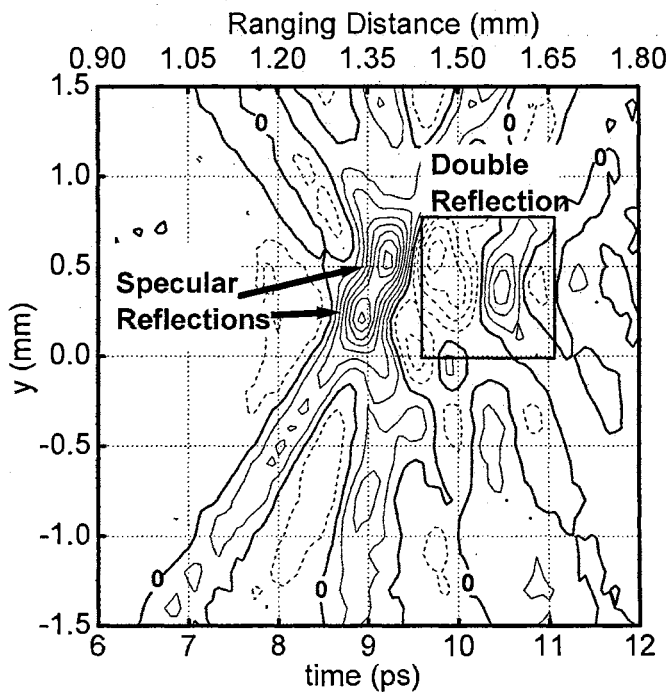


Figure 6-37. Slice $x = 0$ through experimental, phased-array image of two balls. Contours are separated by 7 pA. Negative contours are indicated by dashed curves.

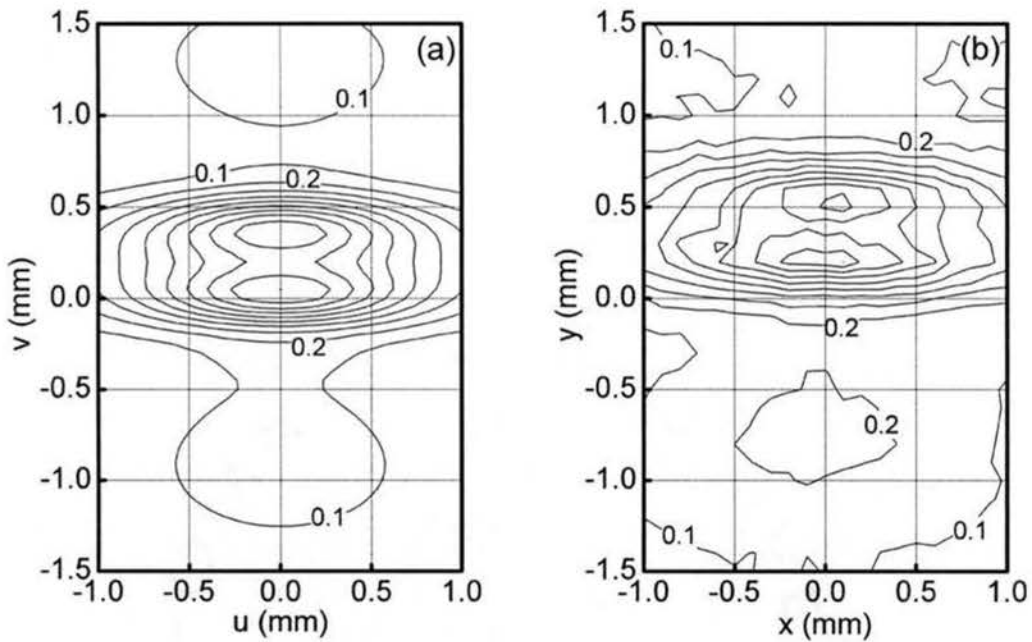


Figure 6-38. Normalized transverse arrayed energy images of two point sources, (a) theoretical image, (b) experimental image from section 5.7.1. Contour separation = 0.1.

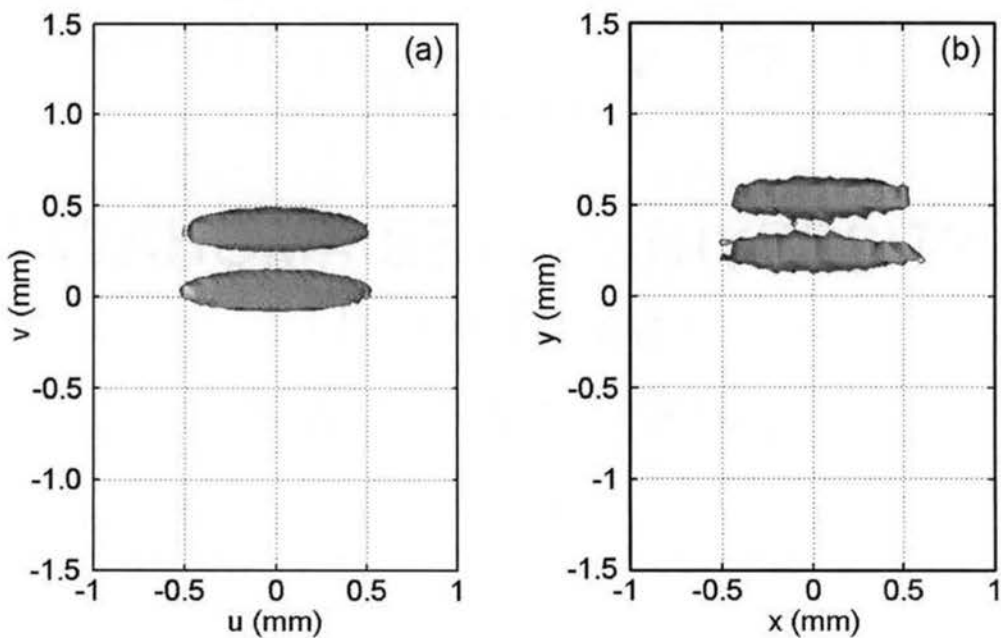


Figure 6-39. Transverse isoamplitude plots. Surfaces contain data values which have amplitude greater than 80% of the peak amplitude. (a) theoretical image, (b) experimental image from section 5.7.1.

Chapter 7

Conclusions

A quasi-optic, synthetic, phased-array THz imaging system has been presented in this dissertation. The system forms real, coherent, diffraction-limited, THz amplitude images which by means of a large-aperture spherical mirror. The images are complete and independent, yet have well-defined phase relationships allowing them to be combined with simple AS methods to achieve higher resolution imaging. Due to the pulsed illumination, the system exhibits not only transverse spatial resolution but also ranging resolution. This radar behavior allows the system to perform imaging over two spatial dimensions and one temporal dimension simultaneously, and also provides a natural means of phase-locking multiple images together for AS.

The first part of the study demonstrated one-dimensional imaging of point sources. By imaging a point reflector, the broadband, amplitude PSF of the system was determined. It was found that the system was well-corrected (or diffraction limited) and the resolution was limited by the extent of the spherical mirror. Decreasing the size of this mirror caused a decrease in the transverse resolution by an amount that agreed very well with theoretical predictions. At the same time, range resolution was unaffected. Imaging two point sources together highlighted some of the resolution benefits of a coherent, pulsed imaging system. In particular, the transverse spatial resolution between

two image features was enhanced by their temporal separation, which does not permit them to smear together into one un-resolvable unit.

The second part of this study demonstrated an AS technique whereby the spherical mirror was effectively moved, thus acting as a synthetic phased-array element. Several images were recorded, each by a different phased-array element. Combining these separate images formed a higher resolution, composite image. Due to the sparse-aperture setup, no image reconstruction was necessary when the images were properly phase locked to a common reference. Instead, this form of AS was accomplished by simple superposition of separate images. Both vertical and horizontal arraying were demonstrated and exhibited resolution gains of about four times. Many different forms of image processing were demonstrated, and each highlighted the power and flexibility inherent in a coherent, pulsed imaging system. Other imaging phenomena, such as object stealth and artificial aperture doubling, were also explained and showed some of the more unconventional attributes of the THz imaging system.

Finally, the last part of this dissertation presented three theoretical models of the THz imaging system. Each successive model incorporated more of the physical attributes of the actual system and provided a more accurate picture of how the system behaved. All of the models used, to some extent, a combination of geometric optics and diffraction theory. Since the models assumed self-luminous objects, they were able to account for all the features in the data except for higher order effects such as double reflections between closely placed objects. All of the models verified that the system was well-corrected and that the effect of the receiver on spatial resolution was negligible. The models were all compared to each other and to the experimental data and all showed

good agreement.

This study demonstrated the feasibility of a system that can produce THz images sharp enough to resolve features whose size was on the order of a wavelength or less. Such an imaging system promises application in many types of non-invasive imaging arenas for which microwave techniques cannot obtain sharp enough resolution and optical techniques cannot be used due to opacity or optical sensitivity. One problem not addressed in this dissertation is the fact that data collection is very slow. Typical, individual, two-dimensional images require several days to record. This duration is multiplied in arrayed imaging due to the fact that many images must be collected. With more research in THz technologies, it is likely that much more powerful transmitters will become available. In this case, data collection could be drastically accelerated because long integration time would no longer be necessary to achieve usable SNRs.

References

1. D. H. Auston, K.P. Cheung, and P.R. Smith, "Picosecond photoconducting Hertzian dipoles", *Appl. Phys. Lett.* **45**, 284-286 (1984).
2. M. B. Ketchen, D. Grischkowsky, T. C. Chen, C-C. Chi, I. N. Duling, III, N. J. Halas, J-M. Halbout, J. A. Kash, and G. P. Li, "Generation of subpicosecond electrical pulses on coplanar transmission lines", *Appl. Phys. Lett.* **48**, 751-753 (1986).
3. B. B. Hu, X.-C. Zhang, D. H. Auston and P. R. Smith, "Free-space radiation from electro-optic crystals", *Appl. Phys. Lett.* **56**, 506-508 (1990).
4. Q. Wu and X.-C. Zhang, "Free-space electro-optic sampling of terahertz beams", *Appl. Phys. Lett.* **67**, 3523-3525 (1995).
5. B. B. Hu and M. C. Nuss, "Imaging with terahertz waves", *Opt. Lett.* **20**, 1716-1718 (1995).
6. D. M. Mittleman, S. Hunsche, L. Boivin, and M. C. Nuss, "T-ray tomography", *Opt. Lett.* **22**, 904-906 (1997).
7. Q. Wu, T. D. Hewitt, and X.-C. Zhang, "2-dimensional electro-optic imaging of THz beams", *Appl. Phys. Lett.* **69**, 1026-1028 (1996).
8. Z. Jiang and X.-C. Zhang, "Single-shot spatiotemporal terahertz field imaging", *Opt. Lett.* **23**, 1114-1116 (1998).

9. D. M. Mittleman, M. Gupta, R. Neelamani, R.G. Baraniuk, J.V. Rudd, and M. Koch, "Recent advances in terahertz imaging", *Appl. Phys. B* **68**, 1085-1094 (1999).
10. K. McClatchey, M. T. Reiten, and R. A. Cheville, "Time resolved synthetic aperture terahertz impulse imaging", *Appl. Phys. Lett.* **79**, 4485-4487 (2001).
11. D. M. Mittleman, R. H. Jacobsen, and M. C. Nuss, "T-Ray Imaging", *IEEE J. Sel. Top. Quant. Electron.* **2**, 679-692 (1996).
12. D. Grischkowsky, S. Keiding, M. van Exter, Ch. Fattinger, "Far-infrared time-domain spectroscopy with terahertz beams of dielectrics and semiconductors", *J. Opt. Soc. Am. B* **7**, 2006-2019 (1990).
13. L. Thrane, R. H. Jacobsen, P. Uhd Jepsen, and S. R. Keiding, "THz reflection spectroscopy of liquid water", *Chem. Phys. Lett.* **240**, 330-333 (1995).
14. J. T. Kindt and C. A. Schmuttenmaer, "Far-infrared dielectric properties of polar liquids probed by femtosecond terahertz pulse spectroscopy", *J. Phys. Chem.* **100**, 10373-10379 (1996).
15. M. van Exter, C. Fattinger, and D. Grischkowsky, "Terahertz time-domain spectroscopy of water vapor", *Opt. Lett.* **14**, 1128-1130 (1989).
16. M. van Exter and D. Grischkowsky, "Characterization of an Optoelectronic Terahertz Beam System", *IEEE Trans. Microwave Theory Tech.* **38**, 1684-1691 (1990).
17. S. W. Smye, J. M. Chamberlain, A. J. Fitzgerald, and E. Berry, "The interaction between Terahertz radiation and biological tissue", *Phys. Med. Biol.* **46**, R101-R112 (2001).

18. M. Brucherseifer, P. Haring Bolivar, H. Klingenberg, and H. Kurz, "Angle-dependent THz tomography – characterization of thin ceramic oxide films for fuel cell applications", *Appl. Phys. B* **72**, 361-366 (2001).
19. R. A. Cheville and D. Grischkowsky, "Far-infrared terahertz time-domain spectroscopy of flames", *Opt. Lett.* **20**, 1646-1648 (1995).
20. M. C. Nuss, "Chemistry is Right for T-Ray Imaging", *IEEE Circuits Devices* **12**, 25-30 (1996).
21. J. O'Hara and D. Grischkowsky, "Quasi-optic terahertz imaging", *Opt. Lett.* **26**, 1918-1920 (2001).
22. J. O'Hara and D. Grischkowsky, "Synthetic phased-array terahertz imaging", *Opt. Lett.* **27**, 1070-1072 (2002).
23. J. W. Goodman, *Introduction to Fourier Optics*, 2nd ed. (McGraw-Hill, New York 1996).
24. E. Hecht, *Optics*, 4th ed. (Addison Wesley, San Francisco, CA, 2002).
25. M. Born and E. Wolf, *Principles of Optics*, 7th ed. (Cambridge U. Press, Cambridge, 1999).
26. J. J. Stamnes, *Waves in Focal Regions* (Adam Hilger, Redcliffe Way, Bristol, 1986).
27. A. J. den Dekker and A. van den Bos, "Resolution: a survey", *J. Opt. Soc. Am. A* **14**, 547-557 (1997).
28. N. Katzenellenbogen and D. Grischkowsky, "Efficient generation of 380 fs pulses of THz radiation by ultrafast laser excitation of a biased metal-semiconductor interface", *Appl. Phys. Lett.* **58**, 222-224 (1991).

29. P. G. Huggard, C. J. Shaw, J. A. Cluff, and S. R. Andrews, "Polarization-dependent efficiency of photoconducting THz transmitters and receivers", *Appl. Phys. Lett.* **72**, 2069-2071 (1998). Ref43
30. B. E. A. Saleh and M. C. Teich, *Fundamentals of Photonics* (John Wiley & Sons, New York, 1991).
31. R. A. Cheville and D. Grischkowsky, "Time domain terahertz impulse ranging studies", *Appl. Phys. Lett.* **67**, 1960-1962 (1995).
32. R. Mendis and D. Grischkowsky, Personal communication.
33. W. M. Masri, *Diffraction-corrected synthetic aperture focusing for spherical ultrasonic radiators*, (Ph.D. dissertation, Iowa State University, 1997).
34. H. Fizeau, "Prix Bordin: Rapport sur le concours de l'année 1867", *C. R. Acad. Sci.* **66**, 932-934 (1868).
35. A. A. Michelson, "Measurement of Jupiter's satellites by interference", *Nature* **45**, 160-161 (1891).
36. J. D. Kraus, *Radio Astronomy*, (McGraw-Hill, New York, 1966).
37. M. Ryle and A. Hewish, "The synthesis of large radio telescopes", *Mon. Not. R. Astron. Soc.* **120**, 220-230 (1960).
38. P. J. Napier, A. R. Thompson, and R. D. Ekers, "The Very Large Array: Design and Performance of a Modern Synthesis Radio Telescope", *Proc. IEEE* **71**, 1295-1322 (1983).

39. P. J. Napier, D. S. Bagri, B. G. Clark, A. E. E. Rogers, J. D. Romney, A. R. Thompson, and R. C. Walker, "The Very Long Baseline Array", *Proc. IEEE* **82**, 658-672 (1994).
40. R. A. Monzingo and Thomas W. Miller, *Introduction to Adaptive Arrays*, (John Wiley & Sons, New York, 1980).
41. A. Labeyrie, "Interference fringes obtained on Vega with two optical telescopes", *Astrophys. J.* **196**, L71-L75 (1975).
42. A. R. Hajian and J. T. Armstrong, "A Sharper View of the Stars", *Sci. Am.* **284**, 56-63 (2001).
43. A. Broquetas, J. Palau, L. Jofre, and A. Cardama, "Spherical wave near-field imaging and radar cross-section measurement", *IEEE Trans. Antennas Propag.* **46**, 730-735 (1998).
44. D. Mensa, *High Resolution Radar Imaging*, (Artech House, Dedham, MA 1981).
45. A. B. Ruffin, J. Decker, L. Sanchez-Palencia, L. Le Hors, J. F. Whitaker, T. B. Norris, and J. V. Rudd, "Time reversal and object reconstruction with single-cycle pulses", *Opt. Lett.* **26**, 681-683 (2001).
46. T. D. Dorney, J. L. Johnson, J. Van Rudd, R. G. Baraniuk, W. W. Symes, and D. M. Mittleman, "Terahertz reflection imaging using Kirchoff migration", *Opt. Lett.* **26**, 1513-1515 (2001).
47. T. Sato, M. Ueda, and S. Fukuda, "Synthetic Aperture Sonar", *J. Acoust. Soc. Am.* **54**, 799-802 (1973).

48. C. B. Burckhardt, P. A. Grandchamp, and H. Hoffmann, "An Experimental 2 MHz Synthetic Aperture Sonar System Intended for Medical Use", *IEEE Trans. Sonics and Ultrasonics* SU-21, 1-6 (1974).
49. M. Soumekh, *Fourier Array Imaging*, (Prentice-Hall, Englewood Cliffs, NJ 1994).
50. D. R. Wehner, *High Resolution Radar*, (Artech House, Norwood, MA 1987).
51. Y. Li and E. Wolf, "Three-dimensional intensity distribution near the focus in systems of different Fresnel numbers", *J. Opt. Soc. Am. A* **1**, 801-808 (1984).
52. Trademark Information, MATLAB is a registered trademark of Mathworks, Inc.

Vita



Education

B.S.E. in Electrical Engineering, University of Michigan, Ann Arbor, MI, May 1998. Cumulative GPA: 3.91/4.00.

Completed the Requirements for the Doctor of Philosophy degree at Oklahoma State University in December, 2003.

Professional Experience

Research Assistant, School of Electrical and Computer Engineering, Oklahoma State University, (August 1999-December 2003), Stillwater, OK, USA.

System Engineer, Motorola SSG, Inc. (July 1998-August 1999) Scottsdale, AZ, USA.

Technical Assistant, IMRA America, Inc. (August 1997-December 1997) Ann Arbor, MI, USA.

Honors and Memberships

Member Eta Kappa Nu, Electrical Engineering Honor Fraternity
Member Tau Beta Pi, Engineering Honor Fraternity
James B. Angell Scholar, University of Michigan
Dean's Honor List, University of Michigan